

**Study on Static and Dynamic Structure of
Crosslinked Rubber with Reinforcing Agent
by Quantum Beam**

Ryo Mashita

2016

Preface

The present thesis is submitted for Doctor of Philosophy degree at Kyoto University. The research described herein was conducted under the supervision of Professor Toshiji Kanaya, Laboratory of Polymer Materials Science, Division of Multidisciplinary Chemistry Polymer Materials Science, Institute for Chemical Research, Kyoto University, from 2013 to 2015.

The author thanks for lots of advice and experimental support as described in Acknowledgements section.

The author would be greatly pleased if this thesis contributes to the development of this study field.

March 2016

Ryo Mashita

Contents

1	General Introduction	1
1.1	Introduction	1
1.2	Brief Summary of Static Structure Studies of Rubber Materials with Fillers	4
1.3	Brief Summary of Dynamic Structure Studies of Rubber Materials with Fillers	6
1.4	Work Strategy	11
1.5	Thesis Outline	13
	References	14
2	Theoretical Background	19
2.1	Small-angle Scattering	19
2.2	Quasielastic Neutron Scattering	29
2.3	Muon Spin Relaxation	35
2.4	X-ray Computed Tomography	40
	References	44
3	Small-angle X-ray and Neutron Scattering Analyses of Highly Crosslinked Rubber with Unsaturated Carboxylic Acid	45
3.1	Introduction	45
3.2	Experimental	47
3.3	Results and Discussion	49
3.4	Conclusion	62
	References	63
4	Structure Analyses of Polybutadiene Rubber Crosslinked with Unsaturated Carboxylate using Contrast Variation Small-angle Neutron Scattering	65
4.1	Introduction	65

4.2	Experimental	66
4.3	Results and Discussion	68
4.4	Conclusion	83
	References	83
5	Quasielastic Neutron Scattering Study of Microscopic Dynamics in Polybutadiene Reinforced with an Unsaturated Carboxylate	85
5.1	Introduction	85
5.2	Experimental	86
5.3	Results and Discussion	87
5.4	Conclusion	97
	References	98
6	Dynamical Study of Polybutadiene Reinforced with an Unsaturated Carboxylate by Muon Spin Relaxation	100
6.1	Introduction	100
6.2	Experimental	101
6.3	Results and Discussion	103
6.4	Conclusion	108
	References	109
7	Observation of Deformation Behavior of Tire Rubber Depending on Asperity of Road by Four Dimensional X-ray Computed Tomography	110
7.1	Introduction	110
7.2	Experimental	112
7.3	Results and Discussion	115
7.4	Conclusion	119
	References	119
	Summary	121

List of Publications	123
Acknowledgements	124

Chapter 1

General Introduction

1.1 Introduction

Rubber materials utilized in various industrial products, such as automobile tires, airplanes, and base isolation devices, are indispensable in industry and our daily life. In order to enhance various properties of pure rubber, including mechanical strength, abrasion resistance, and deterioration resistance, rubber materials are modified by adding some fillers or functional agents depending on which particular properties are to be improved. For example, mechanical properties of rubber materials can be enhanced by an addition of crosslinking agents or reinforcing fillers, such as carbon black (CB), silica, or clay. Numerous studies on reinforcement effects of crosslinking agents and reinforcing fillers have been reported.

An increase in elastic modulus G of rubber after addition of CB can be calculated using the Guth-Gold equation [1, 2]:

$$G = G_0(1 + 2.5\phi + 14.1\phi^2), \quad (1.1)$$

where G_0 and ϕ are elastic modulus of unfilled rubber and volume fraction of CB, respectively. Figure 1.1 shows the elastic moduli of different CB-modified rubbers as functions of a CB volume fraction, where the solid line represents theoretical results obtained by Eq. 1.1. Although Eq. (1.1) is capable of predicting experimental values of elastic modulus at low volume fractions of CB fillers, calculated results significantly underestimate rubber elastic moduli in the region of high CB volume fractions [3]. Such a discrepancy is most likely caused by a network of a rigid constrained rubber

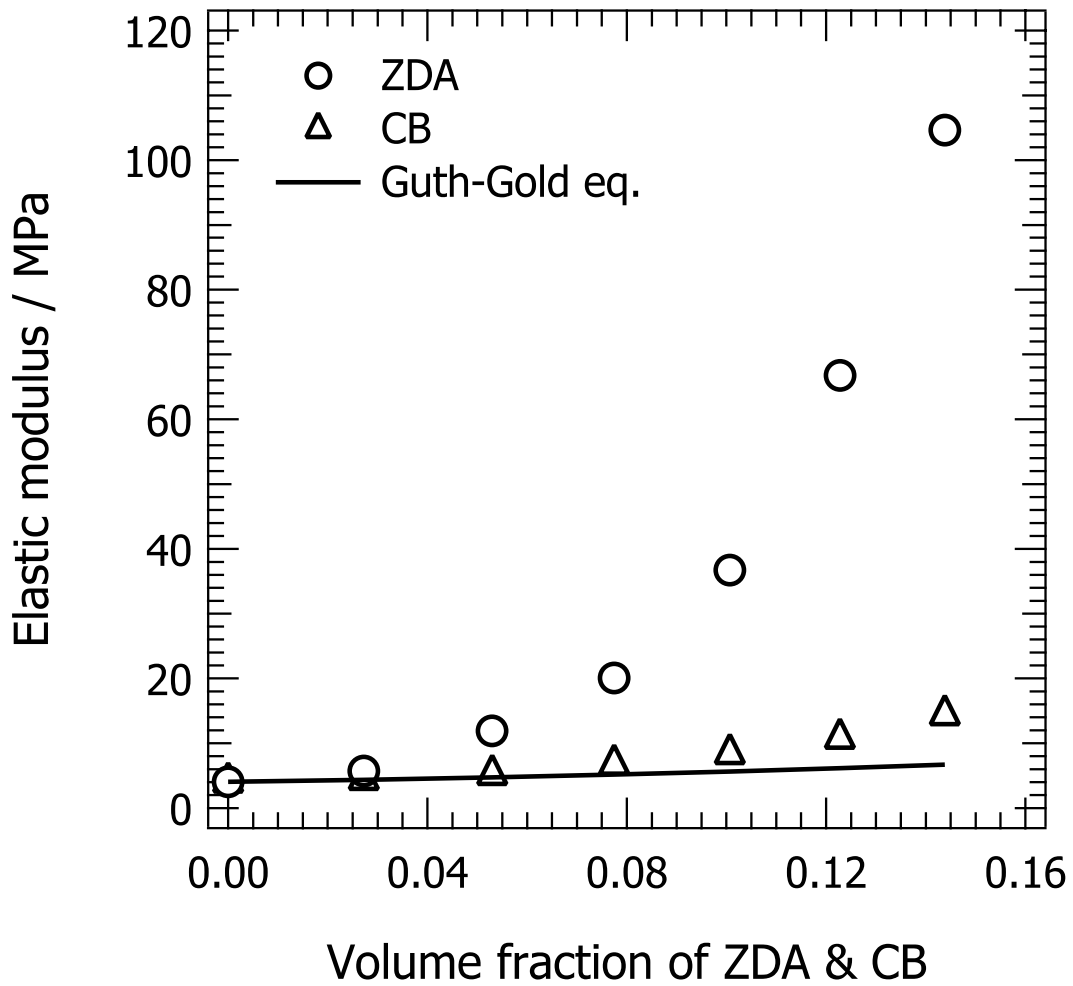


Figure 1.1 : Relationships between elastic moduli of rubber and volume fractions of ZDA and CB fillers. The solid line represents theoretical data calculated by using Eq. (1.1).

phase, which is formed around CB particles at high fractions of CB, drastically increasing elastic modulus [3, 4]. Although various models including a modified Guth-Gold equation [5, 6] were proposed to take into account the effect of confined rubber networks, commonly accepted models still do not exist because of the heterogeneity of rubber materials. For example, reinforcing fillers not only homogeneously disperse, but also hierarchically aggregate [7]. Therefore, hierarchical static and dynamic analyses are required to elucidate the mechanism of filler reinforcement effects.

Rubbers crosslinked with metal diacrylates exhibit excellent mechanical properties without addition of reinforcing fillers such as CB, silica or clay, and the structure of these rubber materials has been extensively studied [8-12]. In particular, the mechanical strength of rubbers reinforced with zinc diacrylate (ZDA) is much stronger than that of rubbers reinforced with regular CB or silica (as can be seen from Figure 1.1). The mechanism of ZDA rubber reinforcement is not yet fully clarified despite an increase in mechanical strength. Metal ion aggregates with sizes of 1 – 30 nm were previously assumed to be responsible for mechanical properties of these materials, which made many researchers focus on structural analyses of these aggregates in rubbers [13-16]; however, no dramatic improvements of mechanical properties were reported despite extensive efforts. On the other hand, structures of rubber matrices, which occupy most of the volume in rubber materials, have not been studied in detail due to their complexity. Thus, an elucidation of rubber matrix structures can lead to an enhancement of mechanical properties of rubber materials.

The main goal of this thesis is to elucidate the cause of very strong ZDA reinforcement effects of rubber materials from a molecular viewpoint. For this purpose, quantum beam techniques such as neutron scattering, synchrotron radiation X-ray scattering, and muon spin relaxation were

employed. In order to demonstrate research progress in the field of reinforced rubber materials in terms of their static and dynamic properties, some recently reported studies are discussed.

1.2 Static Structure Studies of Rubber Materials with Fillers

Figure 1.2 shows the electron microscopy images of rubber materials with various dispersed fillers indicating that the fillers do not disperse homogeneously in rubbers, but hierarchically aggregate. Metal ions aggregate in clusters with sizes of 1 – 30 nm and disperse heterogeneously in rubber matrices crosslinked with metal diacrylates [13-16]. Thus, electron microscopy studies are useful for investigating filler dispersion states because the differences in electron density between polymers and reinforcing agents are large. On the other hand, only local structure information can be obtained by electron microscopy due to its narrow field of view. To overcome this disadvantage, small-angle scattering measurements were performed to investigate dispersion states of reinforcing agents averaged over the whole system. Heterogeneous and hierarchical structures of rubber materials with fillers were studied by performing small-angle X-ray scattering (SAXS) measurements, and the obtained results were interpreted using a *unified approach model* [17-19], which assumes a fractal mechanism of filler aggregation (implying that the first aggregation step defines the second aggregation step, while the second aggregation step defines the third aggregation step and so on). The unified approach model reproduces experimental results obtained for various rubber/filler systems fairly well [17-19, 20].

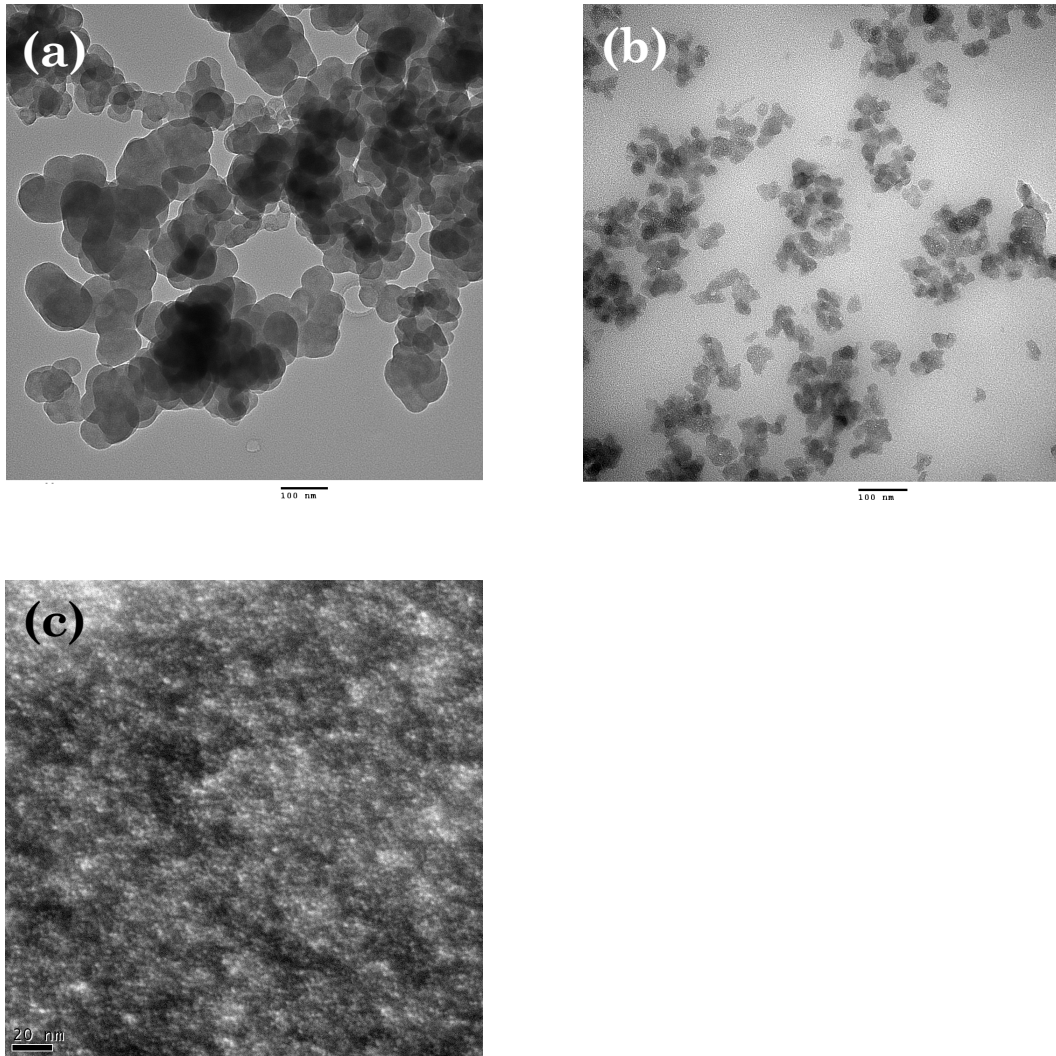


Figure 1.2 : Transmission electron microscopy images of the dispersion states of different fillers in rubber materials. (a) A CB/rubber system. (b) A silica/rubber system. (c) A zinc diacrylate/rubber system.

It is difficult to observe a constrained rubber phase around filler particles with an electron microscope because of the lack of contrast between the constrained rubber and the matrix rubber. Therefore, a static structure of constrained rubber around filler particles was investigated with a contrast variation small-angle neutron scattering (CV-SANS) method [21-26], in which individual self-correlation functions and cross-correlation functions of scattering components can be studied separately (the details of this method are provided in Chapter 2.2). Constrained rubber layers were reported to exist around fillers with thicknesses of several nm for rubber/silica or CB systems [25, 26]. Thus, using both electron microscopy and small-angle scattering techniques is important for an accurate analysis of the static structure of heterogeneous materials such as rubber/filler systems.

1.3 Dynamic Structure Studies of Rubber Materials with Fillers

Different processes occur in rubber materials at various time scales suggesting that controlling rubber dynamic properties at each possible time scale is important for improving its mechanical properties. Therefore, in addition to the static structure information obtained by electron microscopy small-angle scattering, data on the dynamic structure at different time scales are essential for successful material development. Figure 1.3 shows typical dynamical modes existing in polymers and the corresponding measuring methods for wide ranges of time and spatial scales [27]. Because particular modes of motion depend on spatial and time scales, an investigation of motion hierarchical structures conducted over a wide range of time scales is important. Thus, several dynamics studies of filler-reinforced rubbers were performed by various methods.

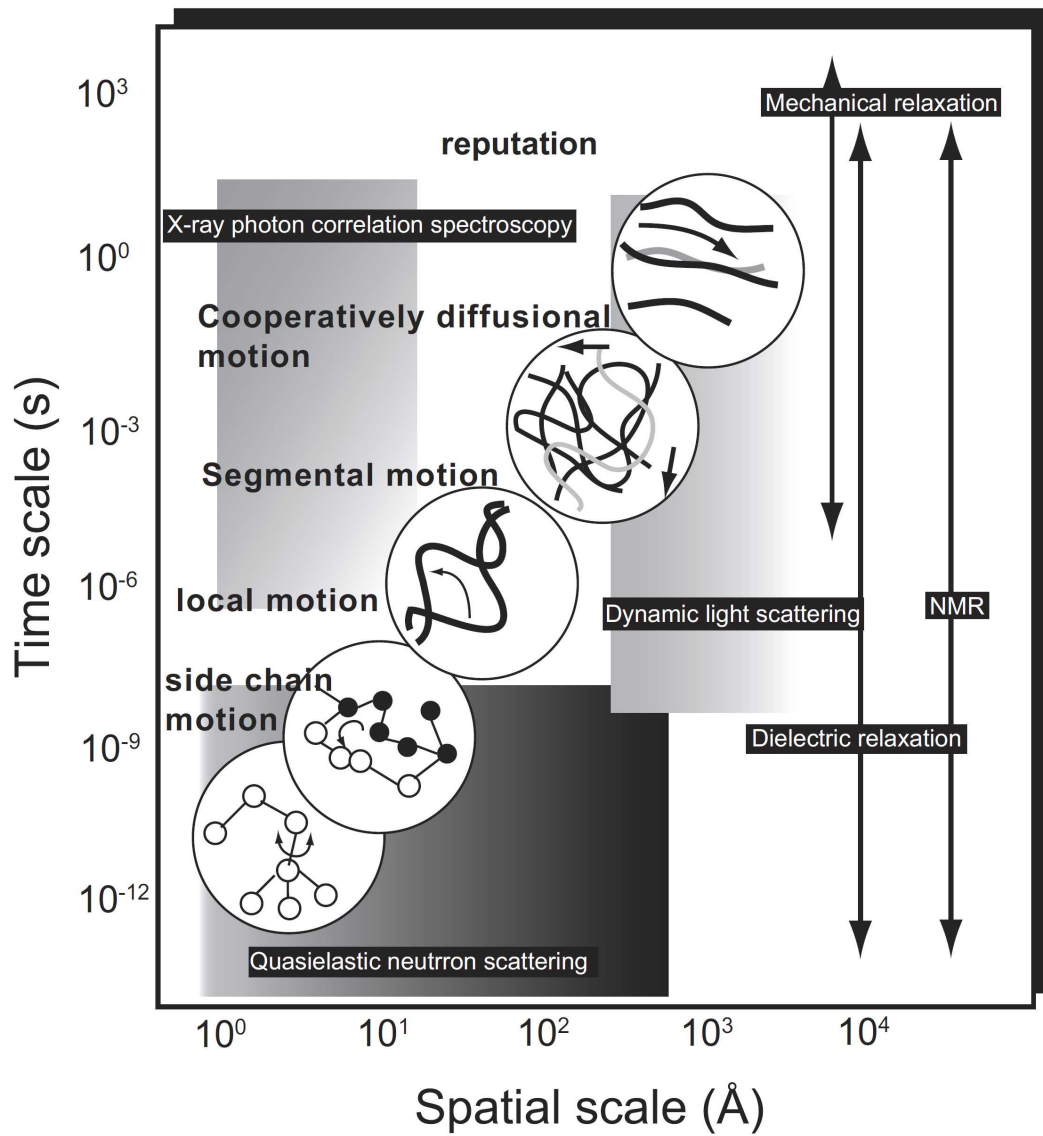


Figure 1.3 : Dynamics of amorphous polymers at different time and spatial scales studied by experimental methods [27].

An effect of fillers on rubber mechanical properties was studied from a rheological viewpoint by dynamic viscoelastic measurements. For CB/polybutadiene rubber (BR) systems, a local segmental mobility decreases, and a relaxation time distribution in the time range of $10^{-3} - 10^3$ s is broadened after an addition of CB [28, 29]. Dielectric relaxation spectroscopy is also a powerful tool for studying local segmental dynamics of polymers. For silica/natural rubber systems, a broadening of dielectric loss spectra was observed at low silica contents in the time range of $10^{-6} - 10^5$ s [30], but not at high silica contents. It is suggested that such a broadening originates from slowing polymer motion near the silica surface owing to silica particle aggregation at high silica contents, which results in lower values of silica surface area. Two relaxation components were also observed for a silica/poly(dimethylsiloxane) system in the time range of $10^{-8} - 10^2$ s [31]; one corresponded to an α relaxation associated with the glass transition in the polymer matrix, and the other one was due to an additional slower α relaxation attributed to motions of polymer chains near the silica/polymer interface (whose mobility was restricted due to interactions with the silica surface). In contrast to these results, relaxation times for filled and unfilled polymers in silica/poly(vinyl acetate) systems were equivalent in the time range of $10^{-5} - 10^2$ s [32]. The obtained data indicate that the degree of interaction between polymers and fillers depends on their particular combination.

Transverse proton (^1H) NMR relaxation measurements revealed a correlation between polymer dynamics and residual dipolar coupling [33-37]. In NMR relaxation measurements, a spin-spin relaxation time becomes shorter when a polymer mobility is constrained due to stronger spin-spin interactions at shorter distances between protons or when protons mobility decreases. In some silica/polymer systems, an additional mode with short relaxation times appears after silica addition suggesting an existence of

immobile rubber species attached to the silica surface in the time range of $10^{-5} - 10^{-2}$ s [36, 37]. Long, short, and intermediate components with time scales of 10^{-2} , 10^{-5} , and 10^{-4} s, respectively, were obtained from the NMR relaxation decay data. These three modes were assigned to a polymer matrix, a polymer bound to a silica surface, and a loosely bound polymer, respectively [37].

The results of dynamic viscoelastic measurements, dielectric relaxation spectroscopy, and NMR relaxation are important for understanding rubber materials dynamics; however, a spatial scale of motion was not probed in these measurements. To elucidate the mechanism of filler reinforcement effects in detail, studies involving both spatial and time scales are required.

Recently, dynamical studies of filler/polymer systems by X-ray photon correlation spectroscopy (XPCS) measurements have been reported [38-42]. XPCS has an advantage of obtaining information about both spatial and time motions. The time range and scattering vector q -range in XPCS are several ten seconds and $0.03 - 0.3 \text{ nm}^{-1}$, respectively. In XPCS measurements of filler/polymer systems, the dynamics of a filler is mainly investigated because its electron density is usually higher than that of a polymer. In mixed silica/polybutadiene-polyisoprene systems, silica motion relaxation times are proportional to q^{-1} indicating that silica particles are hyper-diffusive in an entangled polymer host [41]. Such a hyper-diffusive motion of silica particles results from their hopping between cages formed by entangled polymer chains. In addition, relaxation times of silica particles increase with their volume fraction over the whole q -range. In a CB/styrene-butadiene rubber system, relaxation times of CB also increase with the volume fraction of CB over the whole q -range [42]. Moreover, a velocity of CB increases with temperature at low volume CB fractions due to a decrease in viscosity for matrix rubber polymers. When a volume fraction of CB is high, a velocity hardly increases with temperature, most likely

owing to a formation of CB percolated networks. Because CB particles are connected to each other, their dynamics is highly limited and hardly depends on matrix viscosity. Thus, XPCS can probe motions with relatively large spatial and time scales. To elucidate the reinforcement mechanism of fillers in rubber materials, a deep understanding of rubber dynamics is required at various spatial and time scales. In particular, investigating polymer dynamics is important because polymers are a major part of most rubber materials.

Using neutron scattering techniques such as neutron spin echo (NSE) and quasielastic neutron scattering (QENS), self-motions and distinct motions in polymers can be directly probed on a molecular level (by incoherent and coherent scattering, respectively). Therefore, many studies on polymer dynamics investigating filler effects on polymer dynamics by NSE [43-50] and QENS [28, 29, 51-57] were reported. It should be noted that time and spatial scales for NSE are larger than those for QENS. Confinement effects on polymer motion due to silica were observed for a silica/poly(ethylene-propylene) system, whereas no evidence for a mobility gradient in the neighborhood of silica particles was revealed at high silica contents as indicated by NSE measurements in the q -range of $0.5 - 1.15 \text{ nm}^{-1}$ and time range of $10^{-8} - 10^{-7} \text{ s}$ [50]. On the other hand, polymer segmental motions slowed and dynamic heterogeneity increased for a system of CB/BR studied by QENS in the q -range of $3.1 - 17.1 \text{ nm}^{-1}$ and time range of $10^{-10} - 10^{-8} \text{ s}$ [28], which is most likely due to bond formations on CB particle surfaces via reactive double bonds in BR. These experiments show that interactions between polymers and fillers are important for dynamics studies.

Friction between rubber materials and various objects is also related to rubber dynamics. In the case of tires, one of the typical rubber products, the friction between tire rubbers and road surfaces is a significant problem

for commercial applications. It is difficult to study the contact interface between rubbers and road surfaces directly because of road surface asperities and non-transparency of tire rubbers. X-ray computed tomography (CT) is one of the few methods for direct observations of the contact interface between rubbers and road surfaces [58-62]. For CB and silica/styrene-butadiene rubber systems, real-time X-ray CT observations of tire rubber breakages due to friction were reported [62]. The measured time and spatial ranges were several seconds and $10^{-4} - 10^{-3}$ m, respectively, close to the real usage environment of tire rubbers. According to the reported study, a rubber material was stretched by road projection resulting in a surface crack accompanied by a maximum value of frictional force, after which frictional force values drastically decreased. Such dynamical observations at realistic conditions are important for material developments.

1.4 Work Strategy

In this work, the origins of high elastic modulus for ZDA/BR systems are investigated from both static and dynamical viewpoints. As seen in Figure 1.1, the elastic modulus values for a ZDA/BR system is higher than those for a CB/BR system. An existence of constrained rubber networks physically or chemically attached to a CB surface in CB/rubber systems results in high mechanical strength as mentioned in Section 1.1 [3, 4]. In addition, rubber molecules adsorbed to a CB surface freely slide across the surface under tension indicating that chemical bonding between polymers and CB is negligible, while physical adsorption is dominant. Based on these results, it is expected that a higher elastic moduli for ZDA/BR are caused by stronger networks of BR (HC-BR) layers around ZDA species with high crosslink densities. From a chemical viewpoint, reactive carbon-carbon double bonds (C=C) in ZDA monomers react with BR suggesting that HC-BR layers are

mainly formed by chemical bonding. Therefore, HC-BR layers in ZDA/BR systems should be stronger than physically adsorbed layers in CB/BR systems indicating that networks of HC-BR layers are more rigid than those of polymers physically adsorbed on CB surfaces. Therefore, the high elastic modulus values of ZDA/BR observed in Figure 1.1 most likely result from such rigid networks of HC-BR.

Although many studies on rubber materials reinforced with metal acrylate were performed, no evidence suggesting an existence of high crosslink density polymers around metal acrylate species was detected indicating a difficulty of revealing the existence of a HC-BR layer by a single conventional method. In zinc di-methacrylate (ZDMA)/hydrogenated nitrile-butadiene rubber (HNBR) systems, high crosslink density HNBR species around ZDMA were not observed with an electron microscope despite the existence of ZDMA networks because of the lack of contrast between these two species [13]. Therefore, confirming the existence of HC-BR layers requires using quantum beams, such as X-ray, neutron or muon ones (as was done for CB/polymer systems) [26]. In order to elucidate the filler reinforcement mechanism in rubber materials, deep understanding of the rubber structure and dynamics is required for a wide range of space and time scales. In particular, a direct investigation of the static structure and polymer dynamics is important because polymer is a major part of most rubber materials. Because such quantum beams are available only at large research facilities, such as a synchrotron radiation research institute or research nuclear reactors, opportunities of using them for experimental purposes are limited. Although some filler/polymer systems were recently studied by quantum beams, this research field has not yet been developed very well. In this work, filler/polymer systems were investigated using quantum beams, which would contribute to further developments in this area.

1.5 Thesis Outline

The goal of this thesis is to investigate the reinforcement mechanism of ZDA/BR systems from static and dynamic viewpoints. Its outline is described as follows.

In Chapter 2, fundamental theories of small-angle scattering, QENS, muon spin relaxation, and X-ray CT are described to provide physical meanings to the observables introduced in the later chapters.

In Chapter 3, a static structure of a ZDA/BR system was investigated by using both SAXS and SANS techniques. ZDA was found to hierarchically aggregate in a size range from nanometers to micrometers. In addition, differences in scattering intensity profiles between SAXS and SANS indicate the existence of HC-BR layers. However, a quantitative analysis of the HC-BR layer structure by this method was complicated.

In Chapter 4, a static structure of a ZDA/BR was studied by CV-SANS method to reveal the detail of HC-BR. A correlation between ZDA and HC-BR layers was observed, indicating the existence of HC-BR layers around ZDA aggregates. In addition, some parameters of these layers, such as thickness and volume fraction of HC-BR were quantitatively described.

In Chapter 5, the dynamics of a ZDA/BR system was studied with QENS measurements at a picosecond time scale. Mean square displacements $\langle u^2 \rangle$ decrease with an increase in the ZDA volume fraction indicating that the BR dynamics is affected by ZDA. In addition, a gradient of BR mobility in the neighborhood of ZDA aggregates was quantitatively described, and the physical origin of high elastic modulus due to crosslinking with ZDA was elucidated by a detailed analysis of dynamic scattering laws.

In Chapter 6, hierarchical studies of the ZDA/BR system dynamics were performed by muon spin relaxation measurements at a microsecond time scale. The relaxation rates above the glass transition temperature at

higher ZDA volume fractions were smaller than those at lower ZDA volume fractions indicating that BR dynamics is affected by ZDA at this particular time scale.

In Chapter 7, a dynamic deformation behavior of tire rubber was studied by four-dimensional X-ray CT, simulating real-world conditions. Hysteresis characteristics of the tire rubber were confirmed during interactions between the rubber and a road.

In the end of the thesis, the obtained results and discussions are summarized.

References

- [1] H. M. Smallwood, *J. Appl. Phys.*, **15**, 758 (1944).
- [2] E. Guth, *J. Appl. Phys.*, **16**, 20 (1945).
- [3] Y. Fukahori, *Nippon Gomu Kyokaishi*, **83**, 175 (2010).
- [4] Y. Fukahori, *Rubber Chem. Technol.*, **80**, 701 (2007).
- [5] M. J. Wang, S. Wolff, E. H. Tan, *Rubber Chem. Technol.*, **66**, 178 (1993).
- [6] J. S. Bergstrom, M. C. Boyce, *Rubber Chem. Technol.*, **72**, 633 (1999).
- [7] H. Kishimoto, Y. Shinohara, Y. Amemiya, K. Inoue, Y. Suzuki, A. Takeuchi, K. Uesugi, N. Yagi, *Rubber Chem. Technol.*, **81**, 541 (2008).
- [8] B. J. Chu, D. Q. Wu, R. D. Lundberg, W.J. Macknight, *Macromolecules*, **26**, 994 (1993).
- [9] Y. Tsujita, M. Yasuda, M. Takei, T. Kinoshita, A. Takizawa, H. Yoshimizu, *Macromolecules*, **34**, 2220 (2001).
- [10] M. Al-Hussein, B. G. G. Lohmeijer, U. S. Schubert, W. H. de Jeu, *Macromolecules*, **36**, 9281 (2003).
- [11] C. N. Zhou, D. C. Chan, I. K. Winey, *Macromolecules*, **41**, 6134 (2008).
- [12] E. M. Seitz, D. C. Chan, L. K. Opper, W. T. Baughman, B. K. Wagener, I. K. Winey, *J. Am. Chem. Soc.*, **132**, 8165 (2010).

- [13] N. Nagata, T. Sato, T. Fujii, Y. Saito, *J. Appl. Polym. Sci.*, **53**, 103 (1994).
- [14] X. Yuan, Y. Zhang, Z. Peng, Y. Zhang, *J. Appl. Polym. Sci.*, **84**, 1403 (2002).
- [15] Z. Wei, Y. Lu, S. Yan, Y. Meng, L. Zhang, *J. Appl. Polym. Sci.*, **124**, 288 (2012).
- [16] Z. Wei, Y. Lu, Y. Meng, L. Zhang, *Polymer*, **53**, 1409 (2012).
- [17] G. Beaucage, *J. Appl. Cryst.*, **28**, 717 (1995).
- [18] G. Beaucage, *J. Appl. Cryst.*, **29**, 134 (1996).
- [19] G. Beaucage, H. K. Kammler, S. E. Pratsinis, *J. Appl. Cryst.*, **37**, 523 (2004).
- [20] T. Koga, T. Hashimoto, M. Takenaka, K. Aizawa, N. Amino, M. Nakamura, D. Yamaguchi, S. Koizumi, *Macromolecules*, **41**, 453 (2008).
- [21] S. Miyazaki, H. Endo, T. Karino, K. Haraguchi, M. Shibayama, *Macromolecules*, **40**, 4287 (2007).
- [22] Y. Ikeda, N. Higashitani, K. Hijikata, Y. Kukubo, Y. Morita, M. Shibayama, N. Osaka, T. Suzuki, H. Endo, S. Kohjiya, *Macromolecules*, **42**, 2741 (2009).
- [23] T. Suzuki, N. Osaka, H. Endo, M. Shibayama, Y. Ikeda, H. Asai, N. Higashitani, Y. Kokubo, S. Kohjiya, *Macromolecules*, **43**, 1556 (2010).
- [24] H. Endo, D. Schwahn, H. Cölfen, *J. Chem. Phys.*, **120**, 9410 (2004).
- [25] M. Takenaka, S. Nishitsuji, N. Amino, Y. Ishikawa, D. Yamaguchi, S. Koizumi, *Macromolecules*, **42**, 308 (2009).
- [26] M. Takenaka, S. Nishitsuji, N. Amino, Y. Ishikawa, D. Yamaguchi, S. Koizumi, *Rubber Chem. Technol.*, **85**, 157 (2012).
- [27] R. Inoue, *PhD Thesis, Kyoto University*, 3 (2008).
- [28] J. H. Roh, M. Tyagi, T. E. Hogan, C. M. Roland, *Macromolecules*, **46**, 6667 (2013).
- [29] J. H. Roh, M. Tyagi, T. E. Hogan, C. M. Roland, *J. Chem. Phys.*, **139**,

134905 (2013).

- [30] D. Fragiadakis, L. Bokobza, P. Pissis, *Polymer*, **52**, 3175 (2011).
- [31] D. Fragiadakis, P. Pissis, L. Bokobza, *Polymer*, **46**, 6001 (2005).
- [32] R. B. Bogoslovov, C. M. Roland, A. R. Ellis, A. M. Randall, C. G. Robertson, *Macromolecules*, **41**, 1289 (2008).
- [33] H. Luo, M. Klüppel, H. Schneider, *Macromolecules*, **37**, 8000 (2004).
- [34] C. A. Steren, G. A. Monti, *Macromolecules*, **37**, 5624 (2004).
- [35] S. Hayashi, Y. Komori, *Solid State Nucl. Mag.*, **36**, 167 (2009).
- [36] A. Papon, K. Saalwachter, K. Schaler, L. Guy, F. Lequeux, H. Montes, *Macromolecules*, **44**, 913 (2011).
- [37] J. W. ten Brinke, V. M. Litvinov, J. E. G. J. Wijnhoven, J. W. M. Noordermeer, *Macromolecules*, **35**, 10026 (2002).
- [38] H. Guo, G. Bourret, R. B. Lennox, M. Sutton, J. L. Harden, R. L. Leheny, *Phys. Rev. Lett.*, **109**, 055901 (2012).
- [39] T. Koga, N. Jiang, P. Gin, M. K. Endoh, S. Narayanan, L. B. Lurio, S. K. Sinha, *Phys. Rev. Lett.*, **107**, 225901 (2011).
- [40] Y. Shinohara, H. Kishimoto, T. Maejima, H. Nishikawa, N. Yagi, Y. Amemiya, *Soft Matter*, **8**, 3457 (2012).
- [41] D. Kim, S. Srivastava, S. Narayanan, L. A. Archer, *Soft Matter*, **8**, 10813 (2012).
- [42] Y. Shinohara, H. Kishimoto, T. Maejima, H. Nishikawa, M. Takata, Y. Amemiya, *Mater. Sci. Eng.*, **24**, 012005 (2011).
- [43] X. Frielinghaus, M. Brodeck, O. Holderer, H. Frielinghaus, *Langmuir*, **26**, 17444 (2010).
- [44] J. Martin, M. Krutyeva, M. Monkenbusch, A. Arbe, J. Allgaier, A. Radulescu, P. Falus, J. Maiz, C. Mijangos, J. Colmenero, D. Richter, *Phys. Rev. Lett.*, **104**, 197801 (2010).
- [45] K. Nusser, G. J. Schneidera, D. Richter, *Soft Matter*, **7**, 7988 (2011).
- [46] Y. Li, M. Kroger, W. K. Liu, *Phys. Rev. Lett.*, **109**, 118001 (2012).

- [47] T. Glomann, A. Hamm, J. Allgaier, E. G. Hubner, A. Radulescu, B. Faragoc, G. J. Schneider, *Soft Matter*, **9**, 10559 (2013).
- [48] T. Glomann, G. J. Schneider, J. Allgaier, A. Radulescu, W. Lohstroh, B. Farago, D. Richter, *Phys. Rev. Lett.*, **110**, 178001 (2013).
- [49] G. J. Schneider, K. Nusser, S. Neueder, M. Brodeck, L. Willner, B. Farago, O. Holderer, W. J. Brielsd, D. Richter, *Soft Matter*, **9**, 4336 (2013).
- [50] G. J. Schneider, K. Nusser, L. Willner, P. Falus, D. Richter, *Macromolecules*, **44**, 5857 (2011).
- [51] V. Arrighi, J. S. Higgins, A. N. Burgess, G. Floudas, *Polymer*, **39**, 6369 (1998).
- [52] S. Gagliardi, V. Arrighi, R. Ferguson, M. T. F. Telling, *Physica B*, **301**, 110 (2001).
- [53] C. Karlsson, A. S. Best, J. Swenson, W. S. Howells, L. Borjesson, *J. Chem. Phys.*, **118**, 4206 (2003).
- [54] K. Chrissopoulou, S. H. Anastasiadis, E. P. Giannelis, B. Frick, *J. Chem. Phys.*, **127**, 144910 (2007).
- [55] S. Fotiadou, K. Chrissopoulou, B. Frick, S. H. Anastasiadis, *J. Polym. Sci. Pol. Phys.*, **48**, 1658 (2010).
- [56] P. Akcora, S. K. Kumar, V. G. Sakai, Y. Li, B. C. Benicewicz, L. S. Schadler, *Macromolecules*, **43**, 8275 (2010).
- [57] K. Sinha, W. Wang, K. I. Winey, J. K. Maranas, *Macromolecules*, **45**, 4354 (2012).
- [58] N. Amino, Y. Uchiyama, T. Iwai, *Nippon Gomu Kyokaishi*, **74**, 110 (2001).
- [59] N. Amino, Y. Uchiyama, T. Iwai, *Nippon Gomu Kyokaishi*, **82**, 346 (2008).
- [60] N. Amino, Y. Ishikawa, M. Takeuchi, *Nippon Gomu Kyokaishi*, **84**, 117 (2011).
- [61] N. Amino, *Nippon Gomu Kyokaishi*, **85**, 332 (2012).

[62] N. Amino, Y. Ishikawa, M. Sato, *Nippon Gomu Kyokaishi*, **87**, 278 (2014).

Chapter 2

Theoretical Background and Experimental Techniques

In this thesis, we used small-angle X-ray and neutron scattering, quasi-elastic neutron scattering, muon spin relaxation and X-ray computed tomography methods for the investigation of static and dynamic structure of rubber materials. We describe the basic theories of these methods.

2.1 Small-angle Scattering

In this section we describe the basic theory of small-angle neutron scattering and the contrast variation technique [1-3]. We omit the explanation of small-angle X-ray scattering because its theory is almost the same as that of neutron scattering and, in addition, neutron scattering is mainly used in this thesis.

2.1.1 Small-angle Neutron Scattering

The small-angle neutron scattering (SANS) method relies on the wave character of neutrons, which in site \mathbf{r} may be expressed as

$$A(r) = A_0 \exp[-i(\mathbf{k} \cdot \mathbf{r})], \quad (2.1)$$

where A_0 represents the neutron beam amplitude and \mathbf{k} is the wave vector parallel to the direction of the beam and with size $k=2\pi/\lambda$, λ being the neutron wavelength given by the de Broglie relation.

The beam scattered from a site \mathbf{r}_i into a direction \mathbf{k}_θ given by the scattering angle 2θ is expressed as

$$A(\mathbf{k}_\theta)_{\mathbf{r}_i} = A \cdot b(\mathbf{r}_i) \exp[-i(\mathbf{k}_\theta \cdot \mathbf{r})], \quad (2.2)$$

where $b(\mathbf{r}_i)$ denotes the ability of the atom at site \mathbf{r}_i to scatter neutrons, the so-called scattering length. The scattering length of neutrons is dominated by the interaction with the nucleus.

It is convenient to rewrite the scattered wave vector \mathbf{k}_θ as $\mathbf{k}_\theta + \mathbf{Q}$, where \mathbf{Q} is the scattering vector, or momentum transfer, given as a function of scattering angle:

$$Q = |\mathbf{Q}| = \frac{4\pi}{\lambda} \sin \theta. \quad (2.3)$$

Eq. (2.2) is thereby rewritten as

$$A(\mathbf{Q})_{\mathbf{r}_i} = A \cdot b(\mathbf{r}_i) \exp[-i(\mathbf{Q} \cdot \mathbf{r})] \exp[-i(\mathbf{k}_0 \cdot \mathbf{r})]. \quad (2.4)$$

The total amplitude scattered from sample is the simple sum of these terms:

$$\begin{aligned} A(\mathbf{Q})_{\mathbf{r}_i} &= \sum_{\mathbf{r}_i \in \text{sample}} A_0 \cdot b(\mathbf{r}_i) \exp[-i(\mathbf{Q} \cdot \mathbf{r})] \exp[-i(\mathbf{k}_0 \cdot \mathbf{r})] \\ &= A_0 \exp[-i(\mathbf{k}_0 \cdot \mathbf{r})] \cdot \sum_{\mathbf{r}_i \in \text{sample}} b(\mathbf{r}_i) \exp[-i(\mathbf{Q} \cdot \mathbf{r})]. \end{aligned} \quad (2.5)$$

The measured intensity is the square of ensemble-averaged amplitude of the scattered beam, that is,

$$\begin{aligned} I_m(\mathbf{Q}) &= A_0^2 \left\langle \sum_{\mathbf{r}_i \in \text{sample}} b(\mathbf{r}_i) \exp[-i(\mathbf{Q} \cdot \mathbf{r})] \sum_{\mathbf{r}_j \in \text{sample}} b(\mathbf{r}_j) \exp[+i(\mathbf{Q} \cdot \mathbf{r})] \right\rangle \\ &= I_0 \sum_i \sum_j \left\langle b(\mathbf{r}_i) b(\mathbf{r}_j) \exp[-i(\mathbf{Q} \cdot \mathbf{r}_{ij})] \right\rangle, \end{aligned} \quad (2.6)$$

where $\mathbf{r}_{ij} = \mathbf{r}_j - \mathbf{r}_i$. Eq. (2.6) expresses how the wave character of the neutron beam gives rise to interference phenomena, when the beam is scattered from

different sites within a sample. In the following, we will consider the intensity normalized with the incoming beam: $I(\mathbf{Q}) = I_m(\mathbf{Q})/I_0$

SANS experiments do not give atomic length-scale resolution. In the scattering function expression for SANS, the scattering length b characterizing individual atoms (nuclei) is therefore conveniently replaced by a continuous *scattering length density* function

$$\rho(\mathbf{r}) = \sum_V b_i/V = \sum_V b_i N_A \delta / M_V, \quad (2.7)$$

averaged over an appropriate volume V . M_V is the molar mass within the volume V , δ is the mass density, and N_A is Avogadro's number.

Substituting the scattering length with scattering length densities, we can reformulate the scattering function, Eq. (2.6), into integral form expressed as

$$I(\mathbf{Q}) = \int \int_{i,j} \langle \rho(\mathbf{r}_i) \rho(\mathbf{r}_j) \exp[-i(\mathbf{Q} \cdot \mathbf{r}_{ij})] \rangle d\mathbf{r}_i d\mathbf{r}_j. \quad (2.8)$$

In the “isotropic medium,” the averaged correlation function $\langle \rho(\mathbf{r}_i) \rho(\mathbf{r}_j) \rangle$ cannot depend on specific sites, but only on the distance \mathbf{r}_{ij} . One of the integrals in Eq. (2.8) can thereby be eliminated, giving

$$\begin{aligned} I(\mathbf{Q}) &= V \int_{sample} \langle \rho(\mathbf{r}') \rho(\mathbf{r}' + \mathbf{r}) \exp[-i(\mathbf{Q} \cdot \mathbf{r})] \rangle d\mathbf{r} \\ &= V \int_{sample} \langle \gamma(\mathbf{r}) \exp[-i(\mathbf{Q} \cdot \mathbf{r})] \rangle d\mathbf{r}. \end{aligned} \quad (2.9)$$

We thereby see that the scattering function is the Fourier transform of the ensemble-averaged correlation function $\gamma(\mathbf{r}) = \rho(\mathbf{r}') \rho(\mathbf{r}' + \mathbf{r})$, correlating densities separated by a distance \mathbf{r} .

In idealized systems where all scattering objects are identical and that on average can be assumed to have spherical symmetry, it is possible to split the scattering function into a product of two terms: one term relating to the intraparticle correlations (the form factor) and the other term relating to the interparticle correlations (the structure factor). To see this, let us assume a sample consisting of n identical particles, each composed of M scattering sites with excess scattering length density $\Delta\rho$. To calculate the scattering function, we must thereby make a double integral running over indexes reflecting the n particles and M sites (subparticles):

$$I(\mathbf{Q}) = \iint_{(i,j) \in n} \iint_{(p,q) \in M} \left\langle (\Delta\rho)^2 \exp[-i\mathbf{Q} \cdot (\mathbf{r}_{pi} - \mathbf{r}_{qj})] \right\rangle d\mathbf{r}_{pi} d\mathbf{r}_{qi} d\mathbf{r}_{pj} d\mathbf{r}_{qj}, \quad (2.10)$$

where p and q represent sites within each of the n particles, and i and j represent different particles. Mathematically, Eq. (2.10) may be rewritten into the form

$$I(\mathbf{Q}) = (\Delta\rho)^2 \iint_{(i,j) \in n} \iint_{(p,q) \in M} \left\langle \exp[-i\mathbf{Q} \cdot (\mathbf{r}_{pi} - \mathbf{r}_{qi})] \exp[-i\mathbf{Q} \cdot (\mathbf{r}_{qi} - \mathbf{r}_{qj})] \right\rangle d\mathbf{r}_{pi} d\mathbf{r}_{qi} d\mathbf{r}_{pj} d\mathbf{r}_{qj}, \quad (2.11)$$

where we by adding and subtracting $\mathbf{Q}\mathbf{r}_{qi}$ in the exponent have split the term into two: one term representing intraparticle correlations ($i = j$) and the other term representing interparticle correlations ($p = q$). Using that all particles are exactly similar, and assuming that the interparticle correlations are only relative weak, it is possible to split the sum in Eq. (2.11) into

$$I(\mathbf{Q}) = n(\Delta\rho)^2 M^2 \cdot \frac{1}{M^2} \iint_{(p,q) \in M} \left\langle \exp[-i\mathbf{Q} \cdot (\mathbf{r}_i - \mathbf{r}_j)] \right\rangle d\mathbf{r}_i d\mathbf{r}_j \cdot \left[1 + \frac{1}{n} \iint_{(i \neq j) \in n} \left\langle \exp[-i\mathbf{Q} \cdot (\mathbf{r}_p - \mathbf{r}_q)] \right\rangle d\mathbf{r}_p d\mathbf{r}_q \right], \quad (2.12)$$

which we will rewrite into the usual form

$$I(\mathbf{Q}) = nM^2(\Delta\rho)^2 \cdot P(\mathbf{Q})S(\mathbf{Q}). \quad (2.13)$$

We see that the scattering function is split into three terms: The first term is the prefactor that is proportional to the number concentration of particles, n , and the squared number of intraparticle scattering sites, that is, molar mass, M . The second term in Eq. (2.13) is the *form factor*, $P(Q)$, representing the form and size of the scattering object. $P(Q)$ is normalized to 1 at forward scattering: $P(Q=0) = 1$. The third term is the structure factor reflecting mutual distribution of the particles. For very dilute systems with no particular interparticle interaction, $S(Q)$ approaches unity, as evident from Eq. (2.12).

Form Factor

The form factor expresses structural details of the molecules or aggregates to be studied. In the case of a dilute sample of identical, randomly oriented particles, the scattering function, Eq. (2.12), may be reduced a function of the absolute value of $|\mathbf{r}| = r$:

$$I(\mathbf{Q}) = n_v(\Delta\rho)^2 4\pi \int r^2 \gamma(r) \cdot \frac{\sin(Qr)}{Qr} dr, \quad (2.13)$$

where n_v is the number density of particles and where it is assumed that the structure factor term of Eq. (2.12) can be set to unity, $S(Q) = 1$. At Q -values small compared to the inverse of the characteristic length of the scattering molecules, the $\sin(Qr)/(Qr)$ term may be expanded into a series in (Qr) , thereby giving Guinier approximation

$$I(Q) \propto \exp(-R_g^2 Q^2/3), \quad (2.14)$$

where R_g is the radius of gyration of the scattering object.

Generally, only the simplest structural form can be represented by analytical expressions for the form factor. This includes linear polymer chains when obeying Gaussian chain statistics, given by the Debye formula

$$I(Q) = \frac{2}{Q^4 R_g^4} \left[\exp(-Q^2 R_g^2) - 1 + Q^2 R_g^2 \right]. \quad (2.15)$$

Another example where $P(Q)$ is expressed analytically is a system that may be represented by simple dense sphere of radius R ,

$$P(Q) = \left[\frac{3}{Q^3 R^3} \left[\sin(QR) - QR \cos(QR) \right] \right]^2. \quad (2.16)$$

Structure Factor

The scattering function of particles in solution becomes increasingly dominated by interparticle correlations as the concentration is increased. This is given by the structure factor. In very dense systems, this term becomes the dominating part and evolves into resolution-limited Bragg peaks if the system forms ordered structure. Here we will only discuss the one based on the Ornstein-Zernike (OZ) approximation and applying the Percus-Yevick closure with hard-sphere interaction potential. $S(Q)$ is in the hard-sphere Percus-Yevick approximation given analytically by two parameters only, the volume fraction ϕ and the hard-sphere interaction distance R_{hs} .

$$S(Q) = \frac{1}{1 + 24\phi G(QR_{hs}, \phi)/(2QR_{hs})}, \quad (2.17)$$

where G is a trigonometric function of Q , R_{hs} and ϕ .

We see that for relatively small volume fractions, the main effect of the structure factor is to decrease the intensity at the lowest angles, while at higher volume fractions, oscillations in the structure factor will become a dominating factor in the scattering data, eventually evolving into real Bragg reflections if the suspension forms an ordered system.

2.1.2 Contrast Variation Technique

The scattering intensities observed from multicomponent systems can be expressed with partial scattering functions, $S_{ij}(Q)$, as following:

$$I(Q) = \sum_{i=1}^p \rho_i^2 S_{ii}(Q) + 2 \sum_{i < j}^p \rho_i \rho_j S_{ij}(Q) \quad , \quad (2.18)$$

where the system consists of p components and ρ_i is a scattering length density of component i . On the assumption of incompressibility, we can reduce Eq. (2.18) to

$$I(Q) = \sum_{i=1}^{p-1} (\rho_i - \rho_p)^2 S_{ii}(Q) + 2 \sum_{i < j}^{p-1} (\rho_i - \rho_p)(\rho_j - \rho_p) S_{ij}(Q) \quad . \quad (2.19)$$

In Eq. (2.19) component p is chosen as background (the solvent is typically chosen). When SANS experiments are performed with contrast variation and the scattering intensities are obtained with m different contrasts, the observed scattering curves for each Q value yield a set of linear equations expressed as

$$\mathbf{I} = \mathbf{M} \cdot \mathbf{s} \quad , \quad (2.20)$$

where \mathbf{I} represents a vector of intensities, i.e.,

$$\mathbf{I} = \begin{pmatrix} I_1(Q) \\ \mathbf{M} \\ I_m(Q) \end{pmatrix} \quad , \quad (2.21)$$

where \mathbf{M} is an $m \times p! / [(p-2)!2!]$ matrix consisting of scattering contrasts, and \mathbf{s} is a vector consisting of the corresponding $p! / [(p-2)!2!]$ partial scattering functions on the basis of Eq. (2.19).

In Eq. (2.20), by calculating the orthogonal matrix \mathbf{M}^T , where $\mathbf{M}^T \cdot \mathbf{M} = \mathbf{E}$, the intensities can be decomposed into the partial scattering functions, i.e., $\mathbf{s} = \mathbf{M}^T \cdot \mathbf{I}$. This procedure has various advantages over the contrast matching; e.g., (i) the perfect matching condition is not required, which is strictly necessary when the target component has a minor fraction, (ii) not only self-terms ($S_{ii}(Q)$ in Eq. (2.18)) but also cross-terms ($S_{ij}(Q)$ in Eq. (2.18)) are simultaneously obtained.

Theory of partial scattering functions

First of all, the scattering amplitude of component i at the given Q value, $A_i(Q)$, is introduced as

$$A_i(Q) = \langle \exp(iQ \cdot r_i) \rangle, \quad (2.22)$$

where the scattering length is unity and the absolute vector r_i points towards the positions within component i . The self-terms, $S_{ii}(Q)$, is defined as

$$S_{ii}(Q) = A_i(Q) \cdot A_i^*(Q), \quad (2.23)$$

while the cross-terms, $S_{ij}(Q)$, is given by

$$S_{ij}(Q) = \frac{1}{2} [A_i(Q) \cdot A_j^*(Q) + A_i^*(Q) \cdot A_j(Q)] \quad , \quad (2.24)$$

where $A_i^*(Q)$ is a complex conjugate number of $A_i(Q)$. Eqs.(2.23) and (2.24) result in real numbers. Note that the self-terms are always positive, on the other hand, the cross-terms may be either positive or negative. According to the Babinet's principle, $A_i(Q)$ holds

$$\sum_{i=1}^p A_i(Q) = 0 \quad , \quad (2.25)$$

for a multicomponent system with p components.

As a next step, we consider a ternary system in order to overview how to realize the partial scattering functions concretely. The model ternary system consists of solvent (σ), particle A (α) and particle B (β), as depicted in Figure 2.1.

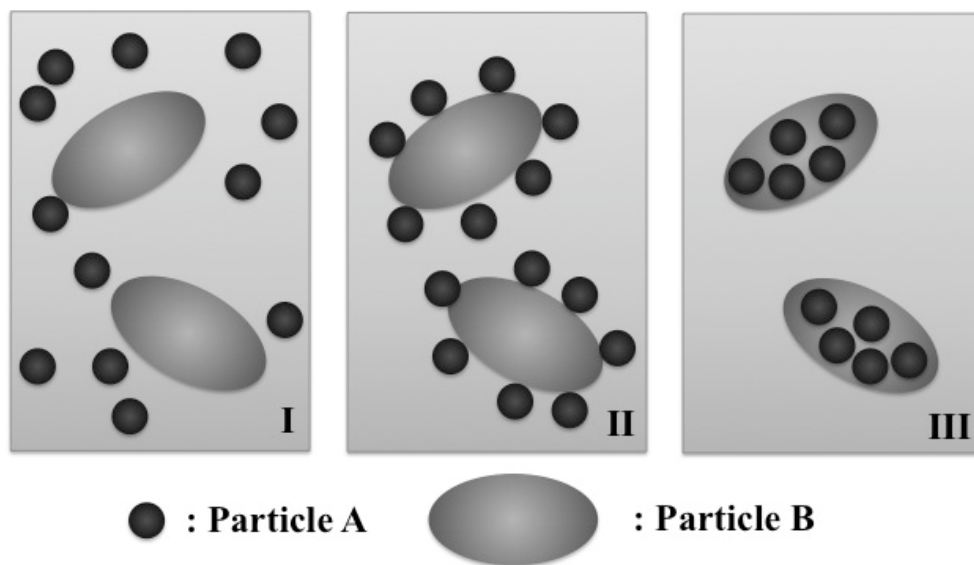


Figure 2.1: Model ternary systems consisting of particle A , particle B and solvent. Three types of “correlation” between A and B are drawn based on [2].

In the case of this ternary system, Eq. (2.25) leads to

$$A_\sigma(Q) = -A_\alpha(Q) - A_\beta(Q). \quad (2.26)$$

Therefore, by calculating the absolute values of Eq. (2.26),

$$S_{\sigma\sigma}(Q) = S_{\alpha\alpha}(Q) + 2S_{\alpha\beta}(Q) + S_{\beta\beta}(Q) \quad (2.27)$$

is obtained. Eq. (2.27) means that the cross-term $S_{\alpha\beta}$ can be related with the other three self-terms. The same treatments can be done for $S_{\beta\sigma}$ and $S_{\sigma\alpha}$, and we find

$$\begin{aligned} 2S_{\alpha\beta}(Q) &= -S_{\alpha\alpha}(Q) - S_{\beta\beta}(Q) + S_{\sigma\sigma}(Q), \\ 2S_{\beta\sigma}(Q) &= S_{\alpha\alpha}(Q) - S_{\beta\beta}(Q) - S_{\sigma\sigma}(Q), \\ 2S_{\sigma\alpha}(Q) &= -S_{\alpha\alpha}(Q) + S_{\beta\beta}(Q) - S_{\sigma\sigma}(Q). \end{aligned} \quad (2.28)$$

Since the cross-terms, $S_{ij}(Q)$, directly reflect the correlation between particle A , B and the solvent, it is quite useful to consider how $S_{ij}(Q)$ behaves in different cases shown in Figure 2.1. We postulate three types of the correlation, i.e., (i) particles A and B are not correlated (I in Figure 2.1), (ii) particles A and B are correlated and particles B are surrounded by A (II in Figure 2.1) and (iii) particles A and B are correlated and particles A are included within B (III in Figure 2.1). If there is no correlation between particles A and B , $S_{\alpha\beta}(Q)$ decays quickly to *null*, while in the case of existence of the correlation, $S_{\alpha\beta}(Q)$ shows *nonzero* values. Furthermore, we can distinguish between the case of II and III in Figure 2.1 by attending to high- Q values of $S_{\alpha\beta}(Q)$, where Porod's law is applicable. At high- Q the intensity of a self-terms $S_{ii}(Q)$ is proportional to its surface area, Σ_i . In the

case of II in Figure 2.1, $\Sigma_\alpha + \Sigma_\beta = \Sigma_\sigma$ holds, so that

$$S_{\alpha\beta}(Q) > (\approx)0, \quad S_{\beta\sigma}(Q) < 0, \quad S_{\sigma\alpha}(Q) < 0 \quad (2.29)$$

should be satisfied; on the other hand, as $\Sigma_\beta - \Sigma_\alpha = \Sigma_\sigma$ is fulfilled in case of III in Figure 2.1,

$$S_{\alpha\beta}(Q) < 0, \quad S_{\beta\sigma}(Q) < 0, \quad S_{\sigma\alpha}(Q) > (\approx)0 \quad (2.30)$$

may be achieved in Porod's region according to Eq. (2.28). The above relations of the cross-terms given by Eqs. (2.29) and (2.30) allow us to conclude the structure of the hybrid particle consisting of particles *A* and *B* as shown in Figure 2.1.

2.2 Quasi-elastic Neutron Scattering

In this section we describe the basic theory of quasi-elastic neutron scattering [1, 3-7].

Basic Scattering Theory

Information on the dynamic structure of condensed matter is obtained by analyzing the intensity of neutrons, e.g., from a monochromatic unpolarized neutron beam scattered by a sample into a solid angle element $d\Omega$ and an energy interval $d(\hbar\omega)$. This is proportional to the double-differential scattering cross section $d^2\sigma/d\Omega d\omega$:

$$\frac{d^2\sigma}{d\Omega d\omega} = \frac{k}{k_0} S(\mathbf{Q}, \omega) \quad , \quad (2.31)$$

where k_0 and k are the neutron wave vectors before and after scattering, respectively. That is, the product of the ratio of the neutron wave numbers

and van Hove's neutron dynamic scattering law $S(\mathbf{Q}, \omega)$. The latter is related with van Hove's correlation function $G(\mathbf{r}, t)$ and with the intermediate scattering function $I(\mathbf{Q}, t)$ by following two Fourier transforms:

$$S(\mathbf{Q}, \omega) = \frac{1}{2\pi} \int_{-\infty}^{\infty} e^{-i\omega t} I(\mathbf{Q}, t) dt \quad (2.32)$$

$$I(\mathbf{Q}, t) = \frac{1}{2\pi} \int_{-\infty}^{\infty} e^{-i\mathbf{Q}\cdot\mathbf{r}} G(\mathbf{r}, t) d\mathbf{r} \quad (2.33)$$

The most general (quantum mechanical) form (for unpolarized neutron) of the dynamic scattering law $S(\mathbf{Q}, \omega)$ per atom for a scattering system consisting of an ensemble of N atoms with nuclei generally having different scattering lengths b_i reads explicitly:

$$S(\mathbf{Q}, \omega) = \frac{1}{N} \sum_{i,j} \sum_{\psi_0} \langle \psi_0 | b_j \exp(-i\mathbf{Q}\cdot\mathbf{r}_j) | \psi_1 \rangle \langle \psi_1 | b_i \exp(-i\mathbf{Q}\cdot\mathbf{r}_i) | \psi_0 \rangle * \delta[(\omega_{\psi_1} - \omega_{\psi_0}) - \omega] \quad (2.34)$$

In this expression, we average over all pairs (i, j) of atoms with the bound scattering lengths (b_i, b_j) and the positions $(\mathbf{r}_i, \mathbf{r}_j)$, and sum over all the sample states ($\langle \psi_0 |$ before and $| \psi_1 \rangle$ after the scattering process) characterized by the wave functions ψ ; $p(\psi_0)$ is the statistical weight of the initial state ψ_0 , that is, the corresponding Boltzmann distribution. The δ -function expresses the conservation of the total energy eigenvalues ω_{ψ} are calculated from the Schrödinger equation.

As a consequence, the expression for the dynamic scattering law $S(\mathbf{Q}, \omega)$ now contains the averages of scattering length products

$$\langle b_j b_i \rangle = \langle b \rangle^2 + \delta_{ij} (\langle b^2 \rangle - \langle b \rangle^2) = b_{coh}^2 + \delta_{ij} b_{inc}^2 = \frac{\sigma_{coh}}{4\pi} + \frac{\delta_{ij} \sigma_{inc}}{4\pi} \quad (2.35)$$

permitting the definition of the coherent (σ_{coh}) and the incoherent (σ_{inc}) neutron scattering cross sections for a rigidly bound nucleus ($\delta_{ij} =$ Kronecker symbol), which will – in this type of a “monatomic approximation” – allow us

to separate the double differential scattering cross section into a coherent and an incoherent part:

$$\frac{d^2\sigma}{d\Omega d\omega} = \frac{k}{k_0} \left[\left(\frac{\sigma_{coh}}{4\pi} \right) S_{coh}(\mathbf{Q}, \omega) + \left(\frac{\sigma_{inc}}{4\pi} \right) S_{inc}(\mathbf{Q}, \omega) \right] \quad , \quad (2.36)$$

where $S_{coh}(\mathbf{Q}, \omega)$ and $S_{inc}(\mathbf{Q}, \omega)$ are the coherent and the incoherent dynamic scattering law, respectively. Eq. (2.36) consists of two terms each factorized in three independent components: (i) the ratio of the wave numbers k and k_0 characterizing the scattering process, (ii) the scattering cross sections for a rigidly bound nucleus, and (iii) the dynamic scattering laws. The latter depend on the scattering vector \mathbf{Q} ($=k - k_0$) and the energy transfer $\hbar\omega$. The coherent dynamic scattering law, $S_{coh}(\mathbf{Q}, \omega)$ in the first term, is due to the atom-atom pair correlations, whereas the incoherent dynamic scattering law, $S_{inc}(\mathbf{Q}, \omega)$ in the second term, merely conveys self-correlations of single atoms and, as consequence, only intensities (and not amplitudes) from scattering by different nuclei have to be added.

van Hove Correlation Function

Let us now consider the connection between coherent and incoherent dynamic scattering laws to be measured and correlation functions to be calculated in more detail. Starting again with the double-differential scattering cross section, but now in the ‘‘monatomic approximation’’, we have

$$\frac{d^2\sigma}{d\Omega d\omega} = \left(\frac{d^2\sigma}{d\Omega d\omega} \right)_{coh} + \left(\frac{d^2\sigma}{d\Omega d\omega} \right)_{inc} = \frac{k}{k_0} \frac{(\sigma_{coh} + \sigma_{inc})}{4\pi} S(\mathbf{Q}, \omega) \quad , \quad (2.37)$$

where

$$S(\mathbf{Q}, \omega) = \frac{\sigma_{coh}}{(\sigma_{coh} + \sigma_{inc})} S_{coh}(\mathbf{Q}, \omega) + \frac{\sigma_{inc}}{(\sigma_{coh} + \sigma_{inc})} S_{inc}(\mathbf{Q}, \omega) \quad . \quad (2.38)$$

Combining Eqs. (2.37) and (2.38) , one obtains Eq. (2.36).

Apart from the fact that the neutron-nuclear interaction has been extracted, the Fourier transformations establishing the pertinent relations between neutron dynamic scattering laws, intermediate scattering functions, and van Hove's correlation functions are analogous to Eqs. (2.32) and (2.33), as follows:

$$S_{coh}(\mathbf{Q}, \omega) = \frac{1}{2\pi} \int_{-\infty}^{\infty} e^{-i\omega t} I_{coh}(\mathbf{Q}, t) dt \quad (2.39)$$

$$I_{coh}(\mathbf{Q}, t) = \frac{1}{2\pi} \int_{-\infty}^{\infty} e^{-i\mathbf{Q}r} G_P(\mathbf{r}, t) d\mathbf{r} \quad (2.40)$$

$$S_{inc}(\mathbf{Q}, \omega) = \frac{1}{2\pi} \int_{-\infty}^{\infty} e^{-i\omega t} I_{inc}(\mathbf{Q}, t) dt \quad (2.41)$$

$$I_{inc}(\mathbf{Q}, t) = \frac{1}{2\pi} \int_{-\infty}^{\infty} e^{-i\mathbf{Q}r} G_S(\mathbf{r}, t) d\mathbf{r} \quad (2.42)$$

Furthermore, we have

$$G_P(\mathbf{r}, t) = \frac{1}{(2\pi)^3} \int_{-\infty}^{\infty} e^{-i\omega t} \int_{-\infty}^{\infty} e^{-i\mathbf{Q}r} S_{coh}(\mathbf{Q}, \omega) d\mathbf{Q} d\omega \quad (2.43)$$

$$G_S(\mathbf{r}, t) = \frac{1}{(2\pi)^3} \int_{-\infty}^{\infty} e^{-i\omega t} \int_{-\infty}^{\infty} e^{-i\mathbf{Q}r} S_{inc}(\mathbf{Q}, \omega) d\mathbf{Q} d\omega \quad (2.44)$$

Here, van Hove's pair correlation and self-correlation functions are labeled with the subscripts p and s, respectively. The classical meaning of the van Hove correlation functions can be described as follows: $G_P(\mathbf{r}_j - \mathbf{r}_i, t)$ is the conditional probability per unit volume to find an atom (nucleus) at a position \mathbf{r}_j at time t , if this or another atom has been at a position \mathbf{r}_i , with a distance vector $\mathbf{r} = \mathbf{r}_j - \mathbf{r}_i$, at a previous time $t = 0$. Analogously, the self-correlation function, $G_S(\mathbf{r}, t)$, is the conditional probability per unit volume to find an atom at $\mathbf{r}(t)$ at time t , if the same atom has been at the

origin $\mathbf{r} = 0$ at $t = 0$.

Elastic Incoherent Structure Factor

If an atom is diffusing in a space that is very large as compared to the interatomic distances, the self-correlation function $G_S(\mathbf{r}, t)$ vanishes, if t goes to infinity, whereas, for an atom *bound to a finite volume* (e.g., as part of a vibrating or rotating molecule fixed in a crystal), $G_S(\mathbf{r}, t)$ approaches a finite value $G_S(\mathbf{r}, \infty)$ for \mathbf{r} varying in the interior of this volume. In fact, generally, the self-correlation function can be split into its asymptotic value in the long-time limit and a time-dependent term $G'_S(\mathbf{r}, t)$, according to

$$G(\mathbf{r}, t) = G_S(\mathbf{r}, \infty) + G'_S(\mathbf{r}, t). \quad (2.45)$$

The Fourier transform of this expression over space and time according to Eqs. (2.41) and (2.42) yields

$$S_{inc}(\mathbf{Q}, \omega) = {}^{el}S_{inc}(\mathbf{Q})\delta(\omega) + {}^{ne}S_{inc}(\mathbf{Q}, \omega). \quad (2.46)$$

Apparently, the incoherent dynamic scattering law for a spatially restricted motion decomposed into a purely elastic line, ${}^{el}S_{inc}(\mathbf{Q})\delta(\omega)$, with the integrated intensity ${}^{el}S_{inc}(\mathbf{Q})$, and a non-elastic component, ${}^{ne}S_{inc}(\mathbf{Q}, \omega)$. The first term is the result of diffraction of the neutron on the “infinite time” *distribution in a space of a single nucleus spread over a finite volume by its motion*, as pointed out by Stiller [4]. Therefore, we can derive information about the structure in a very direct way from *incoherent* scattering [5]. In order to systematically exploit the theoretical fact expressed by Eq. (2.46) in neutron scattering experiments, the concept of the elastic incoherent structure factor (EISF) was formulated. The EISF concept provides a method, which permits the extraction of structural information on all kinds

of localized single-particle motion by the determination of the elastic function of the measured spectral intensity, as a function of \mathbf{Q} . The idea is simple: First, by employing a suitable (e.g., sufficiently high) energy resolution, the measured integrals of elastic ($^{el}Int(\mathbf{Q})$) and nonelastic ($^{ne}Int(\mathbf{Q})$) components of the dynamic scattering law in Eq. (2.46) are determined separately. Then, an intensity ratio involving the two integrals can be defined as

$$EISF = \frac{^{el}Int(\mathbf{Q})}{^{el}Int(\mathbf{Q}) + ^{ne}Int(\mathbf{Q})} = \frac{A^{el}S_{inc}(\mathbf{Q}, \omega)}{A \int_{-\infty}^{\infty} S_{inc}(\mathbf{Q}, \omega) d\omega} \quad (2.47)$$

where A is an experimental normalized factor. Because the factor A cancels and the integral of the incoherent dynamic scattering law is equal to unity by definition, we simply have $EISF = ^{el}S_{inc}(\mathbf{Q})$.

Experimental Energy Resolution and Observation Time

The variable neutron energy resolution $\Delta(\hbar\omega)$, and the implied variable observation time Δt_H , which is the decay time on the Fourier time scale of the Fourier transformed resolution function, are connected by the following exact uncertainly relation [6]

$$H_{RES} \cdot (\Delta t)_H = c\hbar, \quad (2.48)$$

where $H_{RES} = \Delta(\hbar\omega)$ has been defined as the half width at half maximum (HWHM) of the resolution function. The constant coefficient c is equal to 1, in the case of Lorentzian resolution function, whereas in the more realistic case of a Gaussian resolution function, $c = 2\sqrt{\ln 2}$.

The necessity to discuss resolution functions reflects the fact that the dynamic scattering laws S_{coh} and S_{inc} defined in Eqs. (2.39) – (2.42), as well as the corresponding functions G_P , G_S and the intermediate scattering

functions I_{coh} , I_{inc} cannot be determined experimentally in their pure forms. The reason is that, for example, the dynamic scattering laws are in principle broadened by the experimental resolution functions $R(\mathbf{Q}, \omega)$ in the four-dimensional (\mathbf{Q}, ω) -space. In the case of incoherent scattering, the \mathbf{Q} -spread of the resolution can often be neglected, when the studied functions are only rather slowly varying with \mathbf{Q} . It is sufficient to compare the measured resolution- broadened “dynamic scattering law”, $[S_{\text{inc}}(\mathbf{Q}, \omega)]_{\text{meas}}$ to a convolution of the measured energy-resolution function $R(\omega)$ with a theoretical dynamic scattering law $[S_{\text{inc}}(\mathbf{Q}, \omega)]_{\text{theo}}$ being developed, in order to simulate $S_{\text{inc}}(\mathbf{Q}, \omega)$:

$$[S_{\text{inc}}(\mathbf{Q}, \omega)]_{\text{meas}} = \int_{-\infty}^{\infty} [S_{\text{inc}}(\mathbf{Q}, \omega')]_{\text{theo}} R(\omega - \omega') d\omega' \quad (2.49)$$

The correlation functions are observed in a Fourier time window, with an upper limit controlled by the decay time constant Δt_{H} of the observation function. The low-time limit of this window has a different origin: For instruments working in (\mathbf{Q}, ω) -space, it is mainly a consequence of the statistical accuracy of the measurement, because quasi-elastic intensities typically decrease with increasing energy transfer, and therefore counting statistics become the poorer the larger the energy transfers are as compared to the energy-resolution width.

2.3 Muon Spin Relaxation

In this section we described the basic theory of muon spin relaxation techniques [8-11].

Muon Production

The collision of an accelerated proton (p) beam (typical energy 600 MeV) with the nuclei (n) of a production target produces positive pions (π^+) via the possible reactions

$$p + p \rightarrow p + n + \pi^+, \quad (2.50)$$

$$p + n \rightarrow n + n + \pi^+. \quad (2.51)$$

From the subsequent decay of the pions ($\tau_{\pi^+} = 26.03$ ns), positive muons (μ^+) are formed via the two-body decay

$$\pi^+ \rightarrow \mu^+ + \nu_{\mu}, \quad (2.52)$$

where both the neutrino (ν_{μ}) and the μ^+ have their spin antiparallel to their momentum in the π^+ rest frame. According to the value of the π^+ momentum at the decay time, two types of μ^+ beams are available for muon spin relaxation (μ SR) measurements.

The first type of muon beam is formed by the π^+ decaying in flight. Due to the relativistic transformation to the laboratory frame, and after momentum selection by bending magnets, typical muon beams are produced with a polarization of $\sim 80\%$ and energies of $\sim 40 - 50$ MeV. Although such a high-energy beam requires the use of suitable moderators and samples with sufficient thickness, it guarantees a homogeneous implantation of the muons in the sample volume.

The second type of muon beam is often called the “surface” or “Arizona” beam [10]. Here, muons are used that arise from π^+ decaying at rest near the surface of the production target. Such muons, which are 100% polarized and have a very low momentum, have a range width in matter of the order of 180 mg/cm². Hence the paramount advantage of this type of beam is the possibility to use thin samples. Moreover, novel low-background apparatus,

with special detector arrangements, were recently developed to drastically reduce the lateral dimensions of the sample. This has opened the fascinating possibility of investigating tiny single crystals ($\sim 1 \text{ mm}^3$). However, a possible drawback is that the implanted μ^+ are stopped on the surface layer of the sample, which could present different properties than the bulk. Therefore special care should be taken with the preparation of the specimens and reproducibility of the observed μSR results.

Principle of μSR

After the implantation in the solid sample, the muon is decelerated within 100 ps, which is too rapid to allow any significant loss of polarization and sufficiently rapid for the μSR time window. The μ^+ implanted in the sample decays after an average time of $\tau_\mu = 2.197 \text{ } \mu\text{s}$, according to

$$\mu^+ \rightarrow e^+ + \nu_e + \bar{\nu}_\mu, \quad (2.53)$$

where e^+ is a positron and ν_e and $\bar{\nu}_\mu$ are neutrinos. The parity violation in the weak interaction leads to an anisotropic distribution of the positron emission with respect to the spin direction of the μ^+ at the decay time.

Since muonium atoms (μ^+e^- ; Mu^\bullet) may be formed in situ by muons passing through the walls of sample cells, a range of liquid, solid and gas phase materials may readily be investigated. The muons then combine with radiolytic electrons; when both have achieved near thermal energies (Eq. (2.54)).



Muonium is equivalent to a normal protium atom (p^+e^-) and indeed shows the chemical properties of a light hydrogen atom (Mu^\bullet has a mass 1/9 that of a

protium atom); if the sample contains unsaturated organic molecules, Mu^\bullet can act as a normal hydrogen atom and undergo an addition reaction. The method is indeed highly specific for the study of free radicals, of which many types may be so formed, e.g. Eq. (2.55)–(2.58) [11]:



The μ SR Transverse-field (TF) Technique

The following is a description, specifically, of the TF- μ SR technique, in which each radical is characterized by a single pair of lines in its TF- μ SR spectrum (in high magnetic fields, applied transverse (at 90°) to the muon beam direction, which represent the $-1/2, +1/2 m_s$ electron spin combination with the muon (m_μ) states: these occur at the precession frequencies from muons which experience the sum of the applied and ($-1/2, +1/2 m_s$) hyperfine magnetic fields. The muon–electron hyperfine coupling constant is obtained from the difference between the high (ν_2) and low (ν_1) frequencies for each radical: $A_\mu = \nu_2 - \nu_1$; as the coupling increases, for a given magnetic field, the frequency ν_2 increases, while concomitantly ν_1 first decreases, reaches zero and then increases due to a sign change in the transition: in the latter limit the coupling is obtained from the sum of the frequencies: $A_\mu = \nu_1 - (-\nu_2)$.

An analysis of the data may be made corresponding to each frequency. muons decay to positrons ($\mu^+ \rightarrow e^+ + \nu_e + \bar{\nu}_\mu$) on a microsecond timescale, which are detected using scintillation counters, and counted using fast

electronics; the decay events are accumulated in four data histograms. Generally, the histogram is of the form

$$N(t) = N_0 \{B + \exp(-t/t_\mu)[1 + F(t)]\}, \quad (2.59)$$

where N_0 is a normalization factor, roughly equal to the number of counts in the first channel ($t = 0$), B is the background fraction (usually $< 1\%$), t_μ is the muon lifetime and $F(t)$ reflects the time dependence of the muon spin polarization. For experiments in which a number of frequencies are obtained, $F(t)$ is the sum of contributions of the form corresponding to a muon precession at a specific frequency ν_j , for which A_j is the asymmetry (amplitude), λ_j the relaxation rate which provides a measure of chemical reactions or physical relaxation processes, and ϕ_j is the initial phase. The data are analyzed by fitting directly the latter expression to the experimental data in Fourier space, which yields the parameters A_j , λ_j , ω_j , ϕ_j for each frequency.

$$F_j(t) = A_j \exp(-\lambda_j t) \cos(\omega_j t + \phi_j), \quad (2.60)$$

The μ SR Longitudinal-field (LF) Technique

LF- μ SR involves the application of an external magnetic field parallel to the initial direction of the muon spin polarization. When the frequency of a particular molecular motion (either intramolecular, or that of overall molecular reorientational diffusion) approaches that of the dominant spectral transition (ω) in the muon– electron coupled system, there is an increase in the relaxation rate (λ) of the muon spins, as measured in a longitudinal magnetic field (LF), which reaches a maximum when the frequencies are equal. Motional correlation times (τ) are extracted from the LF-relaxation rates (λ)

$$\lambda = (2\pi\delta A)^2 \tau / (1 + \omega^2 \tau^2). \quad (2.61)$$

Here, δA is the variation in the hyperfine frequency during the motional event, and represents the anisotropy in the hyperfine interaction, which is modulated by the molecular reorientational motion and relaxes the muon spin; ω is taken as the frequency of the $\langle 1 | \leftrightarrow | 2 \rangle$ transition, which is strongly induced by this mechanism. Since $\lambda = 1/T_1$, the maximum in the relaxation rate corresponds to a ' T_1 minimum' familiar in NMR spectroscopy, where a dominant transition frequency (ω) is matched by that of some motional process and the relaxation mechanism finds its maximal efficiency. Activation parameters E_a and τ_∞ are obtained from plots of $-\ln \tau$ vs $1/T$, according to the Arrhenius expression (2.62) in which τ_∞ is the 'attempt time', or 'reciprocal attempt frequency':

$$\tau = \tau_\infty \exp(E_a/RT). \quad (2.62)$$

2.4 X-ray Computed Tomography

In this section we described the basic theory of absorption contrast imaging, which contains X-ray computed tomography technique [12-14].

Radiography and Tomography

The first revolution in medical imaging with X-rays began in Roentgen's laboratory in 1895. The second had to wait until the 1970's when Godfrey Hounsfield invented the technique of Computer Axial Tomography, now commonly referred to as CAT or CT scanning. CT scanning overcomes the obvious main limitation of conventional radiography which measures spatial information. It does this by recording radiographic projections of the object

over a wide range of projection angles, from which it is then possible to reconstruct the full three-dimensional structure. To understand how this works we consider the absorption of a perfectly narrow X-ray beam in the plane of a two-dimensional object. The beam along the y' axis views the object at an angle θ with respect to the fixed $x - y$ coordinate system. For generality we assume that the absorption coefficient $\mu(x, y)$ of the object is non-uniform. The intensity recorded in a detector located behind the sample is

$$I = I_0 e^{-\int \mu(x,y) dy'} \quad (2.63)$$

which can be rearranged to read

$$\log\left(\frac{I_0}{I}\right) = \int \mu(x,y) dy' \quad (2.64)$$

It is thus possible to deduce the line integral of the absorption coefficient, which defines the function $R(\theta, x'=0)$, from the ratio of the intensity of the primary beam to that measured in the detector. Imagine now that the beam is scanned parallel to x' for fixed θ . This process will produce an intensity distribution $R(\theta, x')$ which depends on x' and the viewing angle θ . The function $R(\theta, x')$ is known as the Radon transform. The CT scan may therefore be thought of as a series of Radon transforms collected at a set of viewing angles.

The reconstruction of the two-dimensional image of the object from the Radon transform can be accomplished either algebraically, which is computationally inefficient, or using Fourier analysis techniques. The latter is the most widely adopted approach. It utilizes the Fourier slice theorem, which is derived in the next section.

Fourier Slice Theorem

Consider a general two-dimensional function $f(x, y)$ which is projected, or more precisely integrated, along the y axis to generate a new function of x only, defined by

$$p(x) = \int f(x, y) dy \quad (2.65)$$

The Fourier transform of $p(x)$ is

$$P(q_x) = \int p(x) e^{iq_x x} dx \quad (2.66)$$

It is then natural to ask what relationship does the Fourier transform of the projected function have to the Fourier transform of the original function $f(x, y)$. Again, by definition, the Fourier transform of $f(x, y)$ is

$$F(q_x, q_y) = \iint f(x, y) e^{i(q_x x + q_y y)} dx dy \quad (2.67)$$

Now we examine what happens when we set $q_y=0$. This defines a slice through $F(q_x, q_y)$ given by

$$F(q_x, q_y = 0) = \int \left[\int f(x, y) dy \right] e^{iq_x x} dx \quad (2.68)$$

The integral in the square brackets can then be readily indentified as $p(x)$, allowing us to write

$$F(q_x, q_y = 0) = \int p(x) e^{iq_x x} dx = P(q_x) \quad (2.69)$$

In other words the Fourier transform of the projection along a particular line of a two-dimensional function $f(x, y)$ is equal to a slice through the Fourier

transform of $f(x, y)$ taken along a line passing through the origin in the propagation direction. This is known as the Fourier slice theorem.

Implementing the Radon Transform and its Inverse

The process of CT scanning can be thought of as comprising three key steps. The first is the acquisition of the data as a series of radiographs. In mathematical terms, the data are described as a set of Radon transforms $R(\theta, x')$ taken at different viewing angles. Second, the data $R(\theta, x')$ are Fourier transformed. From the Fourier slice theorem the Fourier transform of the object can be constructed. Finally, an inverse Fourier transform is performed to obtain the reconstructed image of the object. From the Radon transform, the two-dimensional Fourier transform of the object is constructed, and the reconstructed image is then obtained via an inverse Fourier transform. For the analysis of real-life data, sophisticated smoothing and filtering algorithms are required to improve the fidelity of the reconstructed image.

Medical CT Scanning

The CT scanner commonly found in hospital. The patient sits at the centre of a rotation axis around which the X-ray source and detector rotate. The simplest implementation of CT to consider is where for a fixed rotation the X-ray source produces a series of parallel X-ray beams. These impinge on the patient at a particular height, and the Radon transform is recorded on a position sensitive detector. The source-detector carousel then rotates to its next setting and the process repeated until the whole sinogram, which is the plot of the Radon transform for the full range of viewing angles, is collected. The patient's height relative to the X-ray beam is then adjusted, and a new sheet image is obtained, with the process iterated until a full three-dimensional image is obtained as a stack of two-dimensional images.

References

- [1] T. Imae, T. Kanaya, M. Furusaka, N. Torikai, *Neutrons in Soft Matter*, John Wiley & Sons, Inc. (2011).
- [2] H. Endo, *Physica B* **385**, 682 (2006).
- [3] R. Ryong-Joon, *Methods of X-ray and Neutron Scattering in Polymer Science*, Oxford University press (2000).
- [4] H. Stiller, *Inelastic scattering of neutron* **2**, IAEA, Viena, 179 (1965).
- [5] K. Sköld, *J. Chem. Phys* **49**, 2443 (1968).
- [6] R. E. Lechner, *Physica B* **83**, 301 (2001).
- [7] B. Ruffle, J. Olliver, S. Longeville, R. E. Lechner, *Nucl. Instrum. Methods Phys. Res. A* **449**, 332 (2000).
- [8] A. Amato, *Rev. Mod. Phys.* **69**, 1119 (1997).
- [9] J. R. Christopher, *Annu. Rep. Prog. Chem. Sect. C* **97**, 315 (2001).
- [10] A. E. Pfifer, T. Bowen, K. R. Kendall, *Nucl. Instrum. Methods* **135**, 39 (1976).
- [11] E. Roduner, *Chem. Soc. Rev.* **22**, 337 (1993).
- [12] J. Als-Nielsen, D. McMorrow, *Elements of Modern X-ray Physics*, John Wiley & Sons, Ltd. (2011).
- [13] S. Zhou, A. Brahme, *Physica Medica* **24**, 129 (2008).
- [14] A. Momose, *Jpn. J. Appl. Phys.* **44**, 6355 (2005).

Chapter 3

Small-angle X-ray and Neutron Scattering Analyses of Highly Crosslinked Rubber with Unsaturated Carboxylic acid

3.1 Introduction

Many industries, including the automobile industry, currently require lightweight materials with high tensile strengths and high abrasion resistances to improve the manufacturing of commercial products. Hence, controlling the morphology and structure of functional polymeric materials is indispensable to the development of next-generation materials.

The structure of rubber crosslinked with metal acrylate has been extensively studied because such rubber exhibits strong reinforcement properties without requiring the addition of reinforcing materials such as carbon black, silica or clay. Electron microscopy and scanning probe microscopy measurements of these rubber materials have revealed that metal ions formed aggregates with sizes of 10 - 30 nm [1-4], and these aggregates have been presumed to be responsible for these materials' mechanical properties. Therefore, many studies have focused on the metal ion aggregates in these rubber materials [5-9] with the goal of improving the materials' mechanical properties. However, no dramatic improvement in the mechanical properties has been reported. By contrast, the structure of the matrix rubber, which is a primary component in these rubber materials, has not been studied in detail because of its complexity. Elucidating the structure of the matrix rubber could provide a promising approach to enhancing the mechanical properties of these rubber materials, and we thus

decided to analyze the structure of the matrix rubber. Transverse proton (^1H) NMR relaxation measurements have revealed a strong correlation between the crosslink density in the matrix rubber and the residual dipolar coupling, and this method was therefore applied to characterize the crosslink density of the rubber materials [10-12]. Two relaxation processes were observed in the matrix rubber [13], implying the coexistence of high crosslink density and low crosslink density regions in the matrix rubber. Transmission electron microscopy (TEM) and scanning electron microscopy (SEM) measurements were performed on the matrix rubber to confirm the existence of two regions with different crosslink densities. However, the coexistence of two regions in the matrix rubber was not clarified because of a lack of contrast in the TEM and SEM measurements, which is determined by the difference in the electron densities.

If regions with high crosslink density and low crosslink density coexist in the matrix rubber, the high crosslink density region would swell less than the low crosslink density region when the matrix rubber is immersed in a good solvent. This method must be used to enhance the contrast difference between the high and low crosslink density regions. How can we detect the difference between the regions? In the case of neutron scattering, the contrast is provided by the scattering length density: for example, hydrogen atoms (H) are distinct from deuterium (D) atoms because of their large difference in scattering length. If the (hydrogenated) matrix rubber is swollen in deuterated solvent, it would be possible to distinguish high crosslink density rubber from low crosslink density rubber by using small angle neutron scattering (SANS) measurements. In fact, SANS studies on swollen rubber have successfully revealed the complex structure of rubber materials [14-16], and thus SANS is a promising technique for unveiling the hidden structure of the high crosslink density region in the rubber material.

For our rubber material, it is also necessary to evaluate the structure

and spatial distribution of the metal acrylate to reliably analyze the matrix rubber structure, i.e., we must analyze the structures of both the metal acrylate and the matrix rubber, including high and low crosslink density regions, without ambiguity. Complementary use of small angle X-ray scattering (SAXS) and SANS is suited for this purpose. Specifically, the structure of metal acrylate is analyzed using SAXS measurements, and then the structure of the matrix rubber can be analyzed using SANS and SAXS measurements.

In this Chapter, we investigated the structure of butadiene rubber crosslinked with metal acrylate and primarily focused on determining whether regions of high crosslink density and low crosslink density coexist in the matrix rubber by using SAXS and SANS measurements. By comparing the SAXS and SANS results with the tensile moduli, we also clarified the correlation between the structure and the mechanical properties of the studied rubber materials.

3.2 Experimental

Materials and Sample Preparation

The details of the materials used in the present study are summarized in Table 3.1. We used polybutadiene (BR; BR730, JSR Co., Ltd.) as the matrix rubber. Zinc diacrylate (ZDA; Sanceler SR, Sanshin Chemical Industry Co., Ltd.) and dicumyl peroxide (DCP; Percmyl D, Nichiyu Co., Ltd.) were used as a crosslinking agent and a polymerization initiator of butadiene, respectively. The components were mixed using a 6-inch two-roll mill and molded into sheets 1 mm thick at 170 °C for 20 min (Sample A) and 230 °C for 5 min (Sample B). Prior to the SAXS and SANS measurements, Samples A and B were swollen in toluene and deuterated toluene, respectively, and reached their equilibrium states at room

temperature (final swollen ratio was ~ 300 %). The swollen samples were measured in an optical cell 2 mm thick.

Table 3.1: Details about the components of the samples used in the present study.

	Sample A	Sample B
Polybutadiene / vol%	87.2	87.2
Zinc diacrylate / vol%	11.6	11.6
Dicumyl peroxide / vol%	1.1	1.1
Crosslinking temperature / °C	170	230
Crosslinking time / min	20	5

Measurements

Rubber materials exhibit hierarchical structures over a wide range of spatial scales, and the structures at different spatial scales are intricately correlated to each other. Hence, investigating the structure of rubber materials over a wide range of spatial scales is indispensable for clarifying the correlations between a rubber material's structure and its mechanical properties. Hence, we studied the structure of rubber over a wide q range using SAXS and SANS.

SAXS measurements were performed using BL03XU and BL40B2 instruments installed at a synchrotron radiation (SR) X-ray scattering facility, SPring-8, in Nishiharima, Japan. The incident wavelength of the X-ray and the sample-to-detector distance were 1.5 Å and 3.0 m, respectively. Ultra small-angle X-ray scattering (USAXS) measurements were also performed using a BL19B2 instrument installed at SPring-8, and the incident wavelength of the X-ray and the sample-to-detector distance were 0.69 Å and 41 m, respectively. By combining the SAXS and USAXS

measurements, we can cover a q range from 4.6×10^{-3} to $8.7 \times 10^{-1} \text{ nm}^{-1}$. The two-dimensional (2D) scattering images were circularly averaged to obtain one-dimensional (1D) scattering curves, which were corrected for the backgrounds from the sample cell and the air and for the transmittance of the X-rays through the samples.

SANS measurements were performed using a SANS-J-II spectrometer installed at the Japan Research Reactor-3 (JRR-3) in Tokai, Japan. The wavelength λ of the incident neutron and its distribution ($\Delta\lambda/\lambda$) were 6.56 \AA and 0.11 , respectively. The SANS measurements were performed using sample-to-detector distances of 2.5 m and 10 m , and we also used a focusing lens to obtain a lower q region than that covered by the conventional set-up. Using this set-up, the q values ranged from 8.5×10^{-3} to 1.2 nm^{-1} . The observed 2D scattering images were circularly averaged to obtain 1D scattering curves, which were corrected for the backgrounds from the sample cell and the air, the electronic noise, the detector sensitivity, the transmittance of the neutrons through the samples and incoherent scattering. The SANS scattering intensity ($I(q)$) was converted to an absolute intensity scale (cm^{-1}) using a porous aluminum plate as a secondary standard [17].

Scanning electron microscopy (SEM) and transmission electron microscopy (TEM) measurements were performed at operating voltages of 15 kV and 200 kV , respectively. Tensile measurements were performed using a tensile tester with a cross-head speed of 200 mm/min at room temperature.

3.3 Results and Discussion

A large number of micrometer-scale particles were observed in both Sample A and Sample B in the SEM measurements, as shown in Figure 3.1. The ZDA monomer has a diameter of approximately 1.4 nm , so the particles

observed through SEM were ZDA aggregates. Image analysis reveals that the average diameters of the ZDA aggregates in Samples A and B were 1.8 μm and 3.3 μm , respectively. In order to observe the morphology on a smaller spatial scale, we also performed TEM measurements on the samples. The matrix BR areas exhibiting no ZDA aggregates on the micrometer scale were selected for the TEM measurements. Two types of ZDA aggregates with diameters of ~ 5 nm (1st ZDA aggregates) and ~ 20 nm (2nd ZDA aggregates) were observed in the TEM images, as shown in Figure 3.2.

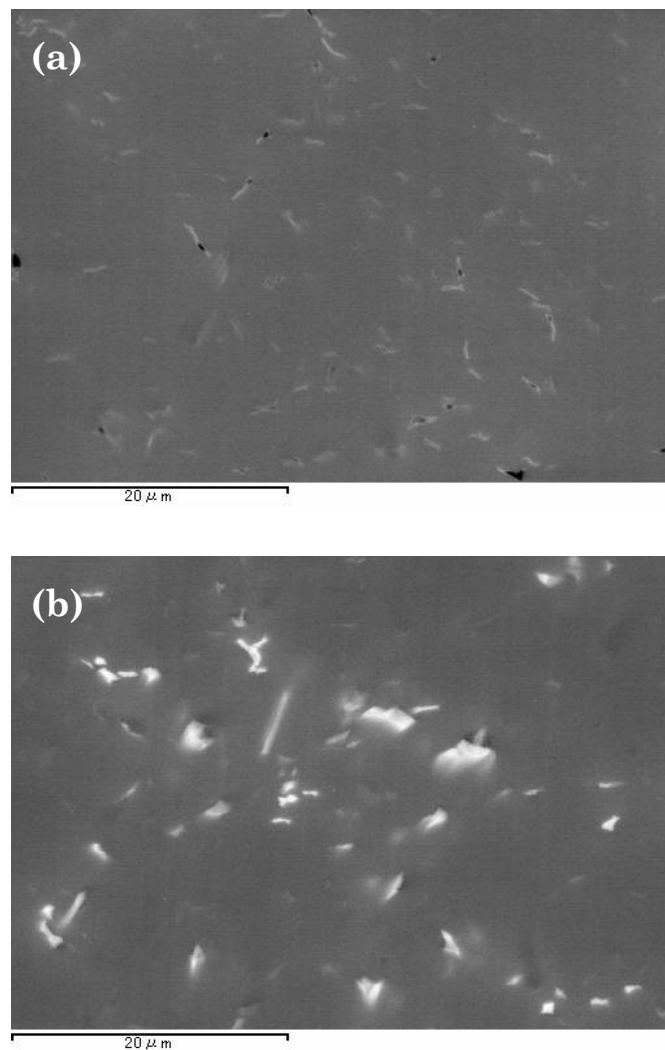


Figure 3.1: SEM images of (a) Sample A and (b) Sample B.

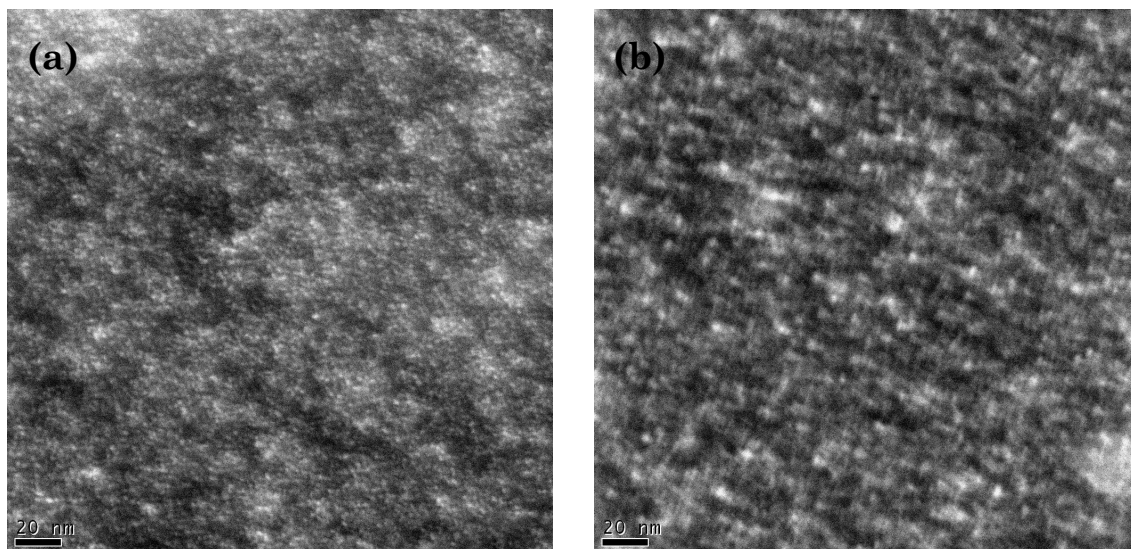


Figure 3.2: TEM images of (a) Sample A and (b) Sample B.

Although it is difficult to accurately analyze the TEM and SEM images because of their limited spatial resolutions, it is safe to say that the ZDA aggregates exhibit a wide distribution of sizes or a hierarchical structure over a wide range of spatial scales in both Samples A and B. The number of ZDA aggregates seems to be larger in Sample A than in Sample B. The difference in ZDA aggregation in terms of size and number might be related to differences in the mechanical properties of Sample A and Sample B, which will be discussed later.

The scattering length density and the electron density of each component in the samples and solvents (toluene and deuterated toluene) are listed in Table 3.2. In the SAXS measurements, it is assumed that the scattering intensity from ZDA dominates the total scattering intensity because the difference in the electron densities of ZDA and toluene is much larger than the difference between the electron densities of the matrix BR

and toluene. If some regions of the matrix BR have higher crosslink densities than the rest, these higher crosslink density regions will not swell in deuterated toluene as much as the lower density regions, resulting in a difference in the scattering length densities. As a result, the difference in the crosslink density will be observable in the SANS profile through the difference in the scattering length density between the high crosslink density region and the deuterated toluene. To verify the assumptions mentioned above, we focus on the experimentally obtained SAXS and SANS scattering profiles.

Table 3.2: Scattering length densities and electron densities of the materials used in the present study.

	Scattering Length Density ($\times 10^{-6} \text{ \AA}^{-2}$)	Electron Density ($\times 10^{23} \text{ electron cm}^{-3}$)
Polybutadiene	0.42	3.01
Zinc diacrylate	2.15	4.83
Toluene	0.94	2.83
Deuterated toluene	5.16	2.82

The intensity profiles $I(q)$ of SAXS ($I_{\text{SAXS}}(q)$) and SANS ($I_{\text{SANS}}(q)$) from Sample A are shown in Figure 3.3 (a) and those from Sample B are shown in Figure 3.3 (b). The $I_{\text{SAXS}}(q)$'s were shifted vertically to overlap with the $I_{\text{SANS}}(q)$'s in the q range of $q < 0.01 \text{ nm}^{-1}$ and $q > 0.5 \text{ nm}^{-1}$ for comparison. The difference in $I_{\text{SAXS}}(q)$ and $I_{\text{SANS}}(q)$ is especially observable over the q region ranging from 0.02 to 0.2 nm^{-1} . As we have already explained above, the difference in the SAXS and SANS profiles originates primarily from the coexistence of high and low crosslink density regions in the matrix rubber.

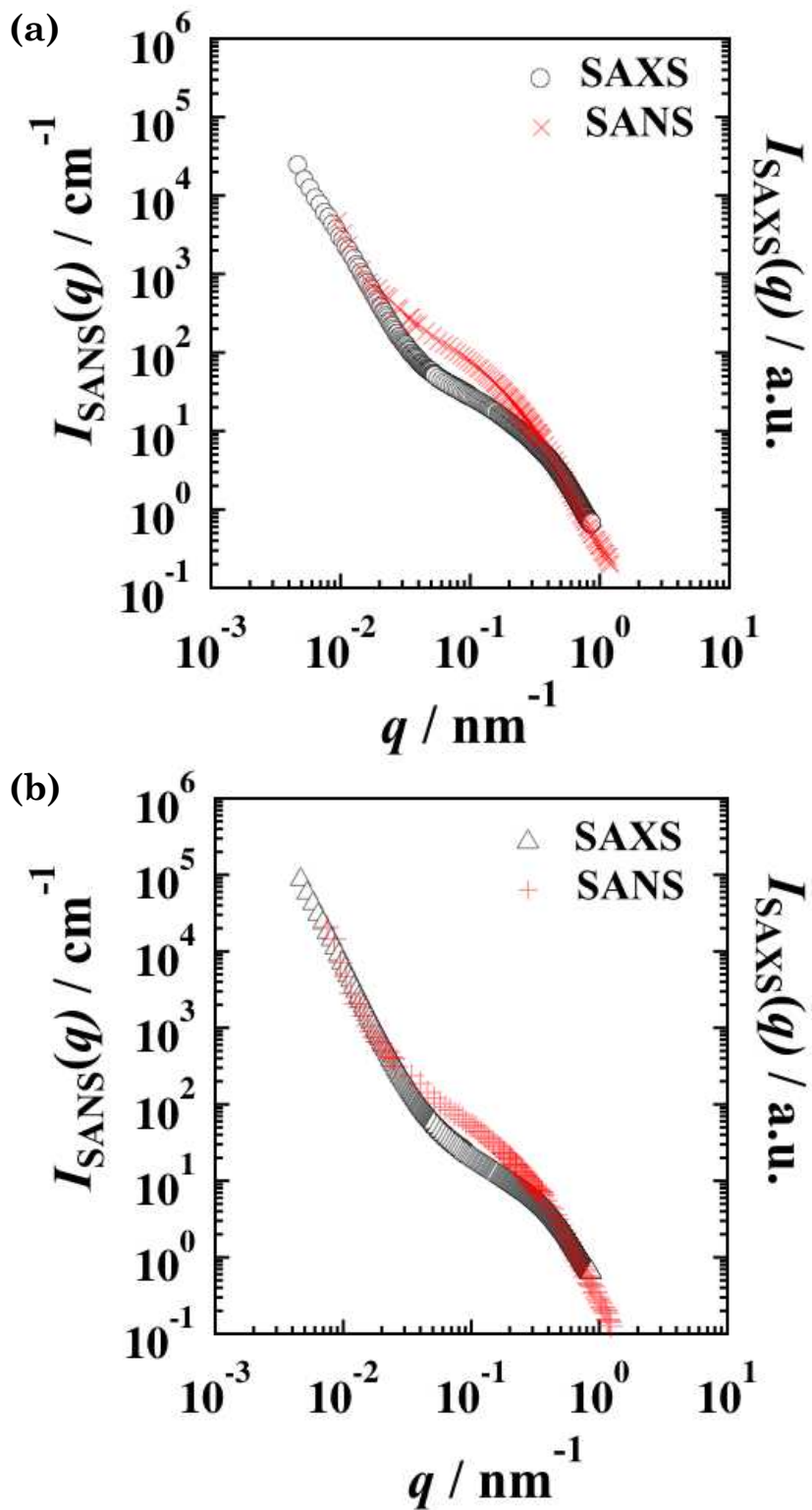


Figure 3.3: SAXS and SANS profiles of (a) Sample A and (b) Sample B.

A model function that considers the hierarchical structure of ZDA aggregates, which were determined from the TEM and SEM images (see Figures 3.1 and 3.2), is used to describe the $I_{\text{SAXS}}(q)$ scattering profiles. The $I(q)$ of rubber in which silica particles are dispersed hierarchically has been successfully analyzed using a *unified approach* [18-21], and we also applied the model given by Eq. (3.1) as a trial.

$$\begin{aligned}
I(q) = & P_4 \left[\left\{ \text{erf} \left(\frac{qR_{g,4}}{\sqrt{6}} \right) / q \right\} \right]^{F_4} \exp \left(\frac{-q^2 R_{g,4}^2}{3} \right) + G_3 \exp \left(\frac{-q^2 R_{g,BR}^2}{3} \right) + P_3 \left[\left\{ \text{erf} \left(\frac{qR_{g,BR}}{\sqrt{6}} \right) / q \right\} \right]^{F_{BR}} + G_2 \exp \left(\frac{-q^2 R_{g,ZDA2}^2}{3} \right) \\
& + P_2 \left[\left\{ \text{erf} \left(\frac{qR_{g,ZDA2}}{\sqrt{6}} \right) / q \right\} \right]^{F_2} \exp \left(\frac{-q^2 R_{g,ZDA1}^2}{3} \right) + G_1 \exp \left(\frac{-q^2 R_{g,ZDA1}^2}{3} \right) + P_1 \left[\left\{ \text{erf} \left(\frac{qR_{g,ZDA1}}{\sqrt{6}} \right) / q \right\} \right]^{F_1} \quad (3.1)
\end{aligned}$$

$$\text{erf}(x) = \frac{2}{\sqrt{\pi}} \int_0^x e^{-t^2} dt \quad (3.2)$$

where $R_{g,ZDA1}$, $R_{g,ZDA2}$, $R_{g,BR}$ and $R_{g,4}$ are the radii of gyration of the 1st ZDA aggregates, the 2nd ZDA aggregates, the high crosslink density BR (HC-BR) and the larger ZDA aggregates, respectively, and R_g is defined as the root mean square distance of the object's points from its center of gravity. $\text{erf}(x)$ in Eq. (3.1) corresponds to the error function, which is also known as the Gaussian error function and is defined in Eq. (3.2). We did not consider cross-terms between the ZDA aggregates and the HC-BR or between ZDA aggregates of different size in Eq. (3.1). We tentatively used values of 1.8 μm and 3.3 μm for $R_{g,4}$, which were determined from the SEM images of Sample A and Sample B, respectively. The size of $R_{g,4}$ is out of the accessible q range in the present USAXS and SAXS measurements. F_1 , F_2 , F_{BR} and F_4 are, the mass-fractal dimensions of the 1st ZDA aggregates, the 2nd ZDA aggregates, the HC-BR and the larger ZDA aggregates, respectively.

G_1 , G_2 , and G_3 are the exponential prefactors and P_1 , P_2 , P_3 and P_4 are the power law prefactors [19-21].

In practice, we have to include the scattering contributions from the low crosslink density rubber in Eq. (3.1). The swelling ratio of the present rubber materials (Sample A and Sample B) in deuterated toluene was estimated to be approximately 300 %, suggesting a large fraction of low crosslink density rubber (LC-BR) in the matrix rubber. The scattering contrast of SANS is generally given by the square of the difference between the average scattering length density and that of the component. If we assume that the average scattering length density of the matrix rubber is almost equal to that of LC-BR, then the scattering intensity of the matrix rubber is dominated by that of the HC-BR. We ignore the scattering contribution from the LC-BR in Eq. (3.1) in a first trial.

Figure 3.4 (a) and (b) show the results of fits of the $I_{\text{SAXS}}(q)$ distributions of Samples A and B, respectively, to Eq. (3.1). The observed and calculated $I_{\text{SAXS}}(q)$ agree fairly well, indicating that the *unified approach* can describe the obtained scattering curves. Hence, we decided to apply the *unified approach* in further analysis of the SAXS and SANS scattering curves. We found that G_3 was nearly equal to zero ($G_3 \approx 0$), implying that the scattering contribution from HC-BR is negligible in the SAXS profiles. This finding supports our initial assumption that the total SAXS intensity is dominated by the scattering from the ZDA aggregates. The fit values of $R_{g,\text{ZDA1}}$ and $R_{g,\text{ZDA2}}$ are 5.0 nm and 14.0 nm for Sample A, respectively, and 4.8 nm and 19.4 nm for Sample B, respectively.

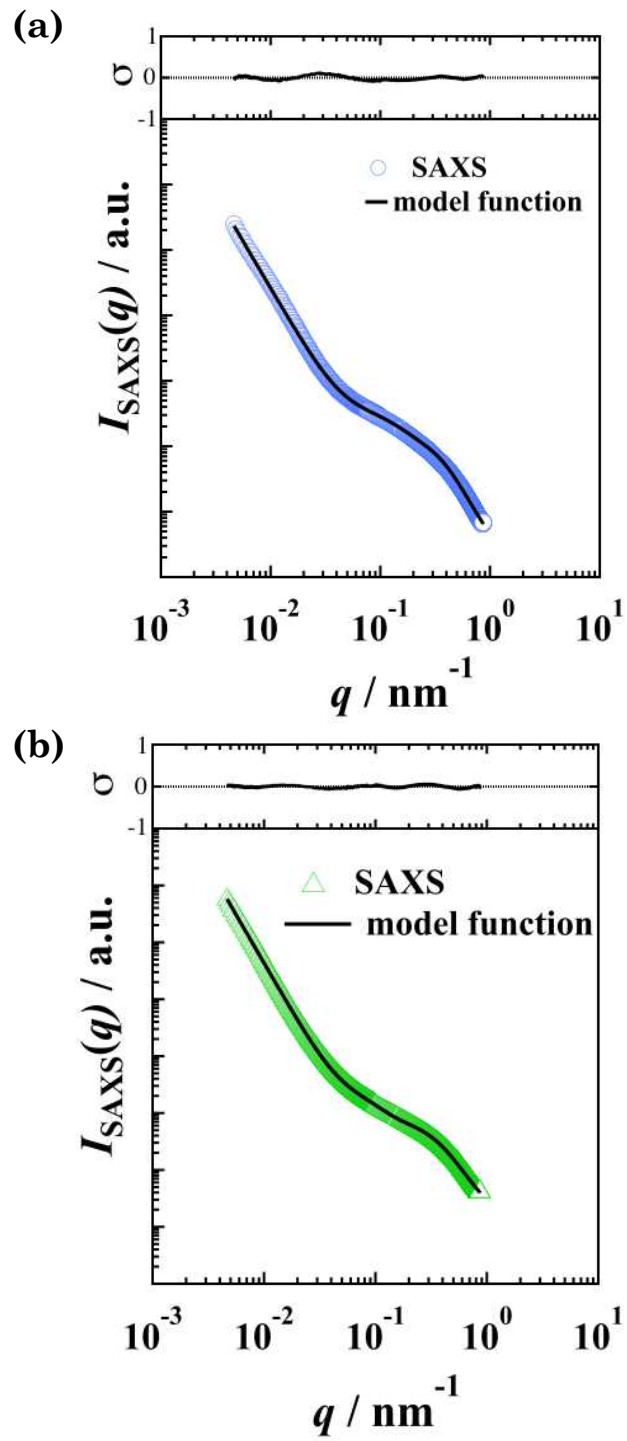


Figure 3.4: SAXS profiles of (a) Sample A and (b) Sample B. The solid lines are the results of fits to the model function, and σ corresponds to the residuals.

For the curve fits to the SANS profiles, we used the values of $R_{g,ZDA1}$ and $R_{g,ZDA2}$ determined from SAXS analysis and $R_{g,4}$ from the SEM images. As noted above, we were able to observe systematic deviations in the scattering curves of the SANS and SAXS profiles in the q range from 0.02 to 0.2 nm⁻¹, and these deviations surely indicate the scattering contribution of HC-BR in the SANS profiles. We would like to demonstrate that the HC-BR component is necessary to quantitatively reproduce the SANS profiles, and so we tried to fit the *unified approach* function (Eq. (3.1)) to the SANS profiles without including the HC-BR contribution ($G_3 = 0$). The best fits to $I_{SANS}(q)$ under the constraint that $G_3 = 0$ are shown in Figure 3.5 (a) and (b), respectively, and severe deviations were observed over the q range 2×10^{-2} to 1×10^{-1} nm⁻¹, implying that the HC-BR contribution is necessary to quantitatively reproduce the SANS profiles. We then fitted the model function (Eq. (3.1)) to $I_{SANS}(q)$ including the contribution of HC-BR ($G_3 \neq 0$) and found that $I_{SANS}(q)$ was well fitted to Eq. (3.1) over the entire studied q range for both Sample A and Sample B, as shown in Figure 3.5 (a) and (b), respectively. As stated above, we neglected the scattering contribution from the low crosslink density rubber (LC-BR) in the model function because of the small contrast between the swollen rubber and the deuterated toluene. The results of the fits to the SANS profiles without this contribution are quite satisfactory, supporting our initial assumption regarding the LC-BR.

In addition to evaluating the size of the HC-BR, the SANS analysis also determines the number densities (N) of the ZDA aggregates and the HC-BR from G_1 , G_2 and G_3 because $I_{SANS}(q)$ was measured on an absolute scale. G_1 , G_2 and G_3 are related to the number densities (N) through the following equations.

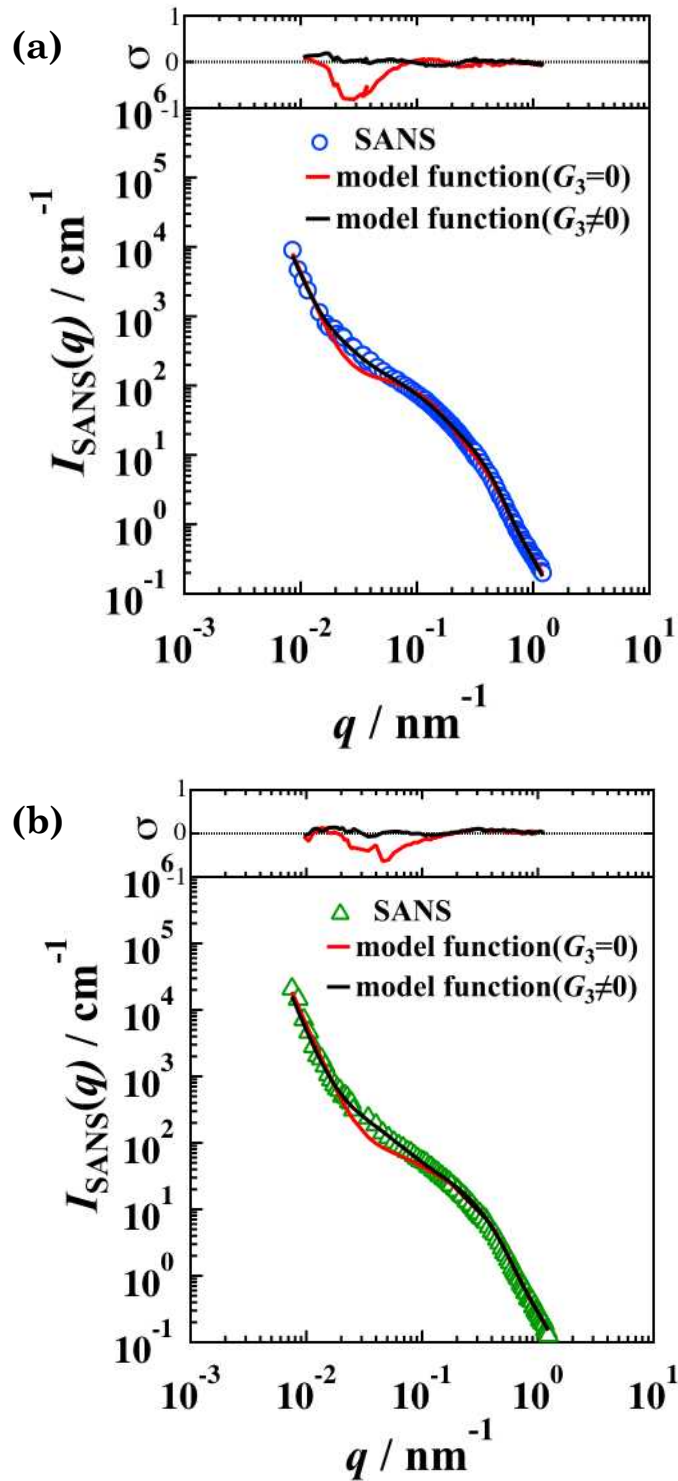


Figure 3.5: SANS profiles of (a) Sample A and (b) Sample B. The red solid lines and black solid lines are the results of fits to the model function without the HC-BR component ($G_3=0$) and that with the HC-BR component, respectively. σ corresponds to the residuals.

$$G_1 = N_{ZDA1} V_{ZDA1}^2 \Delta\rho_{ZDA}^2 \quad (3.3)$$

$$G_2 = N_{ZDA2} V_{ZDA2}^2 \Delta\rho_{ZDA}^2 \quad (3.4)$$

$$G_3 = N_{BR} V_{BR}^2 \Delta\rho_{BR}^2 \quad (3.5)$$

N_{ZDA1} , N_{ZDA2} and N_{BR} are the number densities of the 1st ZDA aggregates, the 2nd ZDA aggregates and the HC-BR, respectively. V_{ZDA1} , V_{ZDA2} and V_{BR} are the volumes of the 1st ZDA aggregates, the 2nd ZDA aggregates and the HC-BR per unit volume, respectively. $\Delta\rho_{ZDA}$, $\Delta\rho_{BR}$ are the differences between the scattering length densities of ZDA and the average scattering length density and between BR and the average, respectively. The average scattering length density is evaluated considering the components of the rubber material summarized in Table 3.2. We have evaluated the number densities of the ZDA aggregates based on the results of these fits. We could not explicitly evaluate the number density of HC-BR because of a lack of knowledge about the degree of swelling of HC-BR. Hence, we only determined the minimum number density of HC-BR ($N_{BR, \min}$) as a reference by assuming that the scattering length density of HC-BR was the same as that of BR. The evaluated number densities of the ZDA aggregates, $N_{BR, \min}$, the R_g 's, the power law exponents and other evaluated parameters are summarized in Table 3.3 for both Sample A and Sample B. $R_{g,ZDA1}$ and N_{ZDA1} were identical between Samples A and B independent of the crosslinking temperature (see Table 3.1). By contrast, a clear difference between Sample A and Sample B was observable in the structural information about the 2nd ZDA aggregates and the HC-BR. Specifically, the $R_{g,ZDA2}$ and $R_{g,BR}$ values of Sample A were smaller than those of Sample B, and the N_{ZDA2} and $N_{BR, \min}$ values of Sample A were larger than those of Sample B. We could not determine clear differences between the power law

exponents of the ZDA aggregates and the HC-BR of Sample A and Sample B, and the physical meaning of the power law exponent is unclear from the present analysis outside of Porod's region ($I(q) \sim q^{-4}$) for larger ZDA aggregates.

Table 3.3: Radii of gyration (R_g), number densities (N), power law exponents of each component and other parameters obtained from the fits for Sample A and Sample B.

	Sample A	Sample B
$R_{g,ZDA1} / \text{nm}$	5.0	4.8
$R_{g,ZDA2} / \text{nm}$	14.0	19.4
$R_{g,BR} / \text{nm}$	72.2	109.2
N_{ZDA1} / cm^3	7.5×10^{16}	6.1×10^{16}
N_{ZDA2} / cm^3	1.1×10^{15}	1.3×10^{14}
$N_{BR,\min} / \text{cm}^3$	3.0×10^{11}	7.0×10^{10}
P_1	2.4×10^{-4}	2.0×10^{-4}
P_2	1.5×10^{-3}	1.6×10^{-2}
P_3	1.4×10^{-1}	5.6×10^{-3}
P_4	8.1×10^{-9}	6.8×10^{-9}
G_1	17.3	11.7
G_2	79.9	74.4
G_3	6.2×10^2	1.3×10^3
F_1	3.1	3.2
F_2	1.8	1.8
F_{BR}	1.8	1.8
F_4	3.9	4.0

The minimum number density ($N_{BR,\min}$) of HC-BR was determined instead of the exact number density.

To determine the correlations between the structural information elucidated from the SAXS and SANS measurements and the mechanical properties of the present rubber materials, we studied the elastic moduli of both of the samples. Figure 3.6 presents the stress-strain curves of Sample A and Sample B. The stress increases linearly with the strain in the low strain region (strain < 0.05) and begins to increase more slowly in the high strain region (strain > 0.05), which is typical behavior for rubber. The tensile modulus was calculated in the linear viscoelastic region (strain < 0.05). The calculated moduli of Samples A and B are 48.4 MPa and 22.8 MPa, respectively. The modulus of Sample B, which was crosslinked at a higher temperature than Sample A, is lower than that of Sample A, indicating that the crosslinking temperature is a factor controlling the modulus.

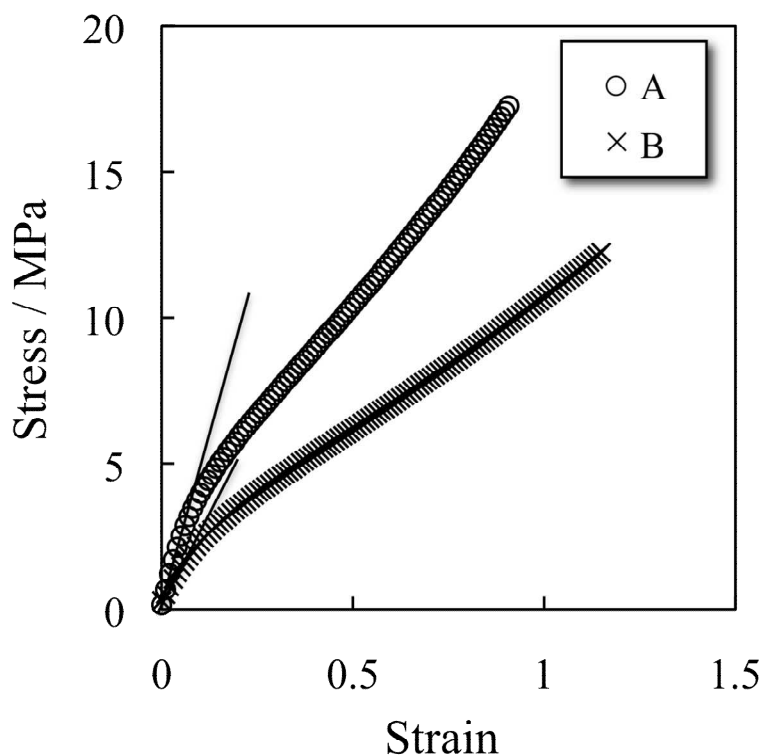


Figure 3.6: Strain dependence of stress in Samples A and B. The solid lines were used to calculate the elastic moduli.

As stated above, we did not discover any clear difference in the sizes and the number densities of the 1st ZDA aggregates of Samples A and B, so it seems that the structures of the 2nd ZDA aggregates and the HC-BR are related to the difference in the elastic moduli. The 2nd ZDA aggregates in Sample A are smaller in size and larger in number density than in Sample B, suggesting that the ZDA aggregates were crushed into a larger number of smaller aggregates prior to the crosslinking reaction. This difference arises because Sample A was molded at a lower temperature (170 °C) than Sample B (230 °C), and the crosslinking reaction thus occurred more slowly in Sample A than in Sample B, allowing the ZDA to be crushed into a larger number of smaller aggregates in Sample A. In addition, the distribution of the 2nd aggregates in Sample A looks more homogeneous than that of Sample B, as shown in Figure 3.2. The homogeneous distribution of small particles may reduce the possibility of stress concentration. A similar tendency was observed in the size and number density of the HC-BR: the size is smaller and the $N_{BR, \min}$ is larger in Sample A than in Sample B. The 2nd ZDA aggregates most likely affect the formation of the HC-BR. The ZDA aggregates are speculated to act as a kind of core for the BR, resulting in the formation of high crosslink density rubber around the ZDA aggregates. In order to discuss the correlation between the ZDA aggregates and the HC-BR in more detail, we must evaluate the partial scattering function, which can directly reveal correlations between the ZDA aggregates and the HC-BR by using contrast variation SANS [22].

3.4 Conclusion

In this Chapter, we investigated the structure of butadiene rubber crosslinked with metal acrylate (ZDA) using SAXS and SANS, focusing on whether high crosslink density and low crosslink density regions coexisted in

the matrix rubber. The SAXS profiles of the rubber materials swollen with toluene were well fitted using the *unified approach* model and considering only the hierarchical structure of the ZDA aggregates. By contrast, the SANS profiles of the rubber materials swollen with deuterated toluene were not well described by a model that considered only the contribution of the hierarchical structure of ZDA aggregates, suggesting that high crosslink density rubber (HC-BR) must be considered to reproduce the SANS profiles. Then, considering both the contributions from the HC-BR and the ZDA aggregates, we were able to describe the SANS profiles very well, and for the first time successfully clarified the structure of HC-BR through complementary use of SAXS and SANS. Comparing the results of the tensile measurements with the structural information determined using SAXS and SANS revealed that the structures of the HC-BR and the 2nd ZDA aggregates are related to the mechanical properties of the rubber materials. Taking these findings together, the size and the number density of the HC-BR and the 2nd ZDA aggregates are related to the mechanical strength of the rubber materials studied herein.

References

- [1] N. Nagata, T. Sato, T. Fujii, Y. Saito, *J. Appl. Polym. Sci.* **53**, 103 (1994).
- [2] X. Yuan, Y. Zhang, Z. Peng, Y. Zhang, *J. Appl. Polym. Sci.* **84**, 1403 (2002).
- [3] Z. Wei, Y. Lu, S. Yan, Y. Meng, L. Zhang, *J. Appl. Polym. Sci.* **124**, 288 (2012).
- [4] Z. Wei, Y. Lu, Y. Meng, L. Zhang, *Polymer* **53**, 1409 (2012).
- [5] B. J. Chu, D. Q. Wu, R. D. Lundberg, W. J. Macknight, *Macromolecules* **26**, 994 (1993).
- [6] Y. Tsujita, M. Yasuda, M. Takei, T. Kinoshita, A. Takizawa, H.

- Yoshimizu, *Macromolecules* **34**, 2220 (2001).
- [7] M. Al-Hussein, B. G. G. Lohmeijer, U. S. Schubert, W. H. de Jeu, *Macromolecules* **36**, 9281 (2003).
- [8] C. N. Zhou, D. C. Chan, I. K. Winey, *Macromolecules* **41**, 6134 (2008).
- [9] E. M. Seitz, D. C. Chan, L. K. Opper, W. T. Baughman, B. K. Wagener, I. K. Winey, *J. Am. Chem. Soc.* **132**, 8165 (2010).
- [10] H. Luo, M. Klüppel, H. Schneider, *Macromolecules* **37**, 8000 (2004).
- [11] C. A. Steren, G. A. Monti, *Macromolecules* **37**, 5624 (2004).
- [12] S. Hayashi, Y. Komori, *Solid State Nucl. Mag.* **36**, 167 (2009).
- [13] K. Shiga, R. Murakami, T. Shigemitsu, H. Kimura, T. Kitago, Golf ball material and golf ball patent appl. No. 207716(JP) (2011).
- [14] M. Takenaka, S. Nishituji, N. Amino, Y. Ishikawa, D. Yamaguchi, S. Koizumi, *Macromolecules* **42**, 308 (2009).
- [15] Y. Ikeda, N. Higashitani, K. Hijikata, Y. Kukubo, Y. Morita, M. Shibayama, N. Osaka, T. Suzuki, H. Endo, S. Kohjiya, *Macromolecules* **42**, 2741 (2009).
- [16] T. Suzuki, N. Osaka, H. Endo, M. Shibayama, Y. Ikeda, H. Asai, N. Higashitani, Y. Kokubo, S. Kohjiya, *Macromolecules* **43**, 1556 (2010).
- [17] T. P. Russell, J. S. Lin, S. Spooner, G. D. Wignall, *J. Appl. Cryst.* **21**, 629 (1988).
- [18] H. Kishimoto, Y. Shinohara, Y. Amemiya, K. Inoue, Y. Suzuki, A. Takeuchi, K. Uesugi, N. Yagi, *Rubber Chem. Technol.*, **81**, 541 (2008).
- [19] G. Beaucage, *J. Appl. Cryst.* **28**, 717 (1995).
- [20] G. Beaucage, *J. Appl. Cryst.* **29**, 134 (1996).
- [21] G. Beaucage, H. K. Kammler, S. E. Pratsinis, *J. Appl. Cryst.* **37**, 523 (2004).
- [22] H. Endo, M. Mihalescu, M. Monkenbusch, J. Allgaier, G. Gompper, D. Richter, B. Jakos, T. Sottmann, R. Strey, I. Grillo, *J. Chem. Phys.* **115**, 580 (2001).

Chapter 4

Structure Analyses of Polybutadiene Rubber Crosslinked with Unsaturated Carboxylate using Contrast Variation Small-angle Neutron Scattering

4.1 Introduction

In Chapter 3, we investigated the structure of butadiene rubber crosslinked with metal acrylate (ZDA) by the complementary use of small-angle x-ray scattering (SAXS) and small-angle neutron scattering (SANS). In the experiment the rubber materials were swollen in a good solvent. Assuming that the degree of swelling for high and low crosslink density regions would be different, we revealed the coexistence of high and low crosslink density regions in the rubber matrix. Based on the SAXS and SANS results, it was expected that the high crosslink density BR (HC-BR) region was absorbed on the surface of metal ion aggregates. However, we have not experimentally confirmed this expectation. Therefore, another experimental approach is necessary to confirm the expectation and essential to understand the structure and physical properties of HC-BR in more detail.

The contrast variation SANS (CV-SANS) method is a powerful tool for structural analyses of multicomponent systems such as clay-polymer and silica-polymer composite systems [1-5]. In this method partial scattering functions in multicomponent systems can be evaluated, which is a great advantage in the study on structure of multicomponent system. As mentioned in Chapter 2, the self-terms are always positive, on the other hand, the cross-terms may be either positive or negative, depending on the

interaction between the components. Using this advantage, Endo et al. determined whether or not a polymer was absorbed on the surface of nanocomposites [5].

In this Chapter, we perform CV-SANS measurements on butadiene rubber crosslinked with metal acrylate (ZDA) to elucidate the structure of HC-BR. In addition we also investigate the structural relationship between the metal ion aggregates and the HC-BR region as well as the hierarchical structure of metal aggregates and the network structures in matrix BR were also investigated using CV-SANS.

4.2 Experimental

Materials and Sample Preparation

The details of the materials used in this study are summarized in Table 4.1. We used polybutadiene (BR; BR730, JSR Co., Ltd.) with weight-average molecular weight (M_w) of 6.72×10^5 and molecular weight distribution index (M_w/M_n) of 2.39, where M_n is number-average molecular weight as the rubber matrix. The content of *cis*, *trans* and *vinyl* in the BR was 97, 2 and 1%, respectively. Zinc diacrylate (ZDA; Sanceler SR, Sanshin Chemical Industry Co., Ltd.) and dicumyl peroxide (DCP; Percmyl D, Nichiyu Co., Ltd.) were used as a crosslinker and an initiator, respectively, in the crosslinking reaction. BR, ZDA and DCP with a volume ratio of 87.3, 12.4 and 0.3, respectively, were placed into a 6-inch two-roll mill simultaneously and mixed for 5 minutes at room temperature. After mixing at room temperature, the mixture consisting of BR, ZDA and DCP was placed into a mold and heated at 170 °C for 20 minutes to promote the chemical reaction. Prior to the SANS and SAXS measurements, the samples were swollen in a mixed solvents containing hydrogenated toluene

(*h*-toluene) and deuterated toluene (*d*-toluene) until their equilibrium states were reached at room temperature (final swollen ratio was ~ 196 %). The swollen samples were measured in a quartz cell that was 2 mm thick. For the TEM observation, the sample, which had a thickness of 50 nm, was prepared using a microtome.

Table 4.1: Characteristics of the components of the samples used in the current study.

Polybutadiene (vol%)	87.3
Zinc diacrylate (vol%)	12.4
Dicumyl peroxide (vol%)	0.3

Measurements

The SANS measurements were performed with a 40m SANS spectrometer installed at a neutron scattering facility (HANARO) in Daejeon, Korea. The wavelength (λ) of the incident neutron and its distribution ($\Delta\lambda/\lambda$) were 7.49 Å and 0.12, respectively. In addition to the three different sample-to-detector distances of 1.16 m, 4.7 m and 19.95 m, a focusing lens was also utilized to access a lower q region than that covered by the normal set-up. Using this set-up, the q values ranged from 2.0×10^{-2} to 7.5×10^{-1} nm $^{-1}$. The observed 2D scattering images were circularly averaged to obtain 1D scattering curves, which were corrected for the backgrounds from the sample cell and air, electronic noise, detector sensitivity, transmittance of the neutrons through the samples and incoherent scattering. The SANS scattering intensity was converted to an absolute intensity scale (cm $^{-1}$) using the direct beam flux method.

SAXS measurements were also conducted on the same samples. The SAXS measurements were performed using a BL03XU instrument installed at a synchrotron radiation (SR) X-ray scattering facility (SPring-8) in

Nishiharima, Japan, and the incident wavelength of the X-ray and the sample-to-detector distance were 1.5 Å and 3.0 m, respectively. Ultra small-angle X-ray scattering (USAXS) measurements were also performed with a BL20XU instrument installed at SPring-8, and the incident wavelength of the X-ray and the sample-to-detector distance were 0.54 Å and 160.5 m, respectively. By combining the SAXS and USAXS measurements, we can cover a q range from 2.9×10^{-3} to $8.7 \times 10^{-1} \text{ nm}^{-1}$. The two-dimensional (2D) scattering images were circularly averaged to obtain one-dimensional (1D) scattering curves, which were corrected for the backgrounds from the sample cell and the air as well as for the transmittance of the X-rays through the samples.

Transmission electron microscopy (TEM) measurements were performed at operating voltages of 200 kV under dark-field mode.

Dynamic viscoelasticity measurements were carried out with a dynamic mechanical analyzer (RSA-G2, TA instruments) at 303 K and 10 Hz.

Differential scanning calorimetry (DSC) measurements were carried out with a differential scanning calorimeter (Q200, TA instruments) for a temperature range of -150 to 150 °C at a rate of 10 °C/min.

4.3 Results and Discussion

Roughly two types of ZDA aggregates with diameters of ~5 nm (1st ZDA aggregates) and ~20 nm (2nd ZDA aggregates) were observed in the TEM image, as shown in Figure 4.1. Because this TEM image was taken in the dark-field mode, the bright particles correspond to ZDA aggregates where the rubber material has a high electron density. Although it is difficult to accurately analyze the TEM image due to its limited spatial resolution, a wide distribution of sizes and a hierarchical structure over a wide range of spatial scales was observed for ZDA aggregates in the BR matrix. In

addition, micrometer-sized ZDA aggregates were also observed in Chapter 3, suggesting the coexistence of nanometer- and micrometer-sized ZDA aggregates in the same sample after the chemical reaction.

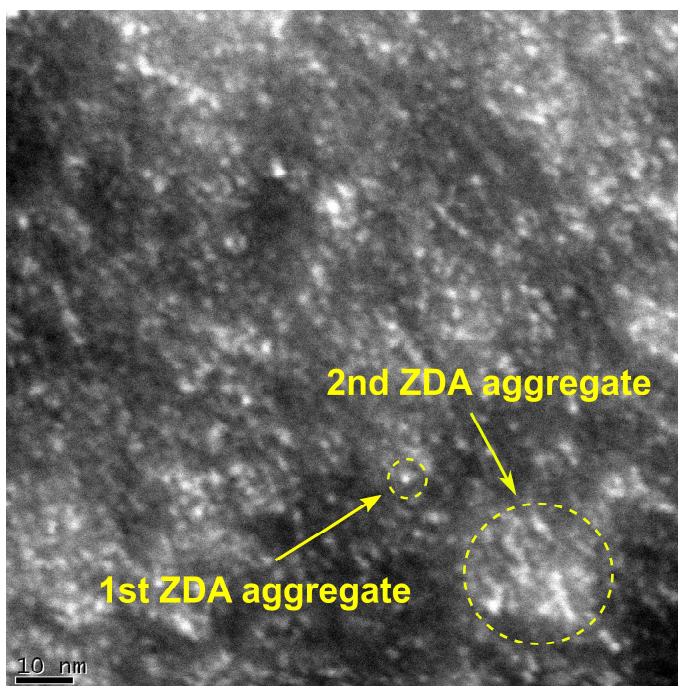


Figure 4.1: TEM image.

Figure 4.2 shows the SANS profiles $I(q)$ of BR crosslinked with ZDA and swollen by toluene consisting of a different mixing ratio of *h*-toluene and *d*-toluene. The Kratky plots ($q^2I(q)$ vs q) are shown in the inset to visualize the change in the q dependence of $I(q)$. The scattering intensity ($I(q)$) tends to decrease with as the ratio of *d*-toluene in toluene solvent decreased, reflecting the decrease in the scattering contrast between BR and the toluene solvent. However, the q dependence of $I(q)$ is strongly dependent on the ratio of *d*-toluene in the toluene solvent. In particular, the q dependence of $I(q)$ swollen by 100% *d*-toluene differs from that swollen by 100% *h*-toluene. If the rubber matrix swells homogeneously in the toluene

solvent, the q dependence of $I(q)$ must be independent of the fraction of d -toluene in the toluene solvent. These experimental results imply that a component other than the ZDA aggregates and BR matrix must exist in the current rubber material.

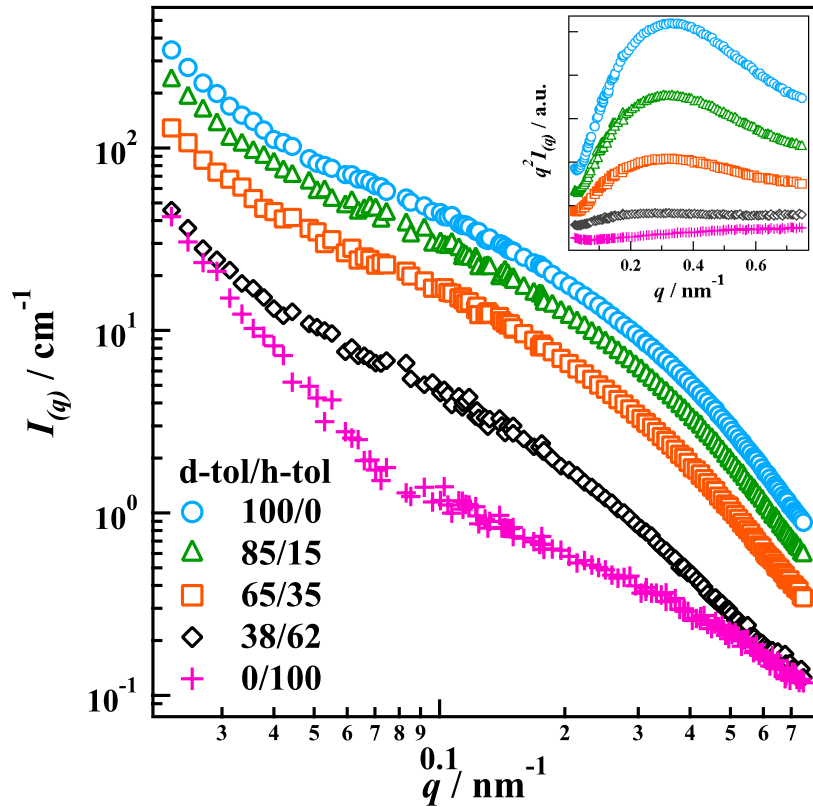


Figure 4.2: SANS profiles for the material swollen in a mixture of d -toluene and h -toluene. The inset shows the Kratky plots of each solvent.

In principle, our samples can be regarded as a four components system consisting of BR, ZDA, DCP and toluene solvent. However, the volume fraction of DCP included in our sample is negligibly small compared to the other components, as shown in Table 4.1. Therefore, our sample can be approximately regarded as three components consisting of BR, ZDA and the toluene solvent. Under such an approximation, $I(q)$ can be expressed as

follows:

$$I(q) = (\sigma_p - \sigma_{sol})^2 S_{pp}(q) + 2(\sigma_p - \sigma_{sol})(\sigma_z - \sigma_{sol}) S_{pz}(q) + (\sigma_z - \sigma_{sol})^2 S_{zz}(q) \quad (4.1)$$

where σ_p , σ_z and σ_{sol} are the scattering length densities of BR, ZDA and the solvent, respectively, as shown in Table 4.2. The scattering length density of the solvent is calculated by considering the mixing ratio of *h*-toluene and *d*-toluene. $S_{pp}(q)$, $S_{zz}(q)$ and $S_{pz}(q)$ are the partial scattering functions of the self-correlation of BR, the self-correlation of the ZDA aggregates and the cross-correlation between the BR and ZDA aggregates, respectively. If the SANS measurements are performed at n different toluene solvents consisting of different mixing ratios of *h*-toluene and *d*-toluene, each $I_j(q)$ ($1 \leq j \leq n$) is related to the ($S_{pp}(q)$, $S_{zz}(q)$ and $S_{pz}(q)$) partial scattering functions as follows:

$$\begin{pmatrix} I_1(q) \\ I_2(q) \\ \vdots \\ I_n(q) \end{pmatrix} = \begin{pmatrix} {}^1\Delta\sigma_p^2 & {}^1\Delta\sigma_p {}^1\Delta\sigma_z & {}^1\Delta\sigma_z^2 \\ {}^2\Delta\sigma_p^2 & {}^2\Delta\sigma_p {}^2\Delta\sigma_z & {}^2\Delta\sigma_z^2 \\ \vdots & \vdots & \vdots \\ {}^n\Delta\sigma_p^2 & {}^n\Delta\sigma_p {}^n\Delta\sigma_z & {}^n\Delta\sigma_z^2 \end{pmatrix} \begin{pmatrix} S_{pp}(q) \\ S_{pz}(q) \\ S_{zz}(q) \end{pmatrix} \quad (4.2)$$

where

$$\Delta\sigma_p = \sigma_p - \sigma_{sol} \quad (4.3)$$

$$\Delta\sigma_z = \sigma_z - \sigma_{sol} \quad (4.4)$$

$S_{pp}(q)$, $S_{zz}(q)$ and $S_{pz}(q)$ can be calculated according to the *singular value decomposition* algorithm [5].

$$\begin{pmatrix} S_{pp}(q) \\ S_{pz}(q) \\ S_{zz}(q) \end{pmatrix} = \begin{pmatrix} {}^1\Delta\sigma_p^2 & {}^1\Delta\sigma_p {}^1\Delta\sigma_z & {}^1\Delta\sigma_z^2 \\ {}^2\Delta\sigma_p^2 & {}^2\Delta\sigma_p {}^2\Delta\sigma_z & {}^2\Delta\sigma_z^2 \\ \vdots & \vdots & \vdots \\ {}^n\Delta\sigma_p^2 & {}^n\Delta\sigma_p {}^n\Delta\sigma_z & {}^n\Delta\sigma_z^2 \end{pmatrix}^{-1} \begin{pmatrix} I_1(q) \\ I_2(q) \\ \vdots \\ I_n(q) \end{pmatrix} \quad (4.5)$$

Table 4.2: Scattering length densities and electron densities of the materials used in the current study.

	Scattering Length Density (x 10 ⁻⁶ Å ⁻²)	Electron Density (x 10 ²³ electron cm ⁻³)
Polybutadiene	0.42	3.01
Zinc diacrylate	2.15	4.83
Toluene	0.94	2.83
Deuterated toluene	5.66	2.82

Figures 4.3(a), (b) and (c) show the calculated partial scattering functions ($S_{ZZ}(q)$, $S_{PP}(q)$ and $S_{PZ}(q)$, respectively). $I(q)$ from the SAXS measurement ($I_{\text{SAXS}}(q)$) is also shown in Figure 4.3(a). Because the difference in the electron density between ZDA and toluene is much larger than those of the other components in the SAXS experiment, as shown in Table 4.2, the scattering intensity from ZDA dominates the total scattering intensity for the SAXS measurements. Under such an assumption, the q dependence of $I_{\text{SAXS}}(q)$ is expected to reproduce the q dependence of $S_{ZZ}(q)$. As shown in Figure 4.3(a), the q dependence of $I_{\text{SAXS}}(q)$ was consistent with that of $S_{ZZ}(q)$, supporting the validity of the evaluation of the partial scattering function. To quantitatively characterize the obtained $S_{PP}(q)$, $S_{ZZ}(q)$ and $S_{PZ}(q)$, an appropriate model should be assumed. The model proposed by Takenaka et al. [2], who studied rubber-silica systems with the

SANS techniques, was employed to model the current rubber material consisting of ZDA aggregates, a HC-BR layer surrounding the ZDA aggregates with a volume fraction of BR in the swollen HC-BR layer with toluene ($\phi_{\text{HC-BR}}$) and the BR matrix with a volume fraction of BR in the swollen matrix BR region with toluene ($\phi_{\text{MT-BR}}$) (Figure 4.5). Based on this model, the partial scattering functions can be described as follows [2]:

$$S_{zz}(q) = F_{ZDA}^2(q) \quad (4.6)$$

$$S_{pz}(q) = (\phi_{\text{HC-BR}} - \phi_{\text{MT-BR}})F_{\text{HC-BR}+ZDA}(q)F_{ZDA}(q) - \phi_{\text{HC-BR}}F_{ZDA}^2(q) \quad (4.7)$$

$$S_{pp}(q) = [(\phi_{\text{HC-BR}} - \phi_{\text{MT-BR}})F_{\text{HC-BR}+ZDA}(q) - \phi_{\text{HC-BR}}F_{ZDA}(q)]^2 + S_{pp,nt}(q) + S_{pp,ih1}(q) + S_{pp,ih2}(q) \quad (4.8)$$

where

$$S_{pp,nt}(q) = \frac{S_{pp,nt}^0(0)}{1 + q^2\xi_1^2} \quad (4.9)$$

$$S_{pp,ih1}(q) = \frac{S_{pp,ih1}^0(0)}{(1 + q^2\xi_2^2)^2} \quad (4.10)$$

$$S_{pp,ih2}(q) = \frac{S_{pp,ih2}^0(0)}{(1 + q^2\xi_3^2)^2} \quad (4.11)$$

$F_{ZDA}(q)$ and $F_{\text{HC-BR}+ZDA}(q)$ are the scattering amplitudes of the ZDA aggregates and the region consisting of ZDA aggregates and the HC-BR layer, respectively. Three correlation lengths due to the crosslinking network, inhomogeneous crosslinking and larger inhomogeneous crosslinking have been reported for similar rubber materials [3, 4]. Therefore, three scattering functions ($S_{pp,nt}(q)$, $S_{pp,ih1}(q)$ and $S_{pp,ih2}(q)$) are introduced to describe the concentration fluctuation of the BR network structure ($S_{pp,nt}(q)$), inhomogeneous crosslinked structure ($S_{pp,ih1}(q)$) and

larger inhomogeneous crosslinked structure ($S_{pp,ih2}(q)$) in the BR matrix region in eq. (4.9). ζ_1 , ζ_2 , ζ_3 , $S_{pp,nt}^0(0)$, $S_{pp,ih1}^0(0)$ and $S_{pp,ih2}^0(0)$ are the correlation lengths of the BR network, the inhomogeneous crosslinked structure and the larger inhomogeneous crosslinked structure in BR matrix region as well as the prefactors of the inhomogeneous crosslinked structure and the larger inhomogeneous crosslinked structure in matrix BR region, respectively.

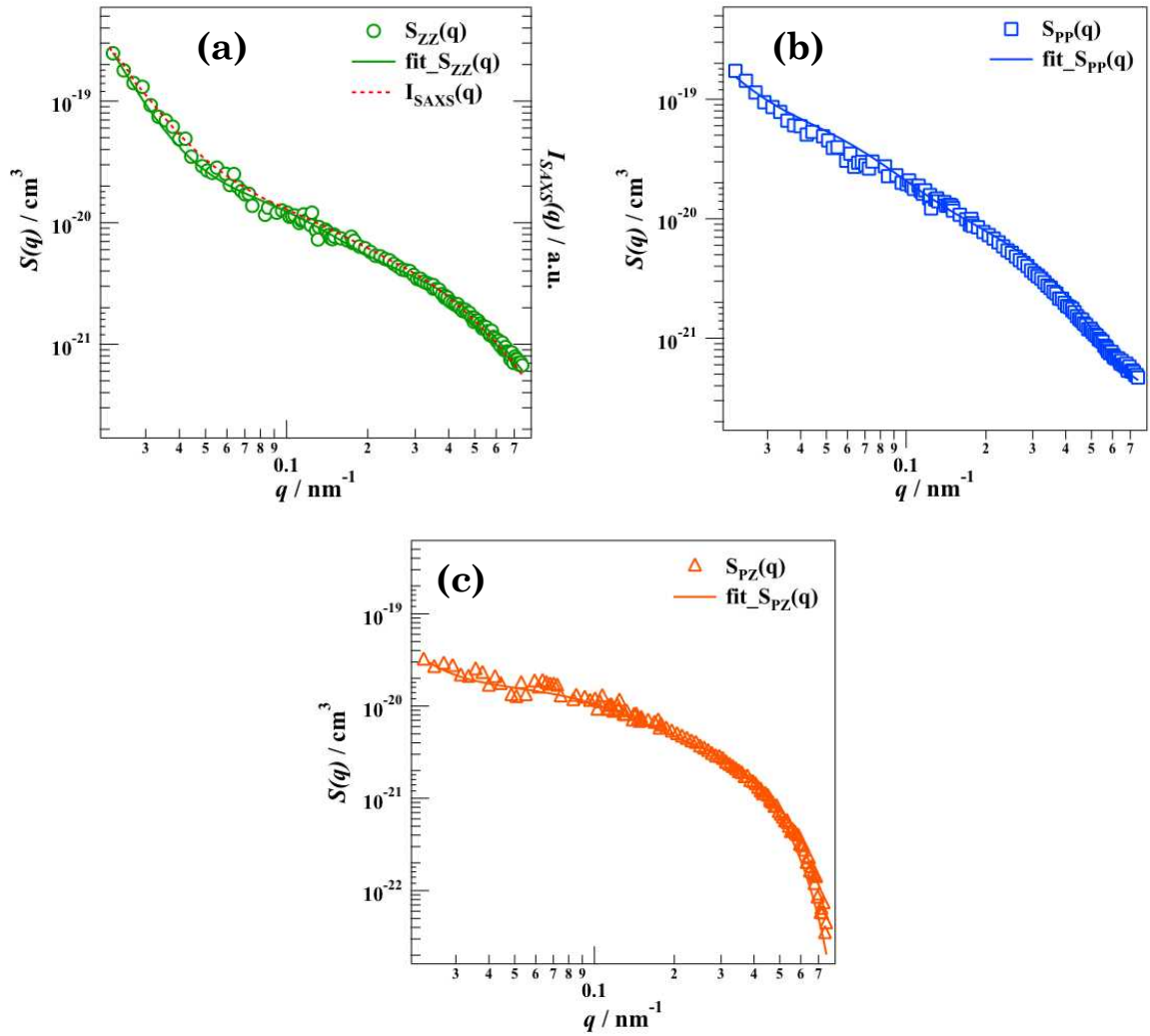


Figure 4.3: Partial scattering functions (a) $S_{ZZ}(q)$, (b) $S_{PP}(q)$ and (c) $S_{PZ}(q)$ obtained using the CV-SANS method. Dashed line in (a) is the SAXS profile. Solid lines represent the results from the fitting with the model function.

Assuming the absence of an absorbed BR layer on the surface of the ZDA aggregates, Eq. (4.7) can be approximated as follows [5]:

$$S_{pz}(q) = -\phi_{MT-BR} F_{ZDA}^2(q) \quad (4.12)$$

In the current experiment, the $S_{pz}(q)$ has a positive sign in the q range examined, implying the possibility of the existence of cross-correlation between BR and ZDA based on structural analysis. Other experimental proof for the existence of an absorbed BR layer on the surface of the ZDA aggregates was obtained from the DSC results (Figure 4.4). The endothermic peak observed at approximately 0 °C originated from the crystal melting peak due to the high *cis* content in the BR matrix. After the chemical reaction with ZDA, new endothermic behavior, which was not detected for the BR matrix (non-crosslinked BR), was observed at approximately 90 °C. It is important to note that the endothermic behavior at 90 °C was not observed for either the ZDA monomer or self-polymerized ZDA [6]. Therefore, the endothermic behavior observed at 90 °C must originate from BR crosslinked with ZDA. The interfacial polymer layer near the impenetrable substrate or nanoparticle exhibits anomalous physical properties, and one representative example is the dramatic increase in the glass transition temperature (T_g) [7, 8]. Then, the endothermic behavior at 90 °C in the rubber material must correspond to the second T_g from the HC-BR layer originating from the crosslinking reaction between BR and ZDA. Based on structural analysis and thermal properties, the existence of a HC-BR layer can be confirmed.

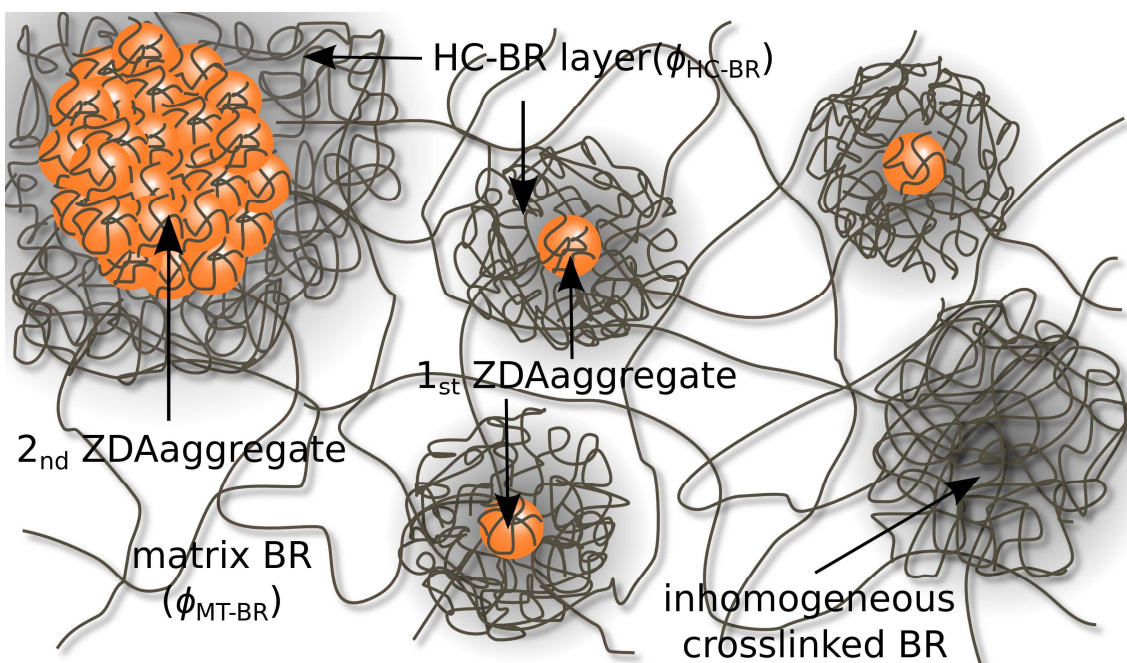


Figure 4.4: Schematic representation of the ZDA/BR system swollen by solvent.

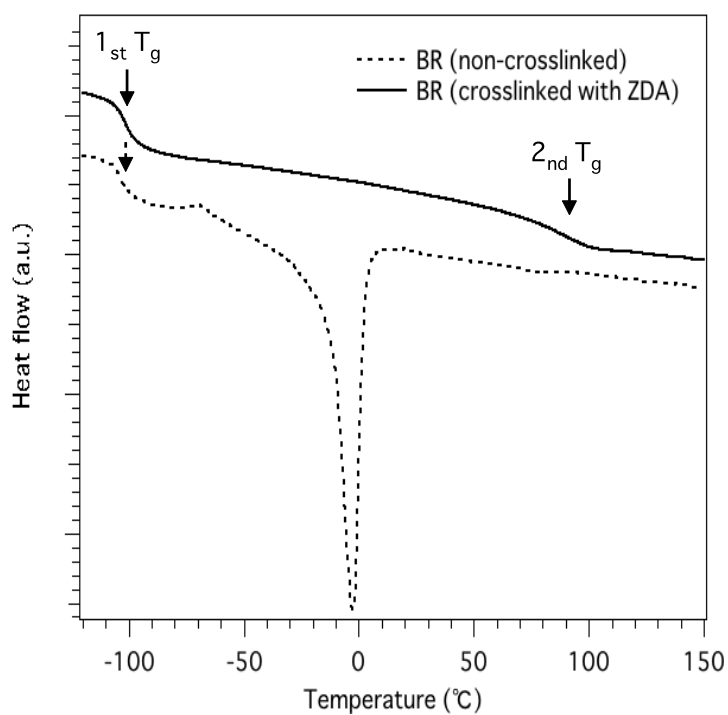


Figure 4.5: DSC curves of non-crosslinked and crosslinked BR.

Based on Chapter 3 TEM and SEM studies on BR crosslinked with ZDA, both the hierarchical structure of the ZDA aggregate and the broad size distributions of the ZDA aggregates have been observed. In addition, the morphologies of the ZDA aggregates were approximately sphere shaped. Therefore, the $S_{ZZ}(q)$ partial scattering function can be expressed by the model function considering the hierarchal structure of the form factor of spheres with broad size distributions.

$$\begin{aligned}
S_{zz}(q) &= |F_{ZDA}(q)|^2 \\
&= n_{ZDA3} \int_0^\infty P(r, r_{0,ZDA3}, \sigma_{ZDA3}) \left(\frac{4}{3} \pi r^3 \right)^2 \left(\frac{3[\sin(qr) - qr \cos(qr)]}{(qr)^3} \right)^2 dr + \\
&n_{ZDA2} \int_0^\infty P(r, r_{0,ZDA2}, \sigma_{ZDA2}) \left(\frac{4}{3} \pi r^3 \right)^2 \left(\frac{3[\sin(qr) - qr \cos(qr)]}{(qr)^3} \right)^2 dr + \\
&n_{ZDA1} \int_0^\infty P(r, r_{0,ZDA1}, \sigma_{ZDA1}) \left(\frac{4}{3} \pi r^3 \right)^2 \left(\frac{3[\sin(qr) - qr \cos(qr)]}{(qr)^3} \right)^2 dr
\end{aligned} \tag{4.13}$$

where

$$P(r, r_{0,i}, \sigma_i) = \frac{1}{\sqrt{2\pi\sigma_i^2}} \exp\left(-\frac{(r - r_{0,i})^2}{2\sigma_i^2}\right) \tag{4.14}$$

$$i = \text{ZDA1, ZDA2, ZDA3} \tag{4.15}$$

$r_{0,ZDA1}$, $r_{0,ZDA2}$ and $r_{0,ZDA3}$ are the mean radii of the first ZDA aggregates, the second ZDA aggregates and the larger ZDA aggregates, respectively. It is important to note that we used a value of 1.6 μm for $r_{0,ZDA3}$, which was determined in Chapter 3 because the size of $r_{0,ZDA3}$ is beyond the accessible q range in the current SANS measurements. n_{ZDA1} , n_{ZDA2} and n_{ZDA3} are the number per unit volume of the first ZDA aggregates, second ZDA aggregates

and the larger ZDA aggregates, respectively. To describe the size distribution of the ZDA aggregates, a Gaussian distribution was used, as described in Eq. (4.13). The solid line was able to reproduce the observed $S_{ZZ}(q)$, as shown in Figure 4.3 (a), and then, we adapted this model function.

Because the HC-BR layer is supposed to adsorb onto the surface of ZDA aggregates, the scattering function of the region consisting of ZDA aggregates and the HC-BR layer ($S_{HC-BR+ZDA}(q)$) is also expected to be described with a similar hierarchical structure model as follows:

$$\begin{aligned}
S_{HC-BR+ZDA}(q) &= |F_{HC-BR+ZDA}(q)|^2 \\
&= n_{ZDA3} \int_0^\infty P(r, r_{0,HC-BR3}, \sigma_{HC-BR3}) \left(\frac{4}{3} \pi r^3 \right)^2 \left(\frac{3[\sin(qr) - qr \cos(qr)]}{(qr)^3} \right)^2 dr + \\
&n_{ZDA2} \int_0^\infty P(r, r_{0,HC-BR2}, \sigma_{HC-BR2}) \left(\frac{4}{3} \pi r^3 \right)^2 \left(\frac{3[\sin(qr) - qr \cos(qr)]}{(qr)^3} \right)^2 dr + \\
&n_{ZDA1} \int_0^\infty P(r, r_{0,HC-BR1}, \sigma_{HC-BR1}) \left(\frac{4}{3} \pi r^3 \right)^2 \left(\frac{3[\sin(qr) - qr \cos(qr)]}{(qr)^3} \right)^2 dr
\end{aligned} \tag{4.16}$$

where $r_{0,HC-BR1}$, $r_{0,HC-BR2}$ and $r_{0,HC-BR3}$ are the mean radii of the first HC-BR layer, the second HC-BR layer and the larger HC-BR layer, respectively. Figure 4.3 shows the results for the fitting analyses of the partial scattering functions. Each partial scattering function fitted well to the previously mentioned structure models, and the parameters obtained from the fitting procedures are summarized in Table 4.3. From the calculated partial scattering function $S_{zz}(q)$ corresponding to self-correlation of the ZDA aggregates, the size of the ZDA aggregates can be evaluated. The mean size of the 1st and 2nd ZDA aggregates coincided with those determined from image analyses on the TEM images within experimental error ($r_{0,ZDA1} = 1.4$ nm and $r_{0,ZDA2} = 5.0$ nm). This result indicates that the difference in the measurement condition between SANS and TEM does not affect the

resulting size information for the ZDA aggregates, which are on the nanometer scale. $\phi_{\text{HC-BR}}$ and $\phi_{\text{MT-BR}}$ are 0.89 and 0.46, respectively, implying that the swelling ratio of HC-BR was lower than that of the BR matrix. Therefore, the crosslinking density of the HC-BR layer around the ZDA aggregates must be higher than that of the BR matrix region. The physical description of HC-BR, which segregated on the surface of the ZDA aggregates, was experimentally confirmed, and successful investigation of the structure of the HC-BR layer was achieved.

Table 4.3: Characteristic parameters calculated from the fitting analysis.

$r_{0,\text{ZDA1}}$ (nm)	1.4	$r_{0,\text{HC-BR1}}$ (nm)	3.2
$r_{0,\text{ZDA2}}$ (nm)	5.0	$r_{0,\text{HC-BR2}}$ (nm)	7.9
$r_{0,\text{ZDA3}}$ (nm)	1600	$r_{0,\text{HC-BR3}}$ (nm)	1610
σ_{ZDA1} (nm)	1.1	$\sigma_{\text{HC-BR1}}$ (nm)	0.3
σ_{ZDA2} (nm)	1.7	$\sigma_{\text{HC-BR2}}$ (nm)	1.8
σ_{ZDA3} (nm)	800	$\sigma_{\text{HC-BR3}}$ (nm)	800
n_{ZDA1} (nm ⁻³)	3.8×10^{-3}	$\phi_{\text{HC-BR}}$	0.89
n_{ZDA2} (nm ⁻³)	1.1×10^{-6}	$\phi_{\text{MT-BR}}$	0.46
n_{ZDA3} (nm ⁻³)	6.5×10^{-18}	ξ_1 (nm)	2.6
ξ_2 (nm)	8.2	ξ_3 (nm)	61

The volume fraction of the BR matrix region ($\phi_{\text{MT-BR}}$) was compared to that from the degree of swelling of the sample Q (1.96). Because ZDA cannot be swollen but BR can be swollen in toluene, $\phi_{\text{MT-BR}}$ estimated from Q can be expressed as follows:

$$\begin{aligned}
\phi_{MT-BR} &= \frac{\Psi_{BR}}{\Psi_{BR} + Q - 1} \\
&= \frac{0.873}{0.873 + 1.96 - 1} = 0.48
\end{aligned}
\tag{4.17}$$

where Ψ_{BR} is the volume fraction of BR. The value of ϕ_{MT-BR} evaluated from Q is nearly equal to that obtained from the SANS measurement (i.e., 0.46), suggesting that the results from the fitting analyses are reasonable.

Based on the $r_{0,ZDA1}$ (1.4 nm) and $r_{0,HC-BR1}$ (3.2 nm) values, the mean thicknesses of the HC-BR layer around the first ZDA aggregates was estimated to be 1.8 nm, and the thickness of the HC-BR layer around the second ZDA aggregates was estimated to be 2.9 nm using the same assumption. The total volume fraction of ZDA aggregates ($\phi_{total-ZDA,fit}$) and HC-BR layers ($\phi_{total-HC-BR,fit}$) were estimated to 0.062 and 0.075, respectively. In comparison to the initial volume fraction of ZDA (0.124), $\phi_{total-ZDA,fit}$ was approximately half that value. Therefore, the model function is not suitable for the current rubber material. However, it is important to note that the rubber material was swollen by toluene for the SANS and SAXS experiments. Therefore, we must take into account the contribution of toluene for comparison to the volume fraction of ZDA. For this purpose, $\phi_{total-ZDA,fit}$ and $\phi_{total-HC-BR,fit}$ should be normalized by the degree of swelling (Q), and these normalized values ($\phi_{total-ZDA,fit}$ and $\phi_{total-HC-BR,fit}$) were determined to be 0.122 and 0.147, respectively. Taking account the possible error from the fitting procedure, $\phi_{total-ZDA,fit}$ is nearly equal to the ZDA content of the sample (0.124), suggesting that the results from the fitting analyses are reasonable.

The ζ_1 , ζ_2 and ζ_3 values, which indicate that the distance between the crosslinking and the size of the inhomogeneous crosslinked structures in the

BR matrix region, are 2.6 nm, 8.2 nm and 61 nm, respectively. We also estimated the average molecular weight between the crosslinks (M_s) from the degree of swelling of the sample ($Q = 1.96$) using the Flory-Rehner equation [9, 10]. Then, M_s was estimated to be 4.22×10^2 g/mol. The correlation length (ζ_s) of the BR network can be calculated from the following equation:

$$M_s = M_0 \left(\frac{\zeta_s}{l} \right)^{1.67} \quad (4.18)$$

where M_0 and l are the molecular weight of the monomer of BR and the statistical segment length of BR, respectively. Using $M_0 = 52$ g/mol and $l = 0.828$ nm, ζ_s was calculated to be 3.1 nm. The ζ_s value (3.1 nm) that was obtained from the degree of swelling nearly coincided with the ζ_1 value (2.6 nm) from CV-SANS analysis, suggesting that the adopted analysis model in the current study is reasonable.

In comparison to rubber material reinforced by the addition of an inorganic nanofiller, such as carbon black (CB), which is phase separated in the rubber matrix, a substantial reinforcement effect was observed for the current rubber, as described at introduction (Figure 4.6). Therefore, the additional contribution beyond the addition of a small-sized filler must be a key factor for realizing high mechanical strength in the current material. Next, we discuss the origin of the substantial increase in the mechanical strength of the current system from the viewpoint of structural analysis. The mean distance between the 1st ZDA aggregates is roughly estimated to be 1 - 5 nm in the TEM image (Figure 4.1). Based on the radius of the ZDA aggregates and the thickness of the HC-BR layer obtained from CV-SANS, the HC-BR layer may serve to connect the ZDA aggregates to each other. Alternatively, the nanometer-sized ZDA aggregates may play a major role as a cross-linker in the current system. In addition, the sum of the volume

fraction of the ZDA aggregates ($\phi_{\text{total-ZDA,fit}}$) and the HC-BR layers ($\phi_{\text{total-HC-BR,fit}}$) is only 0.269, which is lower than the fraction of closest packing. A network of HC-BR layers may be responsible for the high mechanical strength of the current rubber material. In addition, the micrometer-sized aggregates may act as stiff fillers in the current system even though the detailed structural analysis is challenging due to limitations in the accessible q range.

According to Chapter 3, accurate information was simultaneously extracted for both the structure of the HC-BR layer around ZDA aggregates. Because the thickness and volume fraction of the HC-BR layer were quantitatively revealed for the first time, additional improvement in the mechanical properties of the rubber materials must be accomplished by controlling the structure of the HC-BR region.

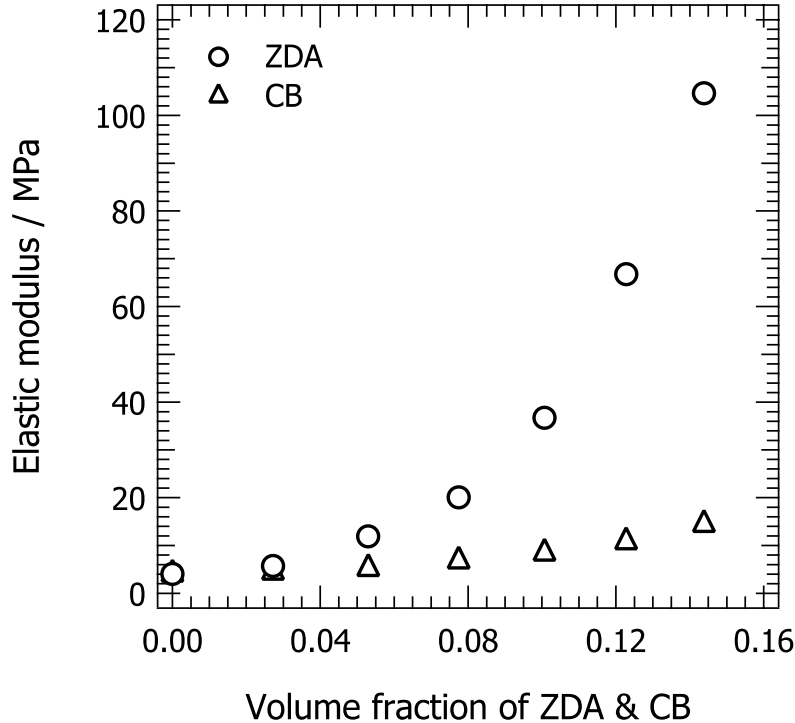


Figure 4.6: Relationship between the elastic modulus and the volume fraction of ZDA and CB.

4.4 Conclusion

We investigated the structure of butadiene rubber (BR) crosslinked with zinc diacrylate (ZDA) using the contrast variation SANS (CV-SANS) method with a focus on the structure of the high crosslink density BR (HC-BR) layer surrounding the ZDA aggregates. The partial scattering functions ($S_{PP}(q)$, $S_{ZZ}(q)$ and $S_{PZ}(q)$) were obtained using the CV-SANS method and *singular value decomposition*. The q dependence of $I_{SAXS}(q)$ was quite similar to that of $S_{ZZ}(q)$, suggesting that the results of the CV-SANS method and *singular value decomposition* are reasonable. $S_{ZZ}(q)$ fitted well to the model assuming a hierarchal structure of spheres with broad size distributions. The analyses of $S_{PP}(q)$ and $S_{PZ}(q)$ revealed the existence of a HC-BR layer surrounding the ZDA aggregates and an inhomogeneous crosslinked structure in the BR matrix region. The total volume fractions of ZDA aggregates ($\phi_{\text{total-ZDA,fit}}$) and the HC-BR layers ($\phi_{\text{total-HC-BR,fit}}$) were estimated to be 0.122 and 0.147, respectively, using the CV-SANS method. The sum of $\phi_{\text{total-ZDA,fit}}$ and $\phi_{\text{total-HC-BR,fit}}$ is only 0.269, which is lower than the fraction of closest packing, suggesting that HC-BR consists of a network, and this network structure in BR may be responsible for the high mechanical strength of the current rubber material. Using CV-SANS, our physical description of HC-BR, which segregated on the surface of the ZDA aggregates, was experimentally confirmed. Therefore, the structure of the HC-BR layer was successfully achieved for the first time.

References

- [1] S. Miyazaki, H. Endo, T. Karino, K. Haraguchi, M. Shibayama,

Macromolecules **40**, 4287 (2007).

[2] M. Takenaka, S. Nishituji, N. Amino, Y. Ishikawa, D. Yamaguchi, S. Koizumi, *Macromolecules* **42**, 308 (2009).

[3] Y. Ikeda, N. Higashitani, K. Hijikata, Y. Kukubo, Y. Morita, M. Shibayama, N. Osaka, T. Suzuki, H. Endo, S. Kohjiya, *Macromolecules* **42**, 2741 (2009).

[4] T. Suzuki, N. Osaka, H. Endo, M. Shibayama, Y. Ikeda, H. Asai, N. Higashitani, Y. Kokubo, S. Kohjiya, *Macromolecules* **43**, 1556 (2010).

[5] H. Endo, D. Schwahn, H. Cölfen, *J. Chem. Phys.* **120**, 9410 (2004).

[6] J. Tsuchida, Y. Saito, S. Sato, U. Yuki, S. Inayama, Y. Tatewaki, S. Okada, A. Shindo, C. Mikura, K. Fushihara, M. Yamada, *Polym. J.* **45**, 1007 (2013).

[7] R. L. Jones, R. W. Richards, *Polymers at Surface and Interfaces* Cambridge University Press, Cambridge, (1999).

[8] R. Inoue, M. Nakamura, K. Matsui, T. Kanaya, K. Nishida, M. Hino, *Phys. Rev. E* **88**, 032601, (2013).

[9] P. J. Flory, J. Rehner, *J. Chem. Phys.* **11**, 521 (1943).

[10] G. Kraus, *J. Appl. Polym. Sci.* **7**, 861 (1963).

Chapter 5

Quasielastic Neutron Scattering Study of Microscopic Dynamics in Polybutadiene Reinforced with an Unsaturated Carboxylate

5.1 Introduction

According to Chapters 3 and 4, in addition to the hierarchical structures of the ZDA aggregates and BR matrix, a hierarchical BR structure having a higher crosslinking density (HC-BR) than the BR matrix was observed for ZDA/BR. Concerning the dynamic structural analysis of ZDA/BR, only macroscopic rheological measurements have been performed via dynamic viscoelastic measurement. The broadening of the loss modulus $G''(\omega)$ in the frequency region corresponding to the α process was observed for ZDA/BR compared to neat BR. Since a hierarchical static structure over a wide spatial scale was revealed from the small-angle scattering methods, a corresponding *hierarchical dynamic structure* must be expected as well. Without the knowledge of this hierarchical dynamic structure, the dominant frequency region, which is responsible for mechanical strength of ZDA/BR, would be hard to identify, hindering the further promotion of mechanical strength in related rubber materials. Therefore, the hierarchical dynamic structure must be elucidated to understand the mechanism behind the high mechanical strength of ZDA/BR, in addition to its hierarchical static structure. In particular, the microscopic scale dynamics has not been adequately studied for rubber materials, including ZDA/BR, and hence, an experimental approach that can probe microscopic dynamics must be applied for ZDA/BR. One candidate technique is the quasielastic neutron scattering

(QENS) method, which can detect microscopic dynamics on a time scale ranging from pico- to microseconds at the molecular spatial level. The mechanisms of various polymer dynamics have been successfully disclosed with this method [1-9]. In addition, it should be noted that same sample conditions for industrial application, i.e., the deuteration of the sample is not required, are applicable for QENS measurements by taking advantage of the high incoherent scattering from hydrogen atoms.

In this Chapter, the dynamics of ZDA/BR was studied especially from the viewpoint of microscopic dynamics, and the origin of the high mechanical strength of ZDA/BR will be discussed based on its dynamical and static structure.

5.2 Experimental

Materials and Sample Preparation

Polybutadiene (BR; BR730, JSR Co., Ltd., Tokyo, Japan) with a weight-average molecular weight M_w of 672000 and molecular weight distribution of 2.39 was used as the matrix rubber. The microstructure of BR is cis:trans:vinyl = 97:2:1. Zinc diacrylate (ZDA; Sanceler SR, Sanshin Chemical Industry Co., Ltd., Yanai, Yamaguchi, Japan) and dicumyl peroxide (DCP; Percmyl D, Nichiyu Co., Ltd., Tokyo, Japan) were used as the crosslinker and initiator for the crosslinking reaction, respectively. The components were mixed using a 6-inch two-roll mill for 5 min, and molded into sheets about 200 μm thick at 170 °C for 20 min. As shown in Figure 4.6, the elastic modulus increases dramatically with the increase in the ZDA volume fraction. The glass transition temperatures (T_g) were constant regardless of the volume fractions of ZDA, which is shown in Figure 4.3(c). The samples used for the QENS study are listed in Table 5.1. Prior to the QENS measurements, the scattering contribution of each component was

roughly estimated. For ZDA(14), which contained the highest volume fraction of ZDA among the investigated samples, the ratio for the total scattering cross-sections of BR, ZDA, and DCP was estimated to 94.7:5.0:0.3. This suggested that the observable scattering intensity in this QENS study would be mainly dominated by the BR in ZDA/BR.

Table 5.1: Sample composition details

	ZDA(0)	ZDA(3)	ZDA(5)	ZDA(10)	ZDA(14)
Polybutadiene (vol%)	99.5	96.8	94.2	89.5	85.2
Zinc diacrylate (vol%)	0	2.7	5.3	10.1	14.4
Dicumyl peroxide (vol%)	0.5	0.5	0.5	0.4	0.4

Measurements

QENS measurements were carried out with an inverted geometry time-of-flight spectrometer (BL02 DNA) [10] installed at J-PARC, Tokai, Japan. The energy resolution δE in the present study was 3.5 μeV . The magnitude of the scattering vector Q ($Q = 4\pi\sin\theta/\lambda_f$, where 2θ and $\lambda_f = 6.26 \text{ \AA}$ are the scattering angle and the wavelength of the analyzed neutron, respectively) ranged from 0.12 to 1.78 \AA^{-1} . To cover the T_g of the present ZDA/BR, the temperature was varied from 10 to 330 K.

5.3 Results and Discussion

Figure 5.1(a,b) shows the dynamic scattering laws $S(Q, \omega)$ at $Q = 1.48 \text{ \AA}^{-1}$ for ZDA(0) and ZDA(14), respectively, at several temperatures. In the graphs, $S(Q, \omega)$ is broadened with increasing temperature for both samples.

Broader $S(Q, \omega)$ spectra are observed for ZDA(0) than ZDA(14) near room temperature, although the resolution functions, which correspond to $S(Q, \omega)$ spectra at 10 K, from ZDA(0) and ZDA(14) coincide nicely. This implies that ZDA affects the dynamics of BR at this energy resolution.

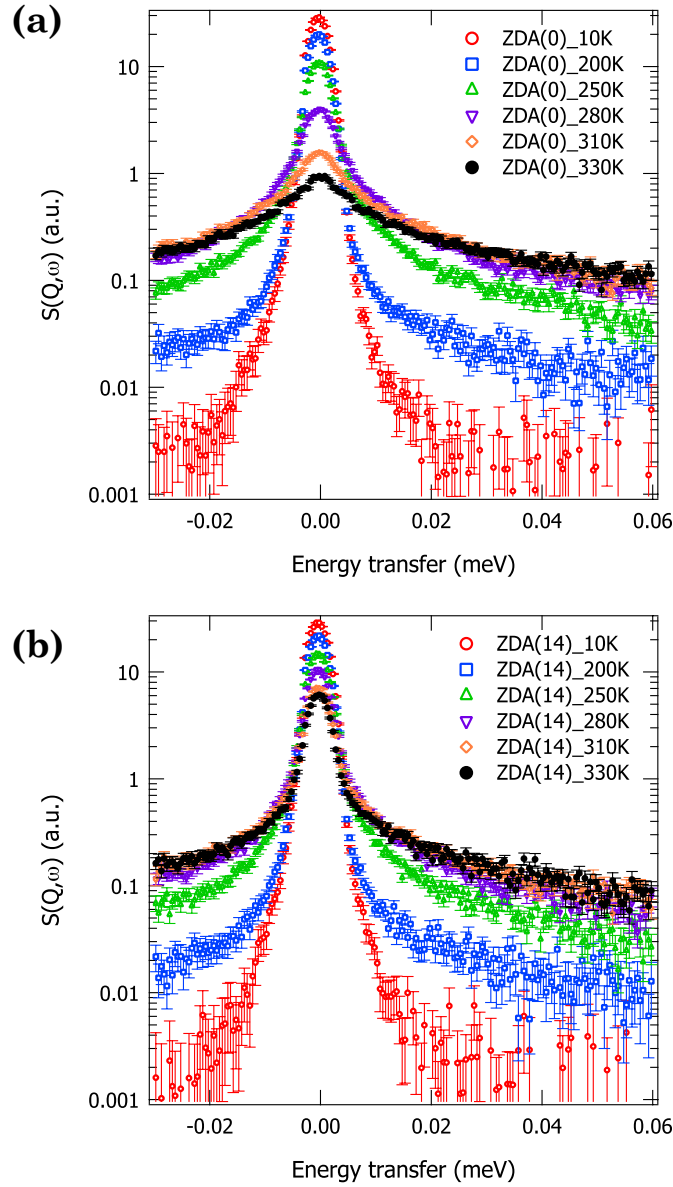


Figure 5.1: Dynamic scattering laws $S(Q, \omega)$ for (a) ZDA(0) and (b) ZDA(14) at various temperatures, obtained by summing the spectra from $Q = 1.38$ to 1.58 \AA^{-1} . The average value of Q is 1.48 \AA^{-1} .

To investigate the effect of ZDA on the observable dynamics in more detail, we evaluated the mean-square displacement ($\langle u^2 \rangle$) from the Q^2 dependence of the elastic scattering intensity ($I_{el}(Q)$), assuming the Gaussian approximation shown by Eq. (5.1).

$$\frac{I_{el}(Q)}{I_{el}(Q)_{10K}} = \exp[-\langle u^2 \rangle Q^2] \quad (5.1)$$

$I_{el}(Q)_{10K}$, which corresponds to the structure factor of a sample, is the elastic scattering intensity at 10 K. When the structure factor of a sample does not depend on temperature, dividing $I_{el}(Q)$ by $I_{el}(Q)_{10K}$ means decreasing the effect of coherent scattering from a sample. Figure 5.2(a) shows the temperature dependence of $\langle u^2 \rangle$ for ZDA/BR having different volume fractions of ZDA. In all samples, $\langle u^2 \rangle$ increases linearly with temperature, until reaching ~ 100 K. With further temperature increases, changes in the slope of $\langle u^2 \rangle$ are observed, indicating the onset of anharmonic motions. The first change in the slope of $\langle u^2 \rangle$ is observed at ~ 100 K. The onset of a localized, so-called “fast process” was reported at ~ 100 K for neat BR [11]; hence, the slope change near 100 K corresponds to the onset of the fast process. This fast-process onset temperature seems to be constant regardless of the volume fraction of ZDA. Furthermore, $\langle u^2 \rangle$ at 140 K is nearly constant regardless of the volume fraction of ZDA. This suggests that ZDA has no significant effect on the local dynamics of ZDA/BR below 140 K.

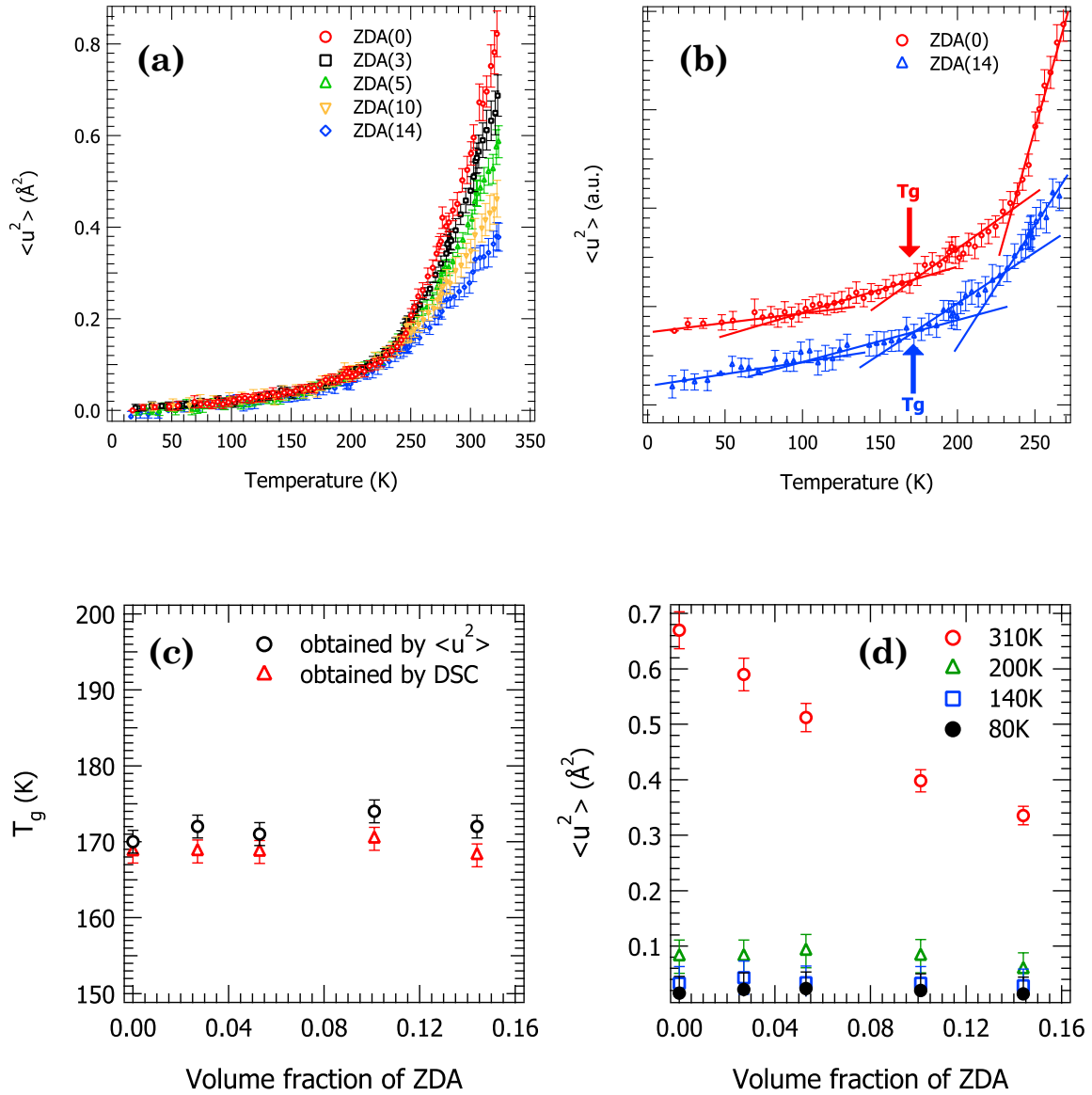


Figure 5.2: (a) The temperature dependence of $\langle u^2 \rangle$ obtained by eq. (5.1). (b) Expansion plots showing the temperature dependence of $\langle u^2 \rangle$ in ZDA(0) and ZDA(14). (c) The volume fraction of ZDA dependence of T_g obtained by $\langle u^2 \rangle$ and DSC. (d) The volume fraction of ZDA dependence of $\langle u^2 \rangle$.

The second change in the slope of $\langle u^2 \rangle$ is observed at ~ 170 K. This temperature is nicely coincident with the T_g values determined by differential scanning calorimetry (DSC), suggesting that this temperature can be regarded as the T_g from the QENS measurements. The results also confirm that the T_g values determined from both DSC and QENS are constant regardless of the ZDA volume fraction (Figure 5.2(c)). The third inflection temperature is observed at ~ 230 K; above this temperature, dramatic increases in the $\langle u^2 \rangle$ occur. To understand the physical origin for the dramatic increase in $\langle u^2 \rangle$ at temperatures above 230 K, we again focused on $S(Q, \omega)$, as shown in Figure 5.1. Above 250 K, a clear broadening of the central component of $S(Q, \omega)$ can be observed for both ZDA(0) and ZDA(14). Such broadening of the dynamic scattering laws indicates the detection of a relaxation process at the present energy resolution. Based on a previous QENS study of BR [12], it is supposed that the broadening of $S(Q, \omega)$ above 250 K must reflect the detection of the α process. We will discuss this point in the section describing the curve fittings to $S(Q, \omega)$.

The value of $\langle u^2 \rangle$ decreased clearly with the increasing volume fraction of ZDA, especially near room temperature, as shown in Figure 5.2 (d). To reveal the physical origin for the decrease of $\langle u^2 \rangle$ with the increasing volume fraction of ZDA above room temperature, we examined the $S(Q, \omega)$ near room temperature. Figure 5.3 shows the dynamic scattering laws $S(Q, \omega)$ normalized by the peak intensity of the elastic scattering from different ZDA volume fractions at 310 K. In line with the decrease in $\langle u^2 \rangle$ with the increase in ZDA volume fraction, a narrowing of the $S(Q, \omega)$ is observed. To extract the parameters describing dynamical information from the $S(Q, \omega)$, we fit the curves of the observed $S(Q, \omega)$ at different ZDA volume fractions with an appropriate model function. Richter et al. reported that the intermediate scattering function corresponding to the α process of neat BR was well fitted by the Kohlrausch-Williams-Watts (KWW)

equation [13]. Hence, we adopted the KWW function to describe the observed $S(Q, \omega)$, and the following model function was proposed.

$$S(Q, \omega) = A \left((1 - EISF) \mathcal{F} \left\{ \exp \left[- (t/\tau)^\beta \right] \right\} + EISF \delta(\omega) \right) \otimes R(Q, \omega) \quad (5.2)$$

where A , $EISF$, τ , and β are the amplitude of the relaxation function, the elastic incoherent structure factor, the relaxation time, and the distribution of the relaxation function, respectively. It should be noted that the KWW function is utilized in the time domain, necessitating that we adopt the Fourier-transformed KWW function ($\mathcal{F}(\text{KWW})$) in the frequency region. $R(Q, \omega)$ indicates the instrumental resolution function. Figure 5.4(a,b) shows the results of the fits to $S(Q, \omega)$ for ZDA(0) and ZDA(14) with Eq. (5.2) at $Q = 1.48 \text{ \AA}^{-1}$ and 310 K, respectively. The $S(Q, \omega)$ from both samples are fitted fairly well by Eq. (5.2), confirming the appropriate model function selection.

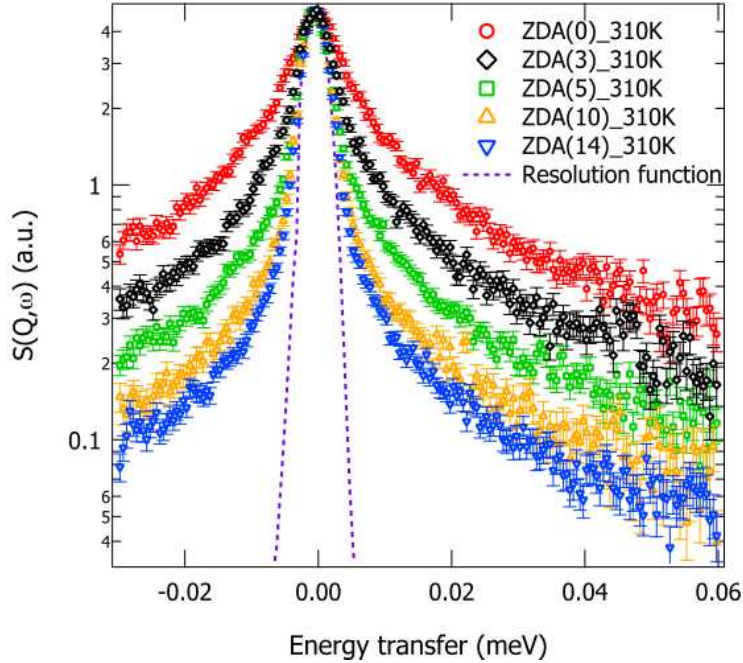


Figure 5.3: Dynamic scattering laws $S(Q, \omega)$ normalized at the peak top at 310 K. The dashed line is the instrumental resolution function.

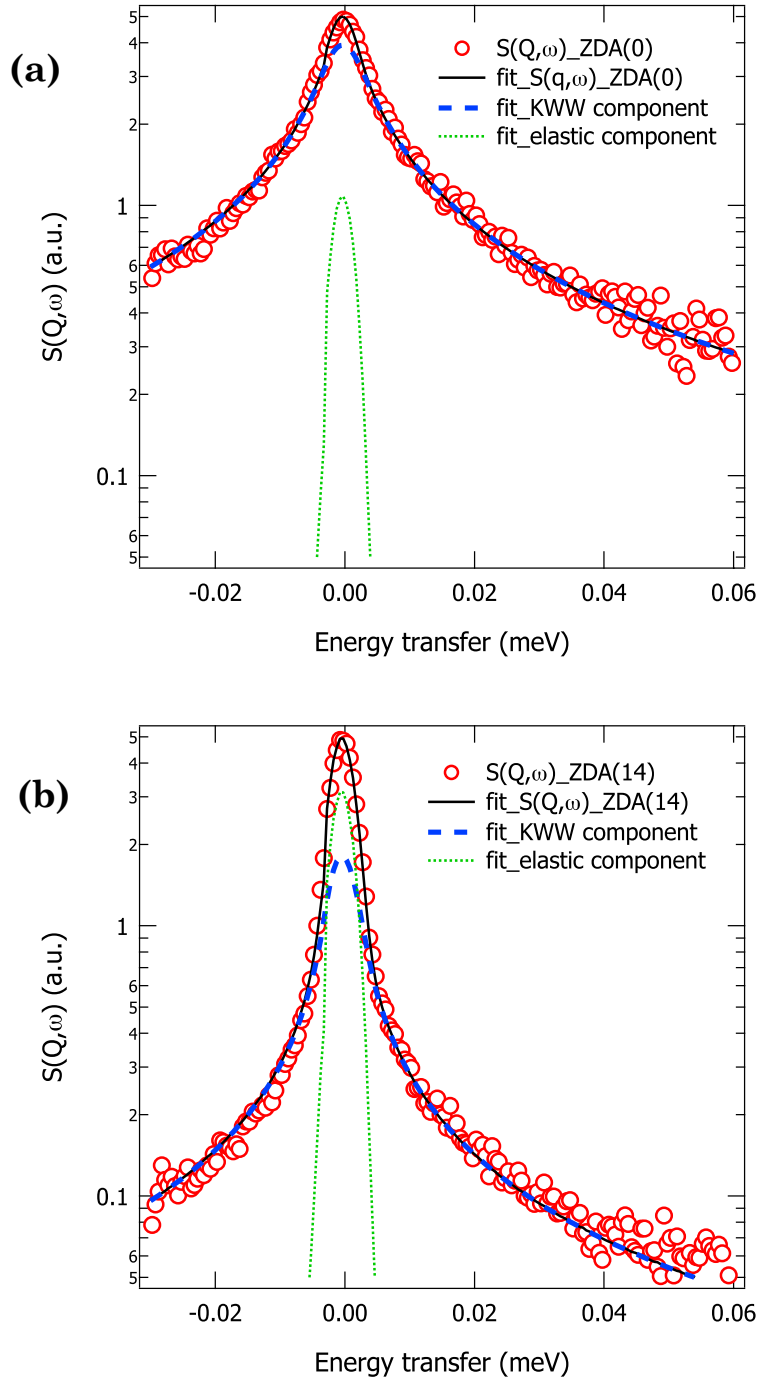


Figure 5.4: The fitting results of $S(Q, \omega)$ for (a) ZDA(0) and (b) ZDA(14) using Eq. (5.2) for $Q = 1.48 \text{ \AA}^{-1}$ at 310 K. Solid lines are the results of fittings with Eq. (5.2). Thick and thin dashed lines are the fitting results of the KWW and elastic components, respectively, in Eq. (5.2).

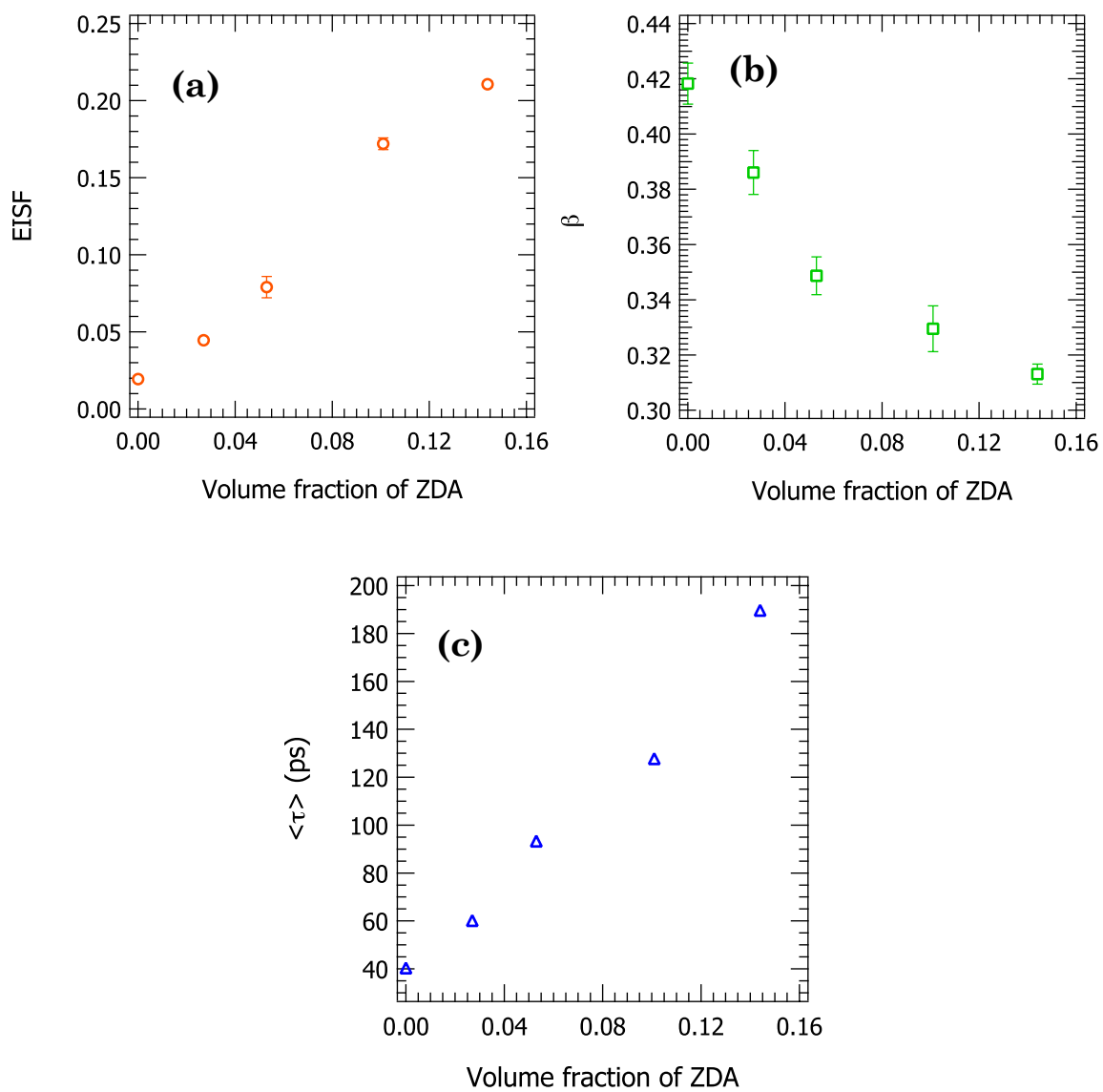


Figure 5.5: Volume fraction of ZDA dependence of (a) $EISF$, (b) β , and (c) $\langle \tau \rangle$ in the range $Q = 1.48 \text{ \AA}^{-1}$ at 310 K.

The dependence values of (a) the *EISF*, (b) β , and (c) mean relaxation time ($\langle\tau\rangle$) at 310 K on the volume fraction of ZDA are shown in Figure 5.5. $\langle\tau\rangle$ is given by the following equation [14]:

$$\langle\tau\rangle = \left(\frac{\tau}{\beta}\right) \Gamma\left(\frac{1}{\beta}\right) \quad (5.3)$$

where Γ is a Γ -function. Summarizing the obtained parameters from the curve fittings, the increase in the *EISF*, decrease of β , and increase of $\langle\tau\rangle$ with increases in the ZDA volume fraction were evaluated. Namely, increases in the immobile component, distribution time, and mean relaxation time were found with increases in the ZDA volume fraction.

To construct a plausible physical picture that could explain the evaluated parameters without inconsistency, we referred to the structural information revealed in Chapters 3 and 4. From small-angle scattering studies, the coexistence of BR regions having low and high crosslinking densities was revealed, and through DSC, a second T_g was also observed at 353 K. It should be noted that the highest temperature in the present QENS measurements was lower than this second T_g , which would suggest that the first T_g corresponds to the that of the low crosslinking density region and the second T_g corresponds to the highly crosslinked domain. Based on this assumption, we considered that the mobile component originates from the low crosslinking density region and the immobile component (*EISF*) originates mainly from the high crosslinking density one (HC-BR), which would still be in a glassy state within the present temperature range. Since an increase in the *EISF* was observed with increasing ZDA volume fraction, a physical picture that assumes the simple coexistence of mobile and immobile regions in the ZDA/BR is seemingly applicable for the observed dynamics. If such a physical picture is strictly valid for the present ZDA/BR, the evaluated relaxation times or distributions of relaxation times must be

constant, regardless of the volume fraction of ZDA. However, a slight increase in the relaxation time or broadening of the relaxation time distribution was found with increases in the volume fraction of ZDA. That is to say, another contributing factor beyond the mobile contribution must be present in the ZDA/BR.

It is known that a polymer near a substrate or impenetrable boundary exhibits anomalous physical properties [15]. Hence, we expected that the dynamics of BR near the HC-BR regions would be strongly perturbed by the HC-BR region in the glassy state, resulting in slower relaxation. With increases in the volume fraction of ZDA, the contributions from such interfacial regions near HC-BR should also increase. Thus, due to the gradient of dynamics mediated by the ZDA aggregates, more heterogeneous and slower dynamics are observed for ZDA/BR than neat BR.

Finally, we compared the present results to previous findings from other rubber systems to determine the origin of the high mechanical strength of ZDA/BR. Roh et al.[1] studied the dynamics of the BR reinforced with carbon black (CB) (CB/BR) and BR via neutron back-scattering, and also observed both the slowing and broadening of the α process for CB/BR compared to neat BR. Qualitatively, both our group and Roh's observed similar trends, although a drastic difference between the moduli was seen for the two systems (*cf.* Figure 5.1). In both cases, the formation of network-like structures is believed to be responsible for realizing the improved mechanical strength which is necessary for practical application. Accordingly, it is supposed that the difference in the mechanism of interaction between the BR and the reinforcement agents must be related to the difference in mechanical strength. In the CB/BR system, it was considered that a network-like structure of physically adsorbed BR on the surface of CB was related to its mechanical strength [16]. In contrast, the formation of covalent bonds between the C=C double bonds in the ZDA

aggregates and the BR must effectively contribute to their strong interactions. In addition, with the increasing volume fraction of ZDA, such tightly constrained BR regions must also grow, as described above. Then, the covalently constrained BR on the surface of the ZDA (HC-BR) in itself would be expected to act as a kind of cross-linker in ZDA/BR, leading to the formation of a tougher network-like structure than in CB/BR, in which the physically absorbed BR alone acts as a cross-linker. Thus, a more rigid network-like structure is developed in ZDA/BR than in CB/BR, imparting a higher mechanical strength for the former at a given volume fraction of reinforcement agent.

5.4 Conclusion

We studied the dynamics of polybutadiene rubber (BR) reinforced with zinc diacrylate (ZDA) (ZDA/BR) by the quasielastic neutron scattering (QENS) technique to reveal the origin of its high elastic modulus from the viewpoint of microscopic dynamics. The mean square displacements ($\langle u^2 \rangle$) of ZDA/BR having different ZDA volume fractions were evaluated. At temperatures below 230 K, no significant ZDA volume fraction dependence was observed for $\langle u^2 \rangle$; on the other hand, a clear reduction of $\langle u^2 \rangle$ with an increasing volume fraction of ZDA was seen above 230 K. To understand the origin of the decrease in $\langle u^2 \rangle$ with the increasing volume fraction of ZDA, dynamic scattering laws were analyzed with a model function, assuming the addition of an elastic component and a Fourier-transformed KWW function in the frequency region. With this model function, the observed dynamic scattering laws from different ZDA volume fractions were nicely fitted. From the results of the curve fittings, the increase in the elastic incoherent structure factor (*EISF*), increase of the mean relaxation time ($\langle \tau \rangle$), and broadening of the relaxation time distribution (β) were evaluated as

functions of the increase of the volume fraction of ZDA. Based on a previously reported static structure, the idea of heterogeneous dynamics that assumes the existence of immobile, mobile, and interfacial constrained mobile regions was proposed as a candidate for understanding the observed dynamics without inconsistency.

By comparing the reported results from CB/BR to those from ZDA/BR in this study, it was postulated that the difference in the interaction between BR and the reinforcement agents must be related to the huge difference in mechanical strength. In the case of ZDA/BR, the existence of chemical bonds between the BR and ZDA contributed to the effective, strong interaction between the BR and the reinforcement agents, compared to CB/BR, in which physical adsorption played the main role. Such covalently constrained BR on the surface of ZDA is expected to function as a kind of cross-linker in ZDA/BR, leading to the formation of a tougher network-like structure than in CB/BR. As a result, a higher mechanical strength was realized for ZDA/BR compared to CB/BR at a given volume fraction of reinforcement agents.

References

- [1] J. H. Roh, M. Tyagi, T. E. Hogan, C. M. Roland, *Macromolecules* **46**, 6667 (2013).
- [2] J. H. Roh, M. Tyagi, T. E. Hogan, C. M. Roland, *J. Chem. Phys.* **139**, 134905 (2013).
- [3] V. Arrighi, J. S. Higgins, A. N. Burgess, G. Floudas, *Polymer* **39**, 6369 (1998).
- [4] S. Gagliardi, V. Arrighi, R. Ferguson, M.T.F. Telling, *Physica B* **301**, 110 (2001).

- [5] C. Karlsson, A. S. Best, J. Swenson, W. S. Howells, L. Borjesson, *J. Chem. Phys.* **118**, 4206 (2003).
- [6] K. Chrissopoulou, S. H. Anastasiadis, E. P. Giannelis, B. Frick, *J. Chem. Phys.* **127**, 144910 (2007).
- [7] S. Fotiadou, K. Chrissopoulou, B. Frick, S. H. Anastasiadis, *J. Polym. Sci. Pol. Phys.* **48**, 1658 (2010).
- [8] P. Akcora, S. K. Kumar, V. G. Sakai, Y. Li, B. C. Benicewicz, L. S. Schadler, *Macromolecules* **43**, 8275 (2010).
- [9] K. Sinha, W. Wang, K. I. Winey, J. K. Maranas, *Macromolecules* **45**, 4354 (2012).
- [10] K. Shibata, N. Takahashi, Y. Kawakita, M. Matsuura, T. Yamada, T. Tominaga, W. Kambara, M. Kobayashi, Y. Inamura, T. Nakatani, K. Nakajima, M. Arai, *JPS Conference Proceedings* **8**, 036022 (2015).
- [11] T. Kanaya, K. Kaji, *Adv. Polym. Sci.* **154**, 87 (2001).
- [12] T. Kanaya, T. Tsukushi, K. Kaji, J. Bartos, J. Kristiak, *Phys. Rev. E.* **60**, 1906 (1999).
- [13] D. Richter, M. Monkenbusch, A. Arbe, J. Colmenero, *J. Non-Cryst. Solids* **287**, 286 (2001).
- [14] T. Kanaya, R. Inoue, M. Saito, M. Seto, Y. Yoda, *J. Chem. Phys.* **140**, 144906 (2014).
- [15] J. Martin, M. Krutyeva, M. Monkenbusch, A. Arbe, J. Allgaier, A. Radulescu, P. Falus, J. Maiz, C. Mijangos, J. Colmenero, D. Richter, *Phys. Rev. Lett.* **104**, 197801 (2010).
- [16] Y. Fukahori, *Rubber Chem. Technol.* **80**, 701 (2007).

Chapter 6

Dynamical Study of Polybutadiene Reinforced with an Unsaturated Carboxylate by Muon Spin Relaxation

6.1 Introduction

In Chapter 5, it was found that the dynamics of BR was affected by addition of ZDA at the time scale of picosecond. In order to understand the essence of the reinforcement effect of ZDA, it is important to investigate the dynamics of ZDA/BR in various time scales. Usually time and spatial ranges covered by a single experimental method is limited and the contrasts in experimental methods are very different method by method. This is why many experimental techniques were employed to study the heterogeneous dynamics in polymers. In Chapter 6 we applied muon spin relaxation (μ SR) technique to investigate the heterogeneous dynamics in crosslinked BR with and without ZDA to find characteristic aspects in the heterogeneous dynamics.

Muon has been used in various research fields, including various polymer dynamics studies by μ SR [1-7]. Pioneering work on the dynamics of neat BR was performed by Pratt et al. using μ SR [4], where they used muon radical state as a probe of the dynamical properties of the polymer. They reported that dynamical changes in the μ SR signals were observed at around the glass-rubber transition, suggesting μ SR was useful to investigate the dynamics of the polymer. However, dynamics of polymer reinforced with filler, especially dynamics of polymers reinforced with metal diacrylate, has not been investigated by μ SR.

In this Chapter, therefore, we aimed at revealing the reinforcement

effect of ZDA on the dynamics of BR in the time scale of microsecond using μ SR measurement.

6.2 Experimental

Materials and Sample Preparation

The details of materials used in the present study are summarized in Table 6.1. Polybutadiene (BR; BR730, JSR Co., Ltd., Tokyo, Japan) with a weight-average molecular weight M_w of 672000 and molecular weight distribution of 2.39 was used as the matrix rubber. The microstructure of BR is cis:trans:vinyl = 97:2:1. Zinc diacrylate (ZDA; Sanceler SR, Sanshin Chemical Industry Co., Ltd., Yanai, Yamaguchi, Japan) and dicumyl peroxide (DCP; Percmyl D, Nichiyu Co., Ltd., Tokyo, Japan) were used as the crosslinker and initiator for the crosslinking reaction, respectively. The components were mixed using a 6-inch two-roll mill for 5 min, and molded into sheets about 1 mm thick at 170 °C for 20 min. The glass transition temperature (T_g) of ZDA(0) and ZDA(14) obtained by differential scanning calorimetry (DSC) are 168.6 K and 168.1 K, respectively. The elastic modulus at 293 K and 10 Hz of ZDA(0) and ZDA(14) obtained by dynamic viscoelasticity measurement are 4.0 MPa and 104.6 MPa, respectively.

Table 6.1: Details about the components of the samples used in the present study.

	ZDA(0)	ZDA(14)
Polybutadiene (vol%)	99.5	85.2
Zinc diacrylate (vol%)	0	14.4
Dicumyl peroxide (vol%)	0.5	0.4

Measurements

The Longitudinal field (LF) μ SR experiment was performed using a beamline D1 instrument installed at Material and Life Science Experimental Facilities (MLF) in J-PARC in the temperature range between 30 and 270 K. External magnetic field was 100 G. Each sample was set onto the sample holder. In the LF- μ SR experiment the external magnetic field was applied parallel to the direction of the muon spin. In the experiments positrons were detected by counters that were positioned in front of and behind the sample with respect to the initial muon momentum direction. The decay of asymmetry ($A(t)$) of the polarized muon was evaluated through Eq. (6.1), where $F(t)$ and $B(t)$ represent the number of positron counts in the forward and backward detectors, respectively, as a function of time [1].

$$A(t) = \frac{F(t) - \alpha B(t)}{F(t) + \alpha B(t)} \quad (6.1)$$

where α is a correction factor which takes into account the relative efficiencies of the detectors. The obtained raw asymmetry data were corrected for the instrumental constant and for the backgrounds from the sample holder. In the study it is important to specify where muon is located in the sample to interpret the experimental results. Muon often forms muonium atom in various materials, which is a confined state of positive muon (μ^+) and electron (e^-) and regarded as a light hydrogen atom [8-11]. Such muonium can react with unsaturated bonds such as C=C in the sample. Many C=C bonds exist in the ZDA/BR system and the C=C bonds are mainly from BR because C=C bond in ZDA must be exhausted to form the crosslinks during the sample preparation [12]. It is therefore considered that muons are mainly located in BR as muonium atoms and spin relaxation of muonium atoms are dominated by the fluctuations of internal magnetic field of BR.

6.3 Results and Discussion

The decay curves of asymmetry $A(t)$ in the LF- μ SR experiments are shown in Figure. 6.1 for ZDA(0) and ZDA(14), which depend on the temperature, and are clearly different between ZDA(0) and ZDA(14). In order to understand the results quantitatively these decay curves were fitted to KWW function [Eq. (6.2)].

$$A(t) = A \exp\left[-(t/\tau)^\beta\right] + B \quad (6.2)$$

where A , τ , β and B are the amplitude of the relaxation function, relaxation time, the distribution of the relaxation time and the so-called “diamagnetic” fraction, respectively. The samples used in the experiments seem very heterogeneous due to the crosslinks as well as the filler ZDA, and hence the wide distribution of relaxation times is expected. Then we employed the KWW function to evaluate the distribution of the relaxation time. An average relaxation time $\langle \tau \rangle$ in the KWW function can be calculated through Eq. (6.3).

$$\langle \tau \rangle = \frac{\tau}{\beta} \Gamma\left(\frac{1}{\beta}\right), \quad (6.3)$$

where Γ is a gamma function. The average relaxation time corresponds to the integrated area of the KWW function. As seen in Figure 6.1 the agreement between the observed decay curves and the fitted KWW function look very good, suggesting the KWW function can describe the decay behavior of the asymmetry $A(t)$ well.

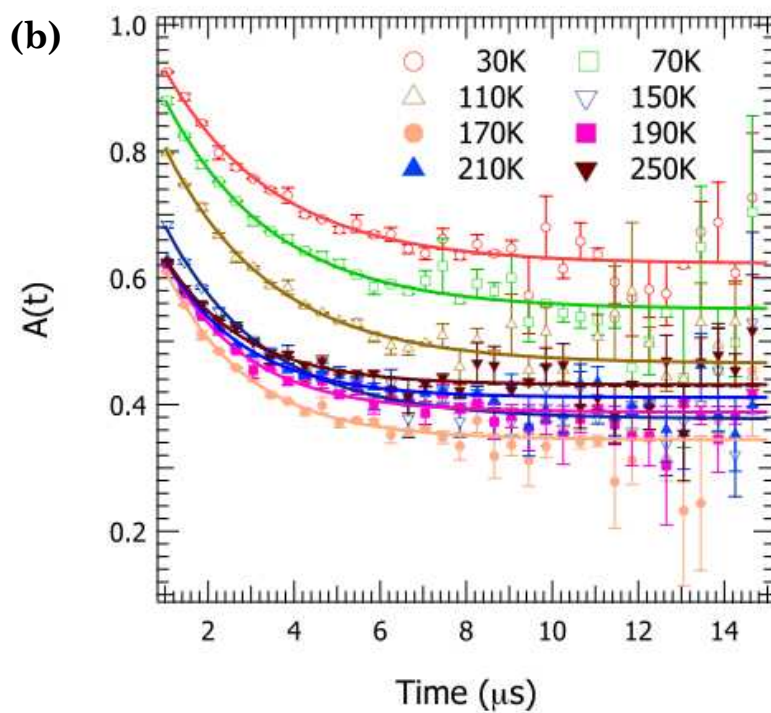
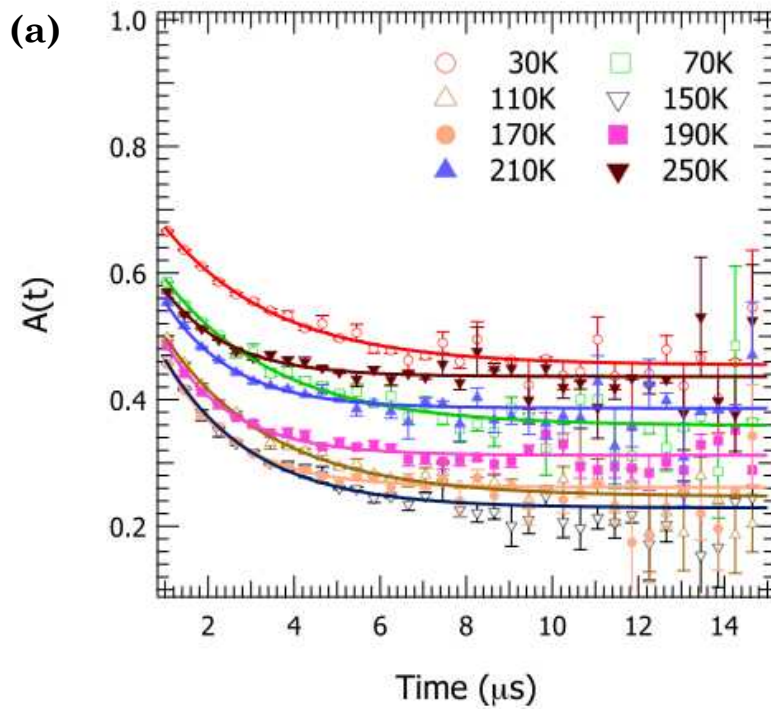


Figure 6.1: Decay of asymmetry $A(t)$ of (a) ZDA(0) and (b) ZDA(14) for various temperatures. The solid curves in the figures are the results of KWW fits.

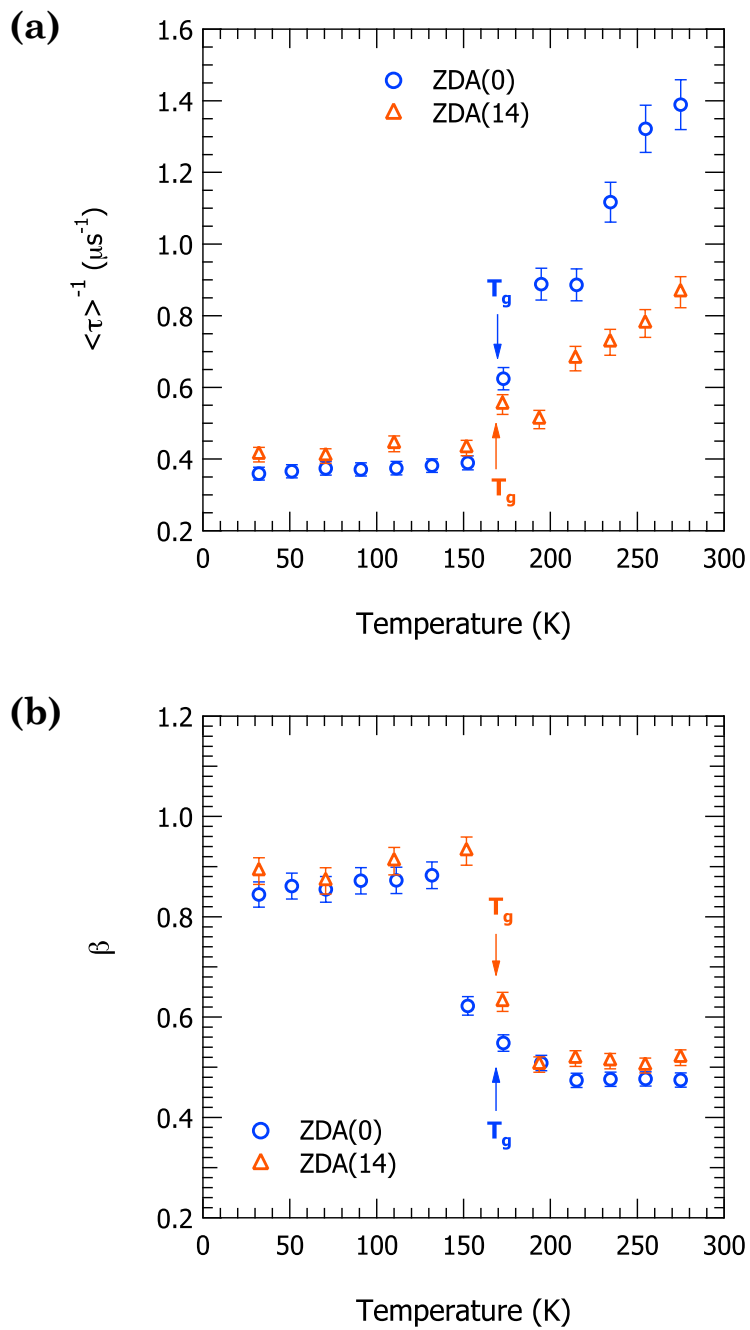


Figure 6.2: Temperature dependence of (a) relaxation rate ($\langle \tau \rangle^{-1}$) (b) β of ZDA(0) and ZDA(14).

The temperature dependence of the relaxation rate ($\langle\tau\rangle^{-1}$) and β obtained by fitting is shown as a function of temperature in Figure 6.2 (a) and (b), respectively. The relaxation rates are almost temperature independent below T_g and the values are almost identical between the two samples. Below T_g the motions of BR is almost suppressed and then the $A(t)$ suggests the static fluctuations of magnetic field due to the heterogeneous structure. The almost identical value of the relaxation rate ($\langle\tau\rangle^{-1}$) implies the similar heterogeneous fluctuations between the two samples. On the other hand, the relaxation rates begin to increase monotonically with temperature above T_g for both of the samples. Similar temperature behavior of the relaxation rate has been reported by Pratt et al. for neat BR [4], suggesting that our measurements were performed well and the dynamics of our crosslinked BR qualitatively identical to the neat BR. The relaxation rate of ZDA(0) is higher than that of ZDA(14) above T_g . From the sample preparation procedure, it is clear that the ZDA(14) has more crosslinks than ZDA(0), implying the motion of BR in ZDA(14) is restricted compared with ZDA(0). The faster relaxation rate in ZDA(0) suggests the dynamic fluctuations of magnetic field in BR is faster in ZDA(0) than ZDA(14) due to the faster molecular motions in ZDA(0). In addition, as seen in the QENS studies in Chapter 5, the dynamics of ZDA(14) is constrained more than ZDA(0). Therefore it is confirmed that the faster spin relaxation rate of ZDA(0) than ZDA(14) indicates the faster motional relaxation rate of ZDA(0) than ZDA(14) due to the confinement by the crosslinks. It is further expected that this difference of the spin relaxation rate is related to the fact that the elastic modulus of ZDA(14) is larger than that of ZDA(0).

Next we focus on the parameter β , which represents the width of the distribution of the spin relaxation rate. As seen in Figure 6.2, β does not depend on the temperature below T_g , showing the relaxation rate

distribution is independent of temperature for both of the samples. On the other hand, it abruptly decreases at round T_g , and becomes temperature independent again above 200 K. This result is opposite to the reported result of neat BR by Pratt et al. [4], in which β increases with temperature above T_g and the value of β (0.5 – 0.6) is larger than that in our ZDA/BR system (0.45 – 0.5). In the case of neat BR, it is considered that β increase with temperature because the magnetic field becomes homogenized due to the mobility of BR. On the other hand, in our crosslinked BR system, there exist low and high density regions of crosslinks as shown in Chapters 3 and 4. At low temperatures below T_g , the mobility of BR in both the low and high crosslink density regions are not so different because BR is almost frozen. As temperature increases, the mobility of BR increases, especially above T_g . In this situation, the mobility in the low crosslink density region is probably not so different from the neat BR, while the mobility in the high crosslink density region must be lower than that of the neat BR, resulting in a wide distribution of motional relaxation time or the small value of β . The difference of β between ZDA(0) and ZDA(14) is not very large, suggesting that the distribution width of relaxation rate is almost identical. Before performing the experiment we expected smaller value of β for ZDA(0) than ZDA(14) because the magnetic fluctuations in BR in ZDA(14) is more heterogeneous due to the ZDA aggregates, but the observed values of β are almost identical. At the moment it is impossible to find any appropriate explanations for that. In Chapter 5, we have evaluated the motional relaxation rate and its distribution width in terms of KWW β for ZDA(0) and ZDA(14) in the QENS experiments. Physical meaning of spin relaxation rate is not identical with the motional relaxation rate, but β s of them reflect the dynamic heterogeneity of the system. The β value of the motional relaxation rate decreases with increasing the fraction of ZDA (see Figure 5.5(b)). This result agrees with our expectation. But the β value for the

asymmetry relaxation rate was independent of ZDA fraction (Figure 6. 2 (b)). We have no final explanations for the discrepancy as mentioned above. One possible explanation is that the dynamic heterogeneity in picosecond time scale probed by QENS is affected by ZDA but not affected in the microsecond time scale probed by μ SR.

6.4 Conclusion

We studied the dynamics of polybutadiene rubber (BR) reinforced with zinc diacrylate (ZDA) (ZDA/BR) by the muon spin relaxation (μ SR) technique in a microsecond time scale. The obtained relaxation rates ($\langle \tau \rangle^{-1}$) is almost constant below T_g while it rises monotonically with increasing temperature above glass transition temperature T_g and the relaxation rate of ZDA(0) is higher than that of ZDA(14) above T_g . It is clear that the ZDA(14) has more crosslinks than ZDA(0) and the motion of BR in ZDA(14) is restricted compared with ZDA(0). Therefore, the faster relaxation rate in ZDA(0) has been assigned to the faster molecular motions in BR in ZDA(0). It was also found that the β value, which represents the width of the spin relaxation rate, abruptly decreased at around T_g . This is opposite to the reported result of neat BR, in which β increases with temperature above T_g . This discrepancy was assigned to the coexistence of the low and high crosslinks density regions in ZDA/BR. The value of β was almost independent of the fraction ZDA both above and below T_g . This result suggest that the heterogeneity of the magnetic field fluctuations in BR is almost identical for ZDA(0) and ZDA(14). It is hard to understand the result at the moment. As shown by the QENS study in Chapter 5, the dynamic heterogeneity increases with the fraction of ZDA in the picosecond region, but the present result suggests that the heterogeneity in BR is almost independent of ZDA fraction in microsecond time scale.

References

- [1] N. J. Clayden, U. A. Jayasooriya, S. P. Cottrell, *Phys. Chem. Chem. Phys.* **1**, 4379 (1999).
- [2] F. L. Pratt, S. J. Blundell, P. A. Pattenden, W. Hayes, K. H. Chow, A. P. Monkman, T. Ishiguro, K. Ishida, K. Nagamine, *Hyperfine Interact.* **106**, 33 (1997).
- [3] F. L. Pratt, S. J. Blundell, W. Hayes, K. Nagamine, K. Ishida, A. P. Monkman, *Phys. Rev. Lett.* **79**, 2855 (1997).
- [4] F. L. Pratt, S. J. Blundell, Th. Jestadt, B. W. Lovett, A. Husmann, I. M. Marshall, W. Hayes, A. Monkman, I. Watanabe, K. Nagamine, R. E. Martin, A. B. Holmes, *Physica B* **289**, 625 (2000).
- [5] S. J. Blundell, F. L. Pratt, I. M. Marshall, C. A. Steer, W. Hayes, A. Husmann, C. Fischmeister, R. E. Martin, A. B. Holmes, *J. Phys. Condens. Matter* **14**, 9987 (2002).
- [6] Risdiana, Fitrilawati, R. Hidayat, A. A. Nugroho, R. E. Siregar, M. O. Tjia, I. Watanabe, *Physica B* **405**, 5381 (2010).
- [7] Risdiana, B. Adiperdana, L. Safriani, A. Bahtiar, Fitrilawati, R. E. Siregar, R. Hidayat, A. A. Nugroho, M. O. Tjia, I. Watanabe, *Physics Procedia* **30**, 97 (2012).
- [8] A. Amato, *Rev. Mod. Phys.* **69**, 1119 (1997).
- [9] J. R. Christopher, *Annu. Rep. Prog. Chem. Sect. C* **97**, 315 (2001).
- [10] A. E. Pfifer, T. Bowen, K. R. Kendall, *Nucl. Instrum. Methods* **135**, 39 (1976).
- [11] E. Roduner, *Chem. Soc. Rev.* **22**, 337 (1993).
- [12] J. Tsuchida, Y. Saito, S. Sato, U. Yuki, S. Inayama, Y. Tatewaki, S. Okada, A. Shindo, C. Mikura, K. Fushihara, M. Yamada, *Polym. J.* **45**, 1007 (2013).

Chapter 7

Observation of Deformation Behavior of The Rubber Depending on Asperity of Road by Four-Dimensional X-ray Computed Tomography

7.1 Introduction

In Chapter 3 to 6, we studied the static and dynamic structure of the rubber below micrometer spatial scale from scientific viewpoint. In this Chapter we focused on the rubber used as an industrial product. We consider that this study about dynamic structure plays a role as a bridge between the scientific research and the industrial product.

Environmental protection is a global concern, especially in the automobile industry. It is important to reduce the fuel consumption due to the tire of an automobile because the rolling resistance of the tire amounts to approximately 20% of the entire fuel consumption of the automobile. Reducing the rolling resistance of the tire, although necessary to reduce the fuel consumption of an automobile, decreases the ability of the tire to grip, which is necessary to stop the automobile safely. Therefore, a trade-off between the rolling resistance and grip of the tire is desired.

To understand the gripping property of a tire made of rubber, the deformation inside the tire and the tire surface depending on the asperity of the road is important. It is considered that the hysteresis loss derived from the difference in the deformation inside the tire and that of the tire surface is related to the gripping property of the tire; therefore, observing inside the tire and the tire surface under dynamic deformation is the key for explaining the gripping mechanism of the tire. In a typical observation method of the

deformation behavior of rubber, the rubber was contacted with a transparent flat plate, and the contact area was observed from the opposite side through the flat plate by a CCD camera [1]. However, it is difficult to observe the contact area between the rubber and a non-flat road or opaque road. Because the asperities of the road provide stimulus to the tire, observing the contact area between the rubber and only a flat plate is not adequate to understand the deformation behavior of the tire. As an alternative observation method, the contact area between the rubber and the road was observed from the lateral side by a CCD camera [2, 3]. Although it is possible to observe the contact area between the rubber and a non-flat road or opaque road, the information is not adequate for the deep understanding of the deformation behavior of the tire with only the lateral side observation. Moreover, in these ways of using the visible wavelength with a CCD camera, it is impossible to observe inside the rubber unless the tire is transparent, and the deformation behavior inside the rubber should be observed to elucidate the phenomenon of hysteresis loss.

In order to solve these problems, X-ray computed tomography (CT) was used [4-8]. According to this study, rubber was stretched by the projection of roads, and cracks arise on the surface of such stretched rubber. In addition, when cracks arise, the frictional force between the rubber and the road increases to a maximum value and then decreases drastically. Such dynamic observation in the usage environment of each product is important for the material development.

In this study, we focus on the phenomenon of hysteresis loss of the rubber and observe its dynamic deformation behavior depending on the asperity of the road using a four-dimensional X-ray CT (4D-CT) method.

7.2 Experimental

Materials and sample preparation

The details of the materials used in this study are summarized in Table 7.1. We used styrene-butadiene rubber (SBR; Nipol 1502, Zeon Corporation), and the ingredients were mixed with an internal mixer until the temperature of the compound reached 423 K. The compounds were molded into a roller at 443 K for 12 min. The obtained rubber roller is cylindrical in shape with a diameter of 60 mm and height 10 mm.

Table 7.1: Sample recipe (weight ratios normalized with SBR).

SBR	100
Stearic acid	2
Zinc oxide	2
Sulfur	1.5
TBBS	1

Abbreviations: SBR, styrene-butadiene rubber;
TBBS, *N*-tert-butylbenzotiazole-2-sulphenamide.

Oscillation apparatus

Figure 7.1 shows the schematic diagram of an oscillation exciter and a control system. In the oscillation exciter, a rubber roller is oscillated up and down by rotating a stepper motor because a cam is placed on the rotational axis of the stepper motor. The oscillation exciter is fixed on the top panel of the apparatus, and only the rubber roller oscillates. We constructed the oscillation apparatus for this study.

While an automobile is moving, pulsed stimuli are applied to the tire depending on the rotational period of the tire. Therefore, in this apparatus, similar automobile driving stimuli are applied to the rubber roller by oscillating the rubber roller on the road. The oscillation frequency of the rubber roller is 1 Hz, which means that the rubber roller moves from top to bottom for 0.5 s (loading process) and from bottom to top for 0.5 s (unloading process). A load of 20 N is applied. The amplitude of oscillation of the rubber roller is fixed, and the load can be controlled by the height of a Z-axis stage. The replica of an actual road in the acrylic resin is used for this experiment.

4D-CT experiments

4D-CT experiments were performed at BL20B2 in SPring-8, Nishiharima, Japan. The X-ray energy and exposure time are 25 keV and 30 ms, respectively. The detector consists of beam monitor 5 and an X-ray CCD camera (C4880-41s, Hamamatsu Photonics K.K.). The resolution of the detector is 11.9 $\mu\text{m}/\text{pixel}$. The oscillation exciter is synchronized with the CT controlling unit by the transistor-transistor-logic (TTL) signal outputted from a proximity sensor, and the deformation behavior of the oscillated rubber roller in a contact face between the rubber roller and the road is observed by controlling the timing of the stage rotation and camera

with a pulse generator.

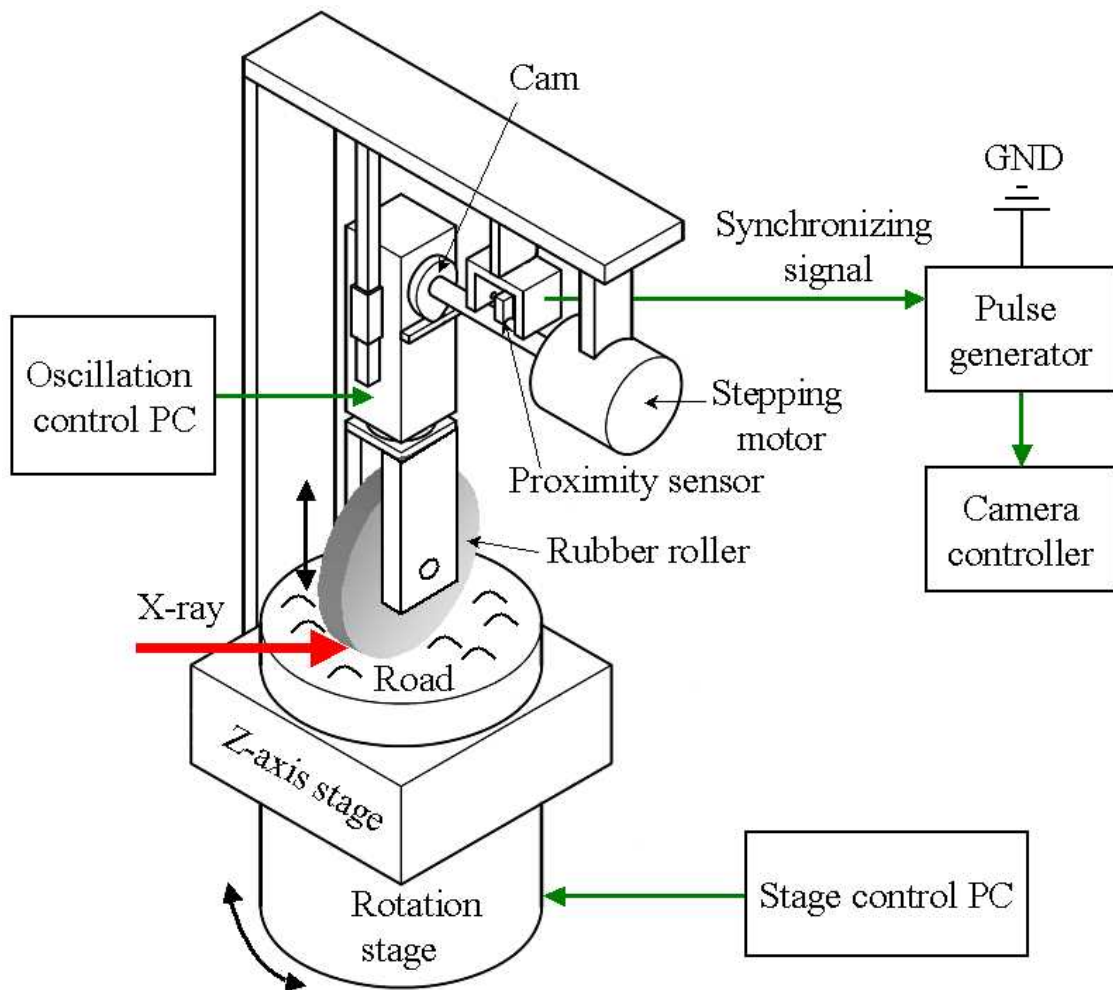


Figure 7.1: Schematic diagram of the apparatus.

7.3 Results and Discussion

Figure 7.2 shows the three-dimensional cross-section of the road and the rubber roller obtained by the 4D-CT method. Seemingly, the rubber deforms depending on the asperity of the road. Thus, by using the 4D-CT method, we successfully observed the dynamic deformation behavior of the rubber when contacted with the road continuously in three-dimension. It is possible to analyze the deformation behavior of the rubber depending on the asperity of the road at any moment and cross-section of the rubber.

Figure 7.3 shows the deformation behavior of the rubber at the contact face between the rubber and the road in the loading and unloading processes. In Figure 7.3, we excluded the road by image processing and displayed only the rubber. By comparing the images corresponding to the loading and unloading processes, it is observed that the contact area between the rubber and the road in the unloading process is larger than that in the loading process. This suggests that the response of the rubber is delayed after the contact with the road. Thus, in the 4D-CT method, the dynamic deformation behavior of the rubber depending on the asperity of the road, which was difficult to observe using conventional methods, was successfully observed.

To compare the deformation behavior of the rubber in the loading process with that in the unloading process quantitatively, the delay time dependence of the contact area between the rubber roller and the road is shown in Figure 7.4. The delay time is the timing of X-ray exposure and indicates the position of the rubber roller. Therefore, the rubber roller attains the top position of oscillation at 0 and 1000 ms and the bottom position of oscillation at 500 ms. The contact area in the unloading process is larger than that in the loading process at each position of oscillation, suggesting that the hysteresis phenomenon, which is the difference in the

deformation behavior between the loading and unloading processes.

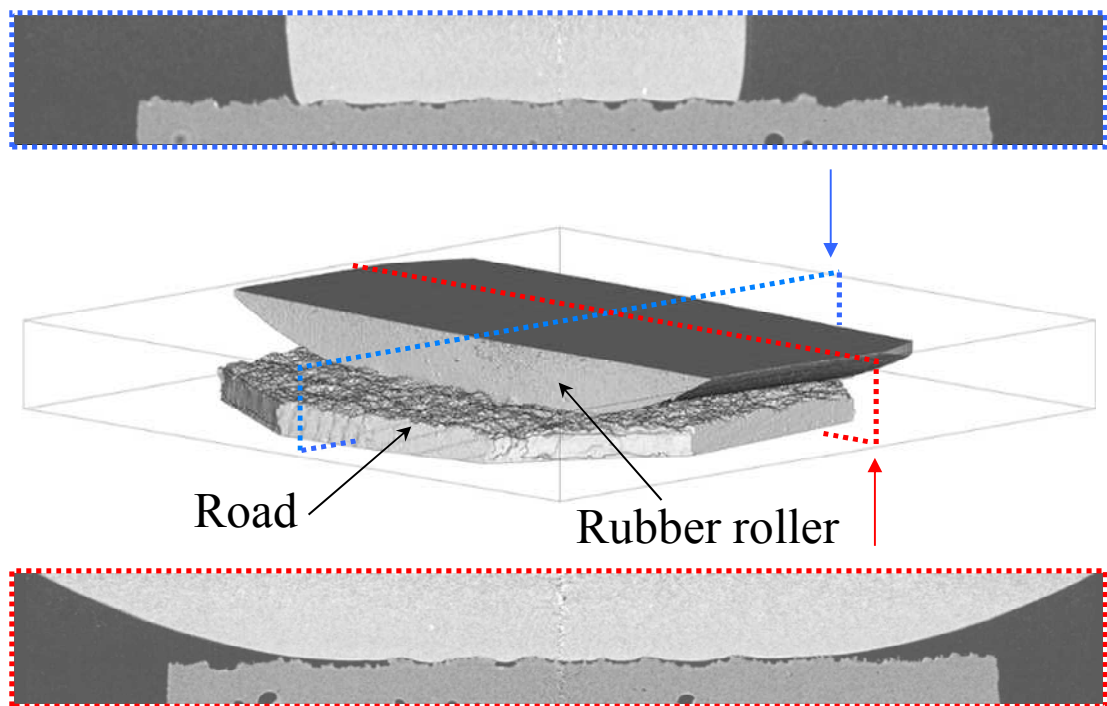


Figure 7.2: Three-dimensional cross-section of the road and rubber roller reconstructed by 4D-CT method.

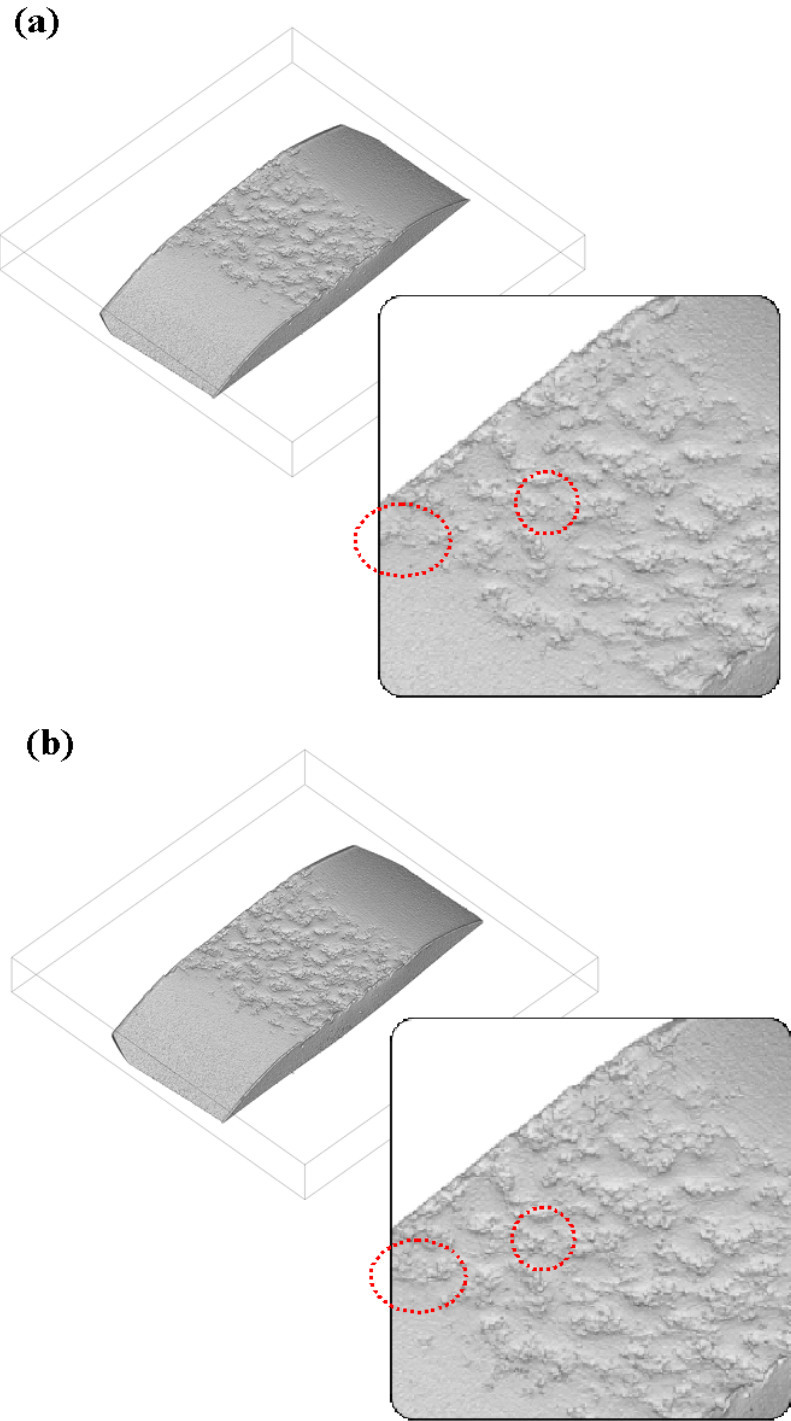


Figure 7.3: Deformation behavior of rubber in a contact face between the rubber roller and the road: (a) loading process and (b) unloading process.

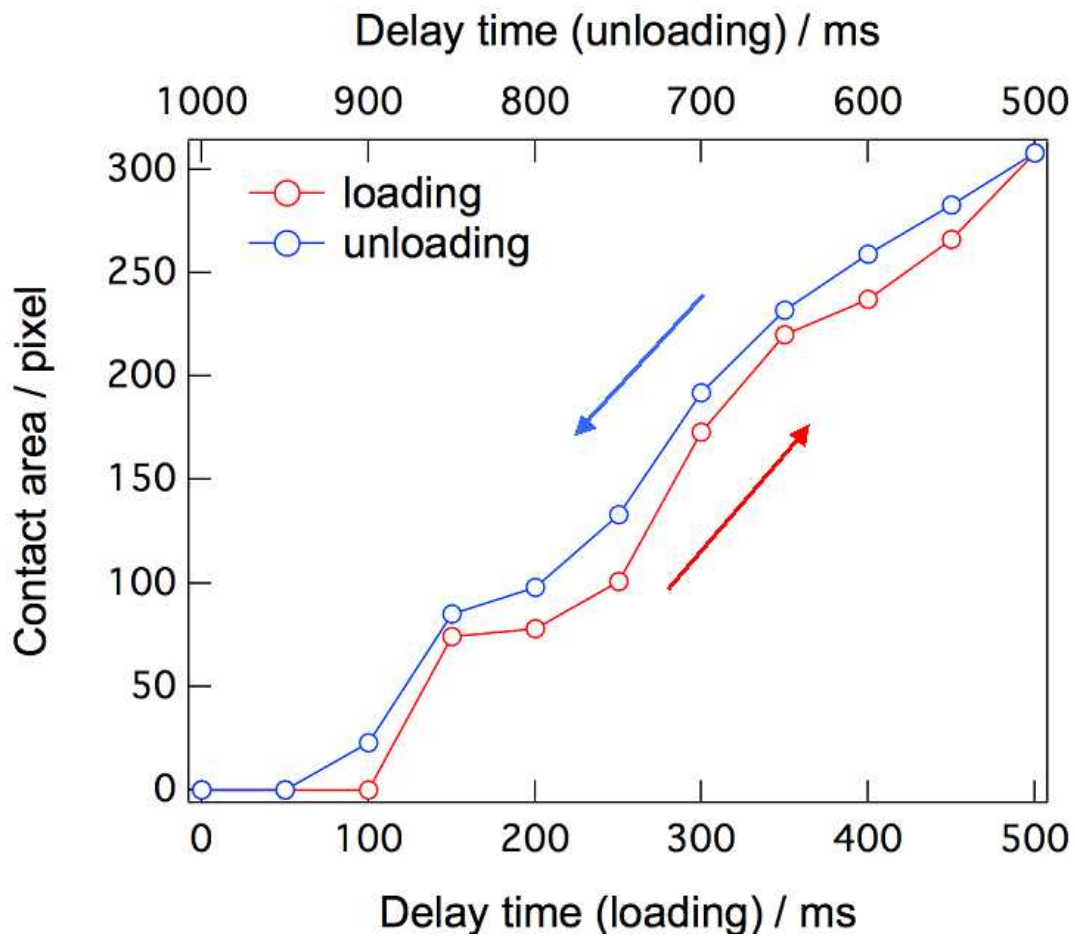


Figure 7.4: Delay time dependence of contact area between the rubber roller and the road.

Thus, under simulated automobile driving, the hysteresis phenomenon of the deformation behavior of rubber was observed. Because the energy lost in the hysteresis phenomenon affects the gripping property of a tire, this study will play an important role in the improvement of the gripping property of tires.

7.4 Conclusion

In this study, we investigated the dynamic deformation behavior of the tire depending on the asperity of the road by a 4D-CT method aiming at the observation of hysteresis phenomenon of the tire. Under simulated automobile driving, the dynamic deformation behavior of the rubber depending on the asperity of the road, which was difficult to observe using conventional methods, was successfully observed. In addition, the contact area in the unloading process is larger than that in the loading process at each position of oscillation suggesting the hysteresis phenomenon, which is the difference in the deformation behavior between the loading and unloading processes. This observation of hysteresis phenomenon is important to improve the gripping property of the tire of an automobile.

References

- [1] M. Barquins, *Mater. Sci. Eng.* **73**, 45 (1985).
- [2] Y. Uchiyama, Y. Ishino, *Wear* **158**, 141 (1992).
- [3] T. Iwai, Y. Uchiyama, K. Shimosaka, K. Takase, *Wear* **259**, 669 (2005).
- [4] N. Amino, Y. Uchiyama, T. Iwai, *Nippon Gomu Kyokaishi* **74**, 110 (2001).
- [5] N. Amino, Y. Uchiyama, T. Iwai, *Nippon Gomu Kyokaishi* **82**, 346 (2008).
- [6] N. Amino, Y. Ishikawa, M. Takeuchi, *Nippon Gomu Kyokaishi* **84**, 117 (2011).

[7] N. Amino, *Nippon Gomu Kyokaishi* **85**, 332 (2012).

[8] N. Amino, Y. Ishikawa, M. Sato, *Nippon Gomu Kyokaishi* **87**, 278 (2014).

Summary

This thesis includes studies on static and dynamic structure of crosslinked rubber with reinforcing agent by quantum beam. The contents of the respective chapters are summarized below.

In Chapter 1, the author gave a brief summary of the reinforcement effects of crosslinking agents and reinforcing fillers for rubber and reviewed the previous works on the rubber reinforced with crosslinking agents and reinforcing fillers to show a basis of the studies in this thesis.

In Chapter 2, fundamental theories of static and dynamic structure analysis techniques used in this thesis, small-angle X-ray scattering (SAXS), small-angle neutron scattering (SANS), quasielastic neutron scattering (QENS), muon spin relaxation (μ SR) and X-ray computed tomography (CT), were described to provide physical meanings to the observables.

In Chapter 3, a static structure of a polybutadiene rubber (BR) reinforced with zinc diacrylate (ZDA) (ZDA/BR) system was investigated by using both SAXS and SANS techniques. ZDA was found to hierarchically aggregate in a size range from nanometers to micrometers. In addition, differences in scattering intensity profiles between SAXS and SANS indicate the existence of high crosslinking density BR (HC-BR) layers.

In Chapter 4, a static structure of a ZDA/BR was studied by CV-SANS method to reveal the detail of HC-BR. A correlation between ZDA and HC-BR layers was observed, indicating the existence of HC-BR layers around ZDA aggregates. In addition, some parameters of these layers, such as thickness, approximately 1 – 5 nm, and volume fraction of HC-BR, $\phi_{\text{total-HC-BR,fit}} = 0.147$, were quantitatively described.

In Chapter 5, the dynamics of a ZDA/BR system was studied with QENS measurements in a picosecond time scale. Mean square displacements $\langle u^2 \rangle$ decrease with an increase in the ZDA volume fraction indicating that the BR

dynamics is affected by ZDA. In addition, dynamic scattering laws were narrowed with increasing ZDA volume fraction, suggesting that the mobility of BR slowed with the increase of ZDA volume fraction. Dynamic scattering law can be divided into elastic scattering component (= immobile component) and inelastic scattering component (=mobile component), and the amount of immobile component (*EISF*) increased with the ZDA volume fraction. On the other hand, increase of mean relaxation time ($\langle\tau\rangle$) and broadening of the relaxation time distribution (β) of mobile component were evaluated as a function of the ZDA volume fraction. Considering the results of Chapter 3 and 4, it was suggested that the mobile and immobile components obtained by QENS correspond to matrix BR and HC-BR, respectively, revealing the heterogeneity of BR dynamics.

In Chapter 6, hierarchical dynamics of the ZDA/BR system were studied by μ SR measurements in a microsecond time scale. The obtained relaxation rates above the glass transition temperature at higher ZDA volume fractions were smaller than those at lower ZDA volume fractions, indicating that BR dynamics is suppressed by ZDA at this particular time scale.

Based on the results of Chapter 3 to 6, it was concluded that ZDA aggregates hierarchically in the range from nanometers to micrometers and HC-BR layers around the ZDA aggregates form the rigid network, which suppress the mobility of BR in a wide time scale, leading to the high elastic modulus of ZDA/BR.

In Chapter 7, a dynamic deformation behavior of tire rubber was studied by four-dimensional X-ray CT (4D-CT), simulating real-world conditions. Hysteresis characteristics of the tire rubber were confirmed during interactions between the rubber and a road.

List of publications

Journal

Chapter 3

“Small-angle X-ray and Neutron Scattering Analyses of Highly Crosslinked Rubber with Unsaturated Carboxylic Acid”, R. Mashita, H. Kishimoto, R. Inoue, and T. Kanaya, *Polymer Journal* **45**, 57 (2013).

Chapter 4

“Structure Analyses of Polybutadiene Rubber Crosslinked with Unsaturated Carboxylate using Contrast Variation Small-angle Neutron Scattering”, R. Mashita, H. Kishimoto, R. Inoue, and T. Kanaya, *Polymer Journal*, in press.

Chapter 5

“Quasielastic Neutron Scattering Study of Microscopic Dynamics in Polybutadiene Reinforced with an Unsaturated Carboxylate”, R. Mashita, R. Inoue, T. Tominaga, K. Shibata, H. Kishimoto, and T. Kanaya, submitted to *Macromolecules*.

Chapter 6

“Dynamical Study of Polybutadiene Reinforced with an Unsaturated Carboxylate by Muon Spin Relaxation”, R. Mashita, R. Inoue, H. Kishimoto, and T. Kanaya, to be submitted to *Phys. Rev. E*.

Chapter 7

“Observation of Deformation Behavior of The Rubber Depending on Asperity of Road by Four-Dimensional X-ray Computed Tomography”, R. Mashita, and H. Kishimoto, *X-Ray Imaging Optics News Letter* **40**, 1 (2014).

Acknowledgments

The present thesis is based on the study carried out under the instruction of Professor Toshiji Kanaya, Laboratory of Polymer Materials Science, Division of Multidisciplinary Chemistry Polymer Materials Science, Institute for Chemical Research, Kyoto University, from 2013 to 2015.

The author would like to express his most sincere thanks to Professor Toshiji Kanaya for his continuous guidance, shrewd comments, discussion and collaborations through the course of the study.

Professor Yoshinobu Tsujii, Professor Takenao Yoshizaki and Professor Hiroshi Watanabe are especially acknowledged for their critical review of this thesis.

The author wishes to express his gratitude to Associate Professor Rintro Inoue for his continuous encouragements, discussions and collaborations throughout this investigation.

The author is indebted to Associate Professor Koji Nishida and Assistant Professor Hiroki Ogawa for their helpful guidance and advice.

The author is sincerely grateful to Dr. Daisuke Yamaguchi for his kind support in SANS measurement at JRR-3 SANS-J-II; to Dr. Hiroyasu Masunaga for his kind support in SAXS measurements at SPring-8 BL03XU; to Dr. Noboru Ohta for his kind support in SAXS measurement at SPring-8 BL40B2; to Dr. Masugu Sato for his kind support on USAXS measurement at SPring-8 BL19B2; to Dr. Young-Soo Han and Dr. Tae-Hwan Kim for their kind support in the SANS measurements at HANARO 40m SANS; to Dr. Yoshio Suzuki, Dr. Akihisa Takeuchi and Dr. Yuya Shinohara for their kind support in the USAXS measurements at SPring-8 BL20XU; to Dr. Kaoru Shibata and Taiki Tominaga for their kind support in the QENS measurement at J-PARC BL02 DNA; to Dr. Ryosuke Kadono, Dr. Kenji Kojima, Dr. Akihiro Koda, Dr. Soshi Takeshita, Dr. Ichihiko Yamauchi and

Dr. Masanori Miyazaki for their kind support in the μ SR measurement at J-PARC Muon D1; to Dr. Kentro Uesugi and Dr. Masato Hoshino for their kind support in the 4D-CT measurements at SPring-8 BL20B2.

The synchrotron X-ray radiation experiments with the approval of the Japan Synchrotron Radiation Research Institute (JASRI) are listed as below.

Proposal No.	Facility	Beamline No.	Corresponding Chapter
2010A1746	SPring-8	BL40B2	Chapter 3
2010B1932	SPring-8	BL19B2	Chapter 3
2010B7264	SPring-8	BL03XU	Chapter 3
2011B1244	SPring-8	BL20XU	Chapter 4
2011B1254	SPring-8	BL20B2	Chapter 7
2011B7260	SPring-8	BL03XU	Chapter 4
2012A1286	SPring-8	BL20B2	Chapter 7
2012A1686	SPring-8	BL20XU	Chapter 4
2012A7210	SPring-8	BL03XU	Chapter 4
2012B1262	SPring-8	BL20B2	Chapter 7
2013A1248	SPring-8	BL20B2	Chapter 7
2013A1441	SPring-8	BL20B2	Chapter 7
2013B1127	SPring-8	BL20B2	Chapter 7
2014A1183	SPring-8	BL20B2	Chapter 7

The SANS measurement at the SANS-J-II instrument installed at JRR-3 in Chapter 3 was performed with the approval of the Japan Atomic Energy Agency (JAEA) (Proposal 2010B-A37).

The QENS measurement at the BL02 DNA instrument installed at J-PARC in Chapter 5 was performed with the approval of the Materials and Life Science Experimental Facility (MLF) of J-PARC (Proposal No. 2014A0014).

The μ SR measurements at the Muon D1 instrument installed at J-PARC in Chapter 6 were performed with the approval of the MLF of J-PARC (Proposal No. 2013B0016 and 2014A0009).

The author wishes to express thanks to my colleagues of Sumitomo Rubber Industries, Ltd. and all the past and current members of Kanaya laboratory.

Finally, the author expresses his gratitude to his family.

March 2016

Ryo Mashita